Computational and Mathematical Methods in Medicine

Complex Systems Models in Biology and Medicine: Generic Properties and Applications

Guest Editors: Roberto Serra, Rudolf Füchslin, Erik Schultes, and Marco Villani

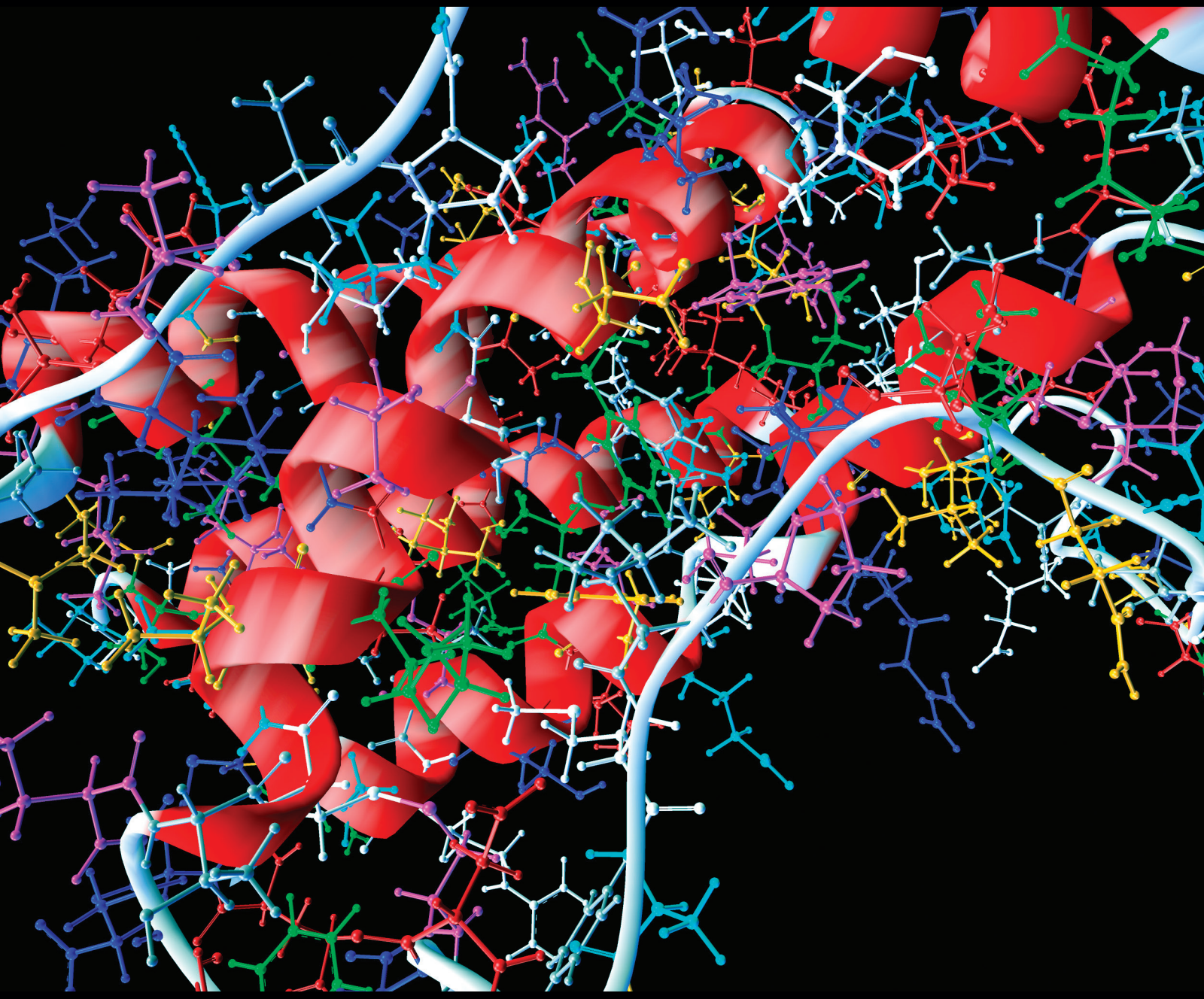

Complex Systems Models in Biology and Medicine: Generic Properties and Applications

Computational and Mathematical Methods in Medicine

Complex Systems Models in Biology and Medicine: Generic Properties and Applications

Guest Editors: Roberto Serra, Rudolf Füchslin, Erik Schultes, and Marco Villani

Editorial Board

Contents

Hindawi Publishing Corporation
Computational and Mathematical Methods in Medicine
Volume 2014, Article ID 580509, 1 page
http://dx.doi.org/10.1155/2014/580509

Editorial

Complex Systems Models in Biology and Medicine: Generic Properties and Applications

Roberto Serra

Department of Physics, Informatics and Mathematics, Modena and Reggio Emilia University, Modena, Italy

Correspondence should be addressed to Roberto Serra; rserra@unimore.it

Received 18 May 2014; Accepted 18 May 2014; Published 15 June 2014

Living organisms are complex systems and indeed some concepts of complex systems science, like those of network theory, have been extensively applied in biology and medicine. However, the penetration of other major concepts of complexity theory is still limited. A good example is the dynamical attractor: in spite of the fact that its application to biology was suggested more than 40 years ago and of the fact that there are several beautiful applications, it is still rarely found in models of biological processes and of medical treatment. The penetration of other candidate general concepts that are still more controversial, like for example, that of criticality, is even slower.

On the other hand, complex systems science promises to give novel and important theoretical insights in medicine and biology, including nervous system, immune system, hormonal systems, and metabolic systems, and it can be also very fruitful from an application-oriented perspective. Moreover, while its methods can be applied to the study of well-defined specific cases, they are particularly well-suited to describe "generic" properties, that are common to a wide class of organisms or processes.

The selection procedure for this special issue has been quite rigorous, resulting in a rejection rate of 50%. The papers that have been selected for publication cover some important and intriguing aspects. The paper by Borrotti et al. shows how it is possible to use evolutionary methods to optimize the design of experiments to find new macromolecules with desirable properties, thereby reducing the number of points to be tested. Ghaffarizadeh and colleagues address the fascinating phenomena involved in cell differentiation and present a tool to analyze and visualize the transitions among different cell types, while Weyland et al. explore the role of compartimentalization for polymer sysnthesis, addressing both biological cells and artificial systems. Scheidegger et al. propose a novel model of the response of tumor cells to radiation and heat, amenable to experimental testing, and Dresp-Langley's paper suggests the existence of a universal power law for the adaptive balance of motor responses to environmental stimuli from various sensor modalities. Finally, Sahiner and Yigit show how rough set theory can be applied to medical diagnosis.

While much has still to be done, it is worthwhile to emphasize that, taken together, the papers presented in this special issue of Computational and Mathematical Models in Medicine provide further evidence in favour of the usefulness and importance of complex systems science in medicine.

Roberto Serra

Hindawi Publishing Corporation
Computational and Mathematical Methods in Medicine
Volume 2014, Article ID 293980, 10 pages
http://dx.doi.org/10.1155/2014/293980

Research Article

Modeling and Visualizing Cell Type Switching

Ahmadreza Ghaffarizadeh,[1] Gregory J. Podgorski,[2,3] and Nicholas S. Flann[1,4,5]

[1] *Computer Science Department, Utah State University, Logan, UT 84322, USA*
[2] *Biology Department, Utah State University, Logan, UT 84322, USA*
[3] *Center for Integrated BioSystems, Utah State University, Logan, UT 84322, USA*
[4] *Institute for Systems Biology, Seattle, WA 98109, USA*
[5] *Synthetic Biomanufacturing Institute, Logan, UT 84322, USA*

Correspondence should be addressed to Nicholas S. Flann; nick.flann@usu.edu

Received 30 September 2013; Revised 20 December 2013; Accepted 10 January 2014; Published 14 April 2014

Academic Editor: Marco Villani

Understanding cellular differentiation is critical in explaining development and for taming diseases such as cancer. Differentiation is conventionally represented using bifurcating lineage trees. However, these lineage trees cannot readily capture or quantify all the types of transitions now known to occur between cell types, including transdifferentiation or differentiation off standard paths. This work introduces a new analysis and visualization technique that is capable of representing all possible transitions between cell states compactly, quantitatively, and intuitively. This method considers the regulatory network of transcription factors that control cell type determination and then performs an analysis of network dynamics to identify stable expression profiles and the potential cell types that they represent. A visualization tool called *CellDiff3D* creates an intuitive three-dimensional graph that shows the overall direction and probability of transitions between all pairs of cell types within a lineage. In this study, the influence of gene expression noise and mutational changes during myeloid cell differentiation are presented as a demonstration of the *CellDiff3D* technique, a new approach to quantify and envision all possible cell state transitions in any lineage network.

1. Introduction

During development, a complex system of tissues and organs emerges from a single cell by the coordination of cell division, morphogenesis, and differentiation. Understanding the differentiation of cell types is necessary to understanding development and its associated defects, for improved control of stem cell differentiation in therapeutic use and for taming diseases such as cancer. Cellular differentiation occurs when a less specialized cell or its progeny becomes increasingly specialized by acquiring properties that allow specific functions. In animals, differentiation typically results in a terminally differentiated state in which a specialized cell can no longer acquire the properties of other specialized adult cells. Recent discoveries, however, have shown that terminally differentiated cells can be reprogrammed to revert back to multipotent and pluripotent stem cells which have the potential to differentiate into other cell types [1, 2] or to transdifferentiate into other specialized cell types [3].

Differentiating cells normally follow well defined paths to mature cell types. Taken together, these paths are referred to as a lineage tree. Pluripotent stem cells give rise to progeny that specialize into more constrained multipotent cells. In turn, multipotent cells produce a variety of stable, terminally differentiated cells. This process is usually depicted as a tree with a pluripotent cell at its root, multipotent cells as intermediate nodes, and the mature cell types as branch tips. As an example, a simplified portion of the myeloid cell lineage tree is illustrated in Figure 1. This figure shows that common myeloid progenitor stem cells produce two pluripotent cell types, a megakaryocyte-erythrocyte progenitor and a granulocyte-monocyte progenitor, that in turn produce terminally differentiated erythrocytes, megakaryocytes, monocytes, and granulocytes.

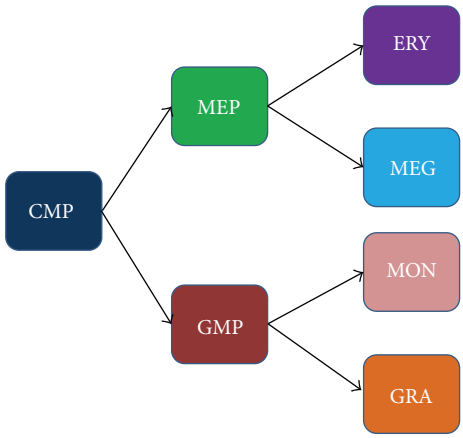

Figure 1: A simplified myeloid lineage tree from [4] where the terminal nodes are mature terminally differentiated erythrocytes (ERY), megakaryocytes (MEG), monocytes (MON), and granulocytes (GRA). Multipotent cells are the common myeloid progenitor (CMP), megakaryocyte-erythrocyte progenitor (MEP), and granulocyte-monocyte progenitor (GMP). The color assigned to each cell type in this figure is also used in the differentiation network shown in Figure 4.

Intracellular genetic regulatory networks (GRNs) control differentiation by responding to external (extracellular) and internal (intracellular) stimuli that reconfigure gene expression profiles and change cell physiology [5]. There is a growing body of evidence that cell types are determined by stable expression patterns of the regulatory networks, referred to as attractors. Switching between cell types amounts to transitioning from one attractor to another [6]. The attractor model explains how cell types can be stable under gene expression noise and how changes in the expression of a small number of master regulators can shift the expression of hundreds of genes as cell types switch.

Regulatory network dynamics are driven by molecular events within the cell that are subject to noise [7]. Understanding the role of noise in gene expression and its effect on differentiation is essential to gaining insight into cellular specialization and its errors. If cell types are attractors of the GRN, these attractors must be robust to noise in order to maintain particular cell types and to stay on the correct branches of the lineage tree during differentiation. Failure to do either can have dire consequences. For instance, cancer has been proposed to involve destabilization of attractor states due to changes in genetic regulatory network dynamics [8]. In this view, the attractors that correspond to normal cells switch to new, abnormal attractors characteristic of cancer cells. In addition to pathological states, transitions between attractor states of differentiated cells may lead to dedifferentiation, in which a cell reverts to an earlier multipotent state, or transdifferentiation, in which a differentiated cell switches to another adult differentiated cell type [9]. Abnormal type switching may also result in off-differentiation in which a multipotent cell from one branch of a lineage tree is converted to a differentiated cell on another branch of the tree. Finally, to maintain a population of multipotent cells, at least some of these cells must resist differentiation to later stages within the lineage tree [10].

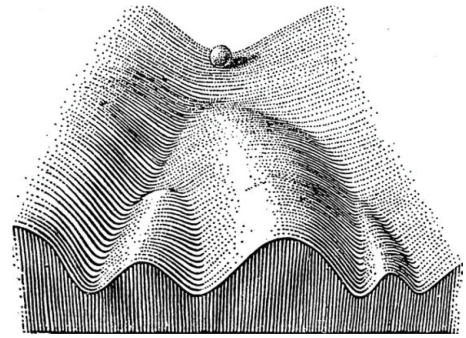

Figure 2: Waddington's classic model of an epigenetic landscape [11]. A developmentally immature cell, represented as a ball at the top rolls downhill and is deflected right or left at each branch point until it reaches a catch basin (not shown in this diagram) that corresponds to a terminally differentiated cell.

An early and influential way of viewing differentiation is Waddington's [11] epigenetic landscape. Waddington envisioned differentiation occurring on a rugged landscape of sloping ridges and valleys (see Figure 2). Waddington represented an undifferentiated cell as a ball at the uppermost point of the highest valley. Differentiation occurred as this ball rolled downhill, encountering the ends of ridges that define branch points between valleys. At each of these branch points, the ball moved left or right to follow the new sloping valley to another ridge terminus that separates yet another pair of valleys. Each ridge terminus represents a progenitor cell in a conventional lineage tree and the movement to right or left into a new valley from this branch point represents a commitment of the progenitor to one or another lineage. The ridges represent barriers that maintain a cell state once it is chosen.

In the decades since Waddington proposed his model, many investigators have used the concept of an epigenetic landscape and tailored it to explain a variety of developmental processes. Waddington himself cautioned that the epigenetic landscape is an abstraction that could not be rigorously interpreted [11]. Some recent work has tried to enhance Waddington's epigenetic landscape to move it from metaphor to rigorous model [1, 12–15]. However, even with these extensions, the ridge-and-valley topography of the epigenetic landscape places a fundamental limit on the number and kinds of cell type transitions that can be shown. For example, representing transdifferentiation between nonadjacent lineages in Waddington's model requires jumping over two or more ridges and showing dedifferentiation requires uphill movement. Conventional two-dimensional lineage trees suffer from similar problems. Even more significant than difficulties in visually representing nonstandard, yet documented transitions between cell types is that Waddington's epigenetic landscape and conventional lineage trees both fail to provide quantification of the probability of any transition. Finally, epigenetic landscapes and conventional lineage trees show only a small fraction of the possible transitions between cell types. Many of these transitions were previously considered

Table 1: Summary of different kinds of cell type transitions with possible examples from myeloid differentiation tree shown in Figure 1.

Transition	Example	Definition
Spontaneous-differentiation	CMP to MEP	Cell switches to a more specialized state
Spontaneous-dedifferentiation	MON to GMP	Cell reverts to an earlier multipotent state
Off-differentiation	GMP to ERY	Cell switches to a more specialized state but on a wrong branch of the lineage tree
Off-dedifferentiation	MEG to GMP	Differentiated cell reverts to an earlier multipotent state but on a wrong branch of the lineage tree
Transdifferentiation	GRA to ERY	Differentiated cell switches to another differentiated state

hypothetical, but with ability to induce pluripotent stem cells from adult differentiated cells and to induce transdifferentiation between lineages, these changes in cell type are well known. To illustrate the limitations of standard representations of cell lineages, a generalized epigenetic landscape like that shown in Figure 2 that considers m cell type attractors can only represent a maximum of $2m - \log_2(m + 1) - 1$ cell type transitions. This formulation considers the expected differentiation transitions within the lineage tree ($m - 1$) and transdifferentiation events between adjacently arranged cell types on the tree ($m - \log_2(m + 1)$). As the number of cell types in a system increases, the limitations of the epigenetic landscape become more acute: the number of representable transitions grows with $O(m)$, while the number of possible transitions grows with $O(m^2)$. Given that nonstandard attractor type transitions play key roles in cancer and disease development, coupled with the ability to experimentally induce dedifferentiation and transdifferentiation and the possibility of off-differentiation events, improvements are needed in the visualization of cellular differentiation.

In this work, we present a new method that generates a three-dimensional graph of attractors and all possible transitions between them to overcome the limitations of a conventional representation of cellular differentiation. Our technique, implemented by a tool called *CellDiff3D*, analyzes the network of attractors generated by a random Boolean GRN. In this work, the GRN that simulates myeloid cell differentiation is used as a demonstration. A noise analysis of the network dynamics is performed to identify m attractors and the likelihood of all the possible $m(m-1)$ transitions between them. This information determines the layout of the graph. The graph is easy to interpret and qualitatively represents the likelihood of transitions between cell types, their overall direction, and rate under the influence of noise. Visualization of the results of *CellDiff3D* is achieved by virtual reality modeling language (VRML) that allows the user to zoom and rotate the three-dimensional lineage network. The *CellDiff3D* tool can be downloaded from http://www.celldiff3d.org/.

2. *CellDiff3D* Design and Visualization

2.1. Separation and Flux between Attractors. We use the mean first passage time (MFPT) [16] between the attractors of any given GRN, represented qualitatively as a Boolean network [17]. MFPT determines the probability and directionality of each theoretically possible transition between all pairs of network states. Introduced by Shmulevich et al. [16], $\mathrm{MFPT}(a_i, a_j)$ between a pair of attractors, a_i and a_j, is an estimate of the average number of state update steps of a Boolean network that are required to transition from an attractor state a_i to an attractor state a_j when the network operates under uniform random noise. Noise is modeled by having each bit (gene expression value) have a probability of changing states (a bit flip, from expressed to nonexpressed or vice versa) at each state update step. Low MFPTs indicate a high likelihood of a transition between cell states and high MFPTs indicate low likelihood for this transition. Once MFPT between two attractors of a network is estimated, then two useful derived measures of the epigenetic barrier between attractors can be determined: the separation between attractors and the flux of transitions between them. Let the separation between two attractors i, j be

$$\text{separation}(i, j) = \min\left(\text{MFPT}(i, j), \text{MFPT}(j, i)\right). \quad (1)$$

Higher separation implies a lower likelihood of transition between attractors. Note that separation is symmetric. Flux establishes the directionality of the transition by quantifying the difference between the rates (MFPTs) of forward and reverse transitions between a pair of attractors. The flux between attractors i, j is defined as

$$\text{flux}(i, j) = \text{MFPT}(i, j) - \text{MFPT}(j, i). \quad (2)$$

Note that flux establishes overall direction of the transition between cell states and is asymmetric.

2.2. Network Dynamics Visualization. An important element of GRNs is their behavior under gene expression noise. By definition, attractors are stable expression states of a genetic regulatory network, but this stability is relative and expected to vary depending on the network structure and dynamics. For example, terminally differentiated cell states are expected to be more stable than progenitor cells that may be more sensitive to noise-driven changes in states. High levels of gene expression noise may cause unexpected or pathological cell state transitions, with these transitions categorized based on the relative positions of the source and sink cell types in the normal lineage tree. Table 1 summarizes five kinds of transitions between cell types and provides an example of each case with respect to the cell types in the simplified myeloid lineage tree shown in Figure 1.

Two of these five transition types are represented easily in Waddington's epigenetic landscape: differentiation (moving

"downhill" in the landscape toward more specialized cell types) and dedifferentiation (loss of specialization shown by upward movement). Two other transition types cannot be shown in the classic epigenetic landscape representation: off-differentiation (differentiation to a cell type not on the normal lineage path); and off-dedifferentiation (loss of specialization to a cell type off the normal lineage path). Additionally, the epigenetic landscape limits visualization of transdifferentiation events (a switch from one adult differentiated cell type to another) to only those events that occur between adjacently arranged cell types. As discussed earlier, it is important to have a way of representing all possible transition types because off-differentiation and dedifferentiation are likely to play central roles in cancer [3, 8] and because recent evidence suggests that transdifferentiation may occur during normal development [18] as well as being induced in cultured cells [19].

Our method visualizes the different attractor transition kinds by constructing a 3-dimensional graph in which the distances between pairs of cell types are their separation (the minimum MFPTs between each pair) and the favored direction of the transition is shown by an arrow with a thickness proportional to the flux. In this way, the graph provides a quantitative view of these important parameters. To reach this result, the following steps are taken. First, the attractors of a given network are determined. Next, noise analysis (described later) is performed for each attractor pair and the separation and flux values are calculated. This is followed by mapping separation and flux values to a weighted directional graph in which attractors are shown as nodes. Mapping is done using *Graphviz*, an open source graphing application [20]. All these procedures are described in detail in the Methods Section below. Plotting separation and flux values using *Graphviz* produces 3-dimensional layouts of the graph which can be rotated freely in any web browser and that are easy to understand and analyze.

The graphical layout problem for showing cell type switching is defined in the following way. Let $i_{x,y,z}$ be the $\langle x, y, z\rangle$ coordinate of attractor i in the graph visualization, and let dist(i, j) be the Euclidean distance between points $i_{x,y,z}$ and $j_{x,y,z}$. Then, given a graph of m attractors defined as a set of separation $(i, j) \mid 1 \le i, j \le m$, the layout is defined by determining the set of coordinates for each attractor such that the following summation is minimized:

$$\sum_{1\le i,j\le m} \left(\text{dist}\left(i_{x,y,z}, j_{x,y,z}\right) - \text{separation}\left(i, j\right)\right)^2. \quad (3)$$

After determining the location of attractors (nodes) in 3D space, flux between pairs of attractors is represented by arrows (directed edges) of variable width between them with arrow width proportional to flux. The edge direction is given by the relationship between MFPT(i, j) and MFPT(j, i): if MFPT(i, j) < MFPT(j, i), then the edge is from i to j. The 3D graph is viewable in any web browser using the VRML viewer plugin (such as *Cartona3D*) and allows the user to rotate and zoom the graph to aid viewing, analyzing, and understanding the relationships between attractors within complex networks.

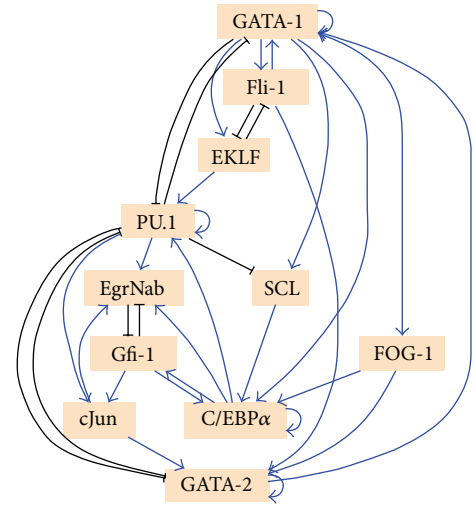

Figure 3: The genetic regulatory network used in this work for modeling myeloid differentiation. Nodes are eleven transcription factors that control cell lineage and edges are regulatory interactions between the transcription factors. An arrow signifies activation and a closed line signifies inhibition. The Boolean regulatory control functions are not shown. This network was discovered using a new search algorithm (paper in preparation) that uncovers networks that can produce a particular set of cell types, but it does not necessarily find the actual biological network.

2.3. Visualizing the Myeloid Differentiation Network. We modeled the simplified myeloid lineage network that is shown in Figure 1 to demonstrate the utility of the visualization technique. The modeling was based on the work of Krumsiek et al. [4] who considered a network of eleven transcription factors known to be important in myeloid cell differentiation. We extended this work by applying a novel search technique (paper in preparation) to discover a new Boolean regulatory network that is supported by the literature and whose dynamics produce all the attractors in the lineage tree, three attractors representing pluripotent cells, along with an additional 4 attractors representing the terminally differentiated cell types. The transcription factor expression pattern of each of these attractors corresponds to a myeloid cell type shown in Figure 1. Our GRN discovery method searches the space of Boolean GRNs converging to a specific GRN that minimizes the difference between the attractor's Boolean expression values and the experimental expression values of the corresponding cell types. The new inferred Boolean GRN is illustrated in Figure 3. The essential point for demonstrating the value of the *CellDiff3D* approach is that this network produces transitions between cell types that cannot be visualized using Waddington's epigenetic landscape or conventional lineage trees but can easily be seen and analyzed using *CellDiff3D*.

Figure 4 shows some outputs of the visualization method applied to simulated myeloid differentiation GRN. Running the myeloid GRN resulted in four attractors with gene expression levels that closely match the four terminally differentiated cell types (erythrocytes (ERY), megakaryocytes (MEG), monocytes (MON), and granulocytes (GRA)). In addition,

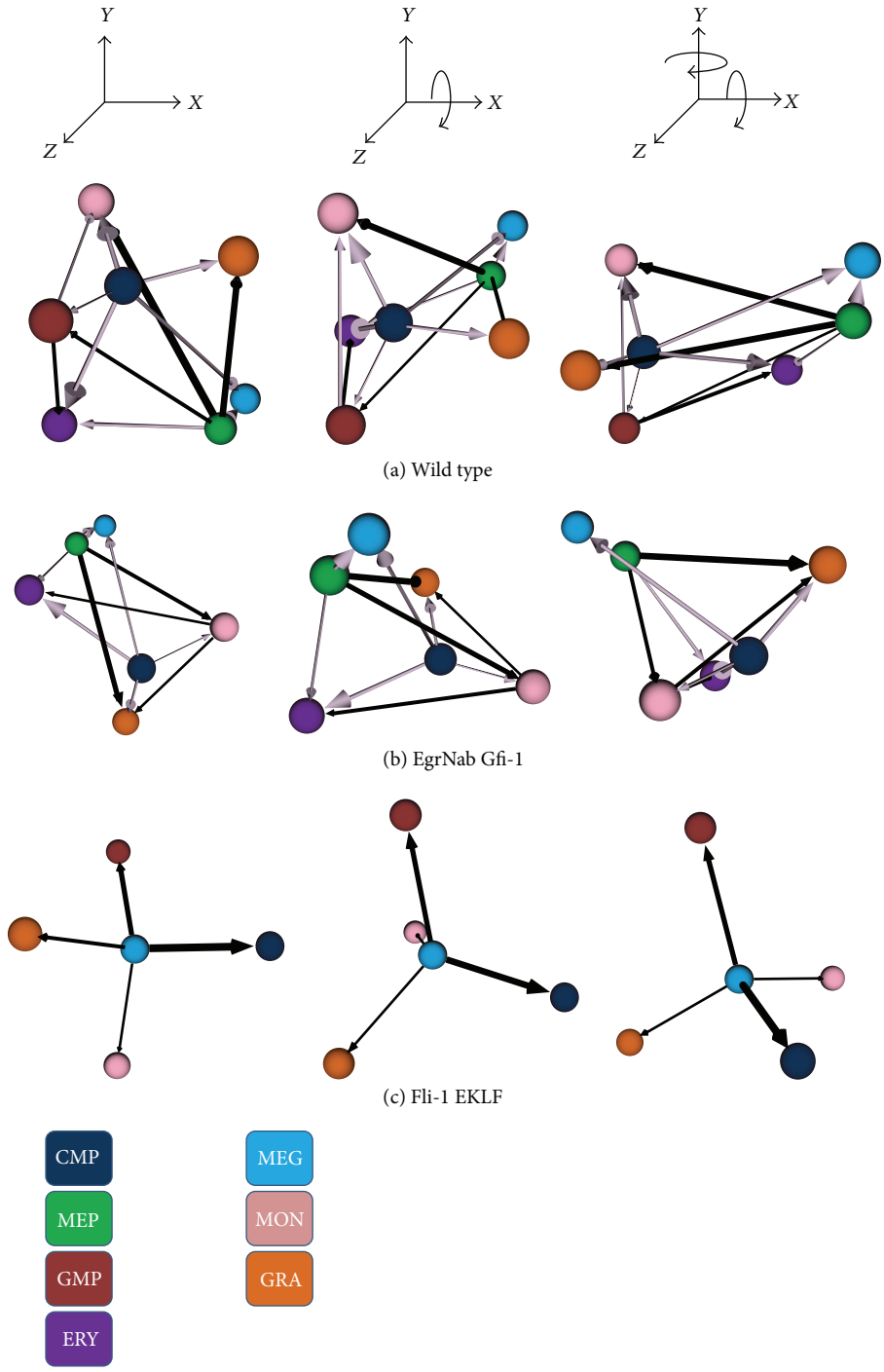

Figure 4: *CellDiff3D* visualization of the simulated myeloid differentiation network. Each image is a still taken from renderings of VRML code produced by the modeling method. The transcription factors and their regulatory interactions that comprise the GRN are shown in Figure 3. Each sphere is one of the myeloid cell types shown in Figure 1. Each row shows three orthographic views of cell type transitions derived from runs using the wild-type transcription factor network (top row of panel) or with transcription factor mutations in which the first transcription factor listed does not interact with the second transcription factor (lower rows of panel). The distance between each pair of cell types is the separation and the arrow direction and thickness are flux. For clarity, low flux edges are not shown. Lavender arrows show normal differentiation or dedifferentiation along the standard lineage tree from a specialized cell to its immediate progenitor; black arrows show transdifferentiation, off-differentiation, or off-dedifferentiation.

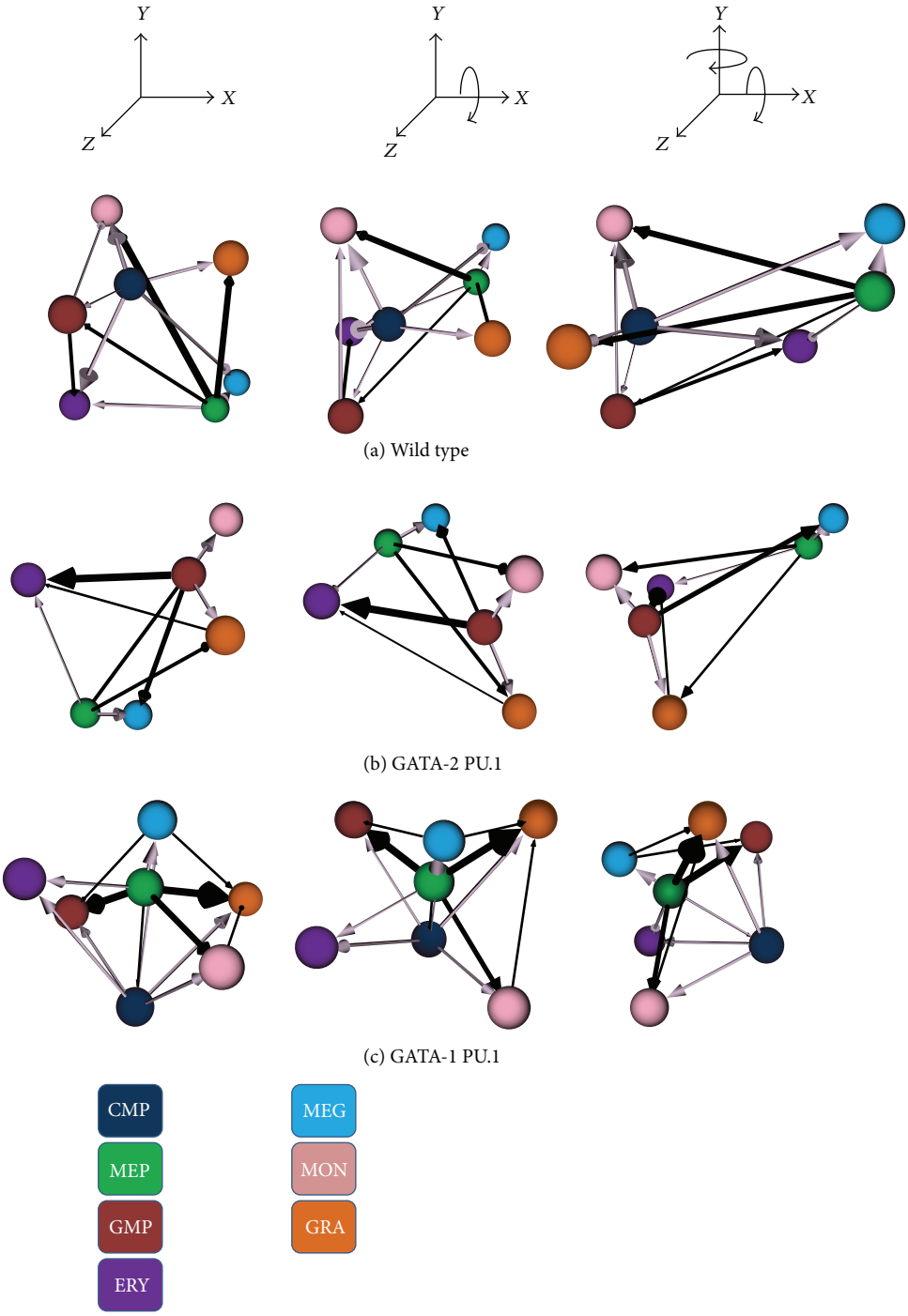

Figure 5: *CellDiff3D* illustration of the effects of two additional mutations that disrupt the myeloid differentiation network. There are interactions between GATA-2 to PU.1 (middle row) and GATA-1 to PU.1 (bottom row). See Figure 4 for extended caption.

there are three attractors that correspond to the MEP and GMP progenitors and the CMP stem cell (expression data is given in [4]).

Each row of Figures 4 and 5 shows three different orthographic projections of the 3D graph of the attractor network. The inferred Boolean network generated the seven stable attractors produced during normal myeloid differentiation (labeled wild type in Figures 4 and 5). Rows below the wild-type network show how network modifications (equivalent to mutations) alter the attractor landscape and how the technique described here can readily visualize these changes. These mutated GRNs were created by knocking out the forward interaction link between a transcription factor and one of its targets by always assigning this link a value of false then running the network to compute the MFPT. For example, in the second row of Figure 4, we

Table 2: Cell type transitions discovered and visualized in the myeloid differentiation network shown Figure 3 and in mutationally altered forms of this network.

Figure	Network	Cell type switch	Kind
Figure 4(a)	Wild type	CMP ⇒ MON	Spontaneous-differentiation
		MEP ⇒ GMP	Off-differentiation
		MEG ⇔ CMP	High separation
		MEP ⇒ GMP	Off-differentiation
		MEP ⇔ MEG	Low separation
Figure 4(b)	EgrNab/Gfi-1	CMP ⇒ MEG	Spontaneous-differentiation
		ERY ⇒ GRA	Transdifferentiation
		GRA ⇔ CMP	Low separation
Figure 4(c)	Fli-1/EKLF	MEG ⇒ CMP	Spontaneous-dedifferentiation
		MEG ⇒ MON	Transdifferentiation
		MEG ⇒ GMP	Off-differentiation
		MEG ⇔ MON	Low separation
		GMP ⇔ MON	High separation
Figure 5(b)	GATA-2/PU.1	GRA ⇒ CMP	Spontaneous-dedifferentiation
		MEP ⇒ MON	Off-differentiation
		GMP ⇒ ERY	Off-differentiation
		GMP ⇒ MEG	Off-differentiation
Figure 5(c)	GATA-1/PU.1	MON ⇒ GMP	Transdifferentiation

fix the value of the link from transcription factor EgrNab to transcription factor Gfi-1 in the network shown in Figure 3.

A key point in interpreting the visualized lineage networks is understanding flux and separation. For example, in the wild-type network of Figure 4, note the wide spacing between the granulocyte (GRA; orange) and megakaryocyte-erythrocyte precursor (MEP; green) cells and the narrowness of the arrow that connects these cells. The large distance indicates that there is a low probability for this cell type transition, the direction of the arrow shows the overall direction of this infrequent transition, and the narrow width of the arrow indicates that there is relatively little difference between the forward and reverse rates of the transitions between these cells. Therefore, this is an infrequent and low flux transition. Similarly, the wide separation and lack of an arrow (signalling a very low flux) indicate that granulocyte (GRA; orange) and monocyte (MON; pink) terminal differentiation is stable and transdifferentiation is rare.

Contrast this with the arrow connecting the monocytes (MON; pink) and common myeloid precursor (CMP; dark blue) cells shown in the same row of the figure. The separation between these cell types is small, indicating a low MFPT and a high probability of this transition and the thick arrow connecting the CMP to the MON cells indicates the overall direction of the cell state transition (CMP to MON) and that the rate of the CMP to MON forward transition far exceeds the rate of the reverse transition. Therefore, this is a frequent and high flux transition. The ability to rotate this graph freely using the VRML viewer tool adds to the utility of the visualization as the viewer can explore the relationships between all pairs of cell types within this, or any other, lineage network.

Comparisons of the wild-type network with mutated networks in which one of the interactions between transcription factors is blocked reveal strong differences in lineage network organization. For instance, in the bottom panel of Figure 4, our visualization method immediately demonstrates major alterations in the lineage tree due to blocking Fli-1′s regulation of EKLF. In this case, two cell types, megakaryocyte-erythrocyte progenitor (MEP) and erythrocytes (ERY), are no longer present.

Finally, the technique developed here is able to reveal many different kinds of transitions between cell states (Table 2). Although a GRN that produces attractors that correspond to myeloid cell types was used in this initial study, any GRN and its resulting attractors/cell types can be explored using this approach. Significantly, nonstandard transitions, such as dedifferentiation, off-differentiation, and transdifferentiation, are increasingly recognized in normal and disease states, many of which cannot be shown using conventional lineage trees. Our method allows their representation in 3-dimensional space and provides important information on their likelihood under either gene expression noise as shown here, or other driving forces in GRN dynamics.

3. Methods

3.1. Cell Differentiation and Attractor Dynamics. First proposed by Kauffman [17], Boolean networks are one of the main contributors to our current knowledge of gene regulatory networks. They have proved effective in representing many biological systems including *Drosophila* development [21, 22], angiogenesis [23], eukaryotic cell dynamics [24], and yeast transcription networks [25]. Boolean networks consist of nodes and directed edges. In GRN modeling, nodes represent the genes and edges represent the regulatory influences between the genes. These regulatory influences are

fully defined by the updating rules for each gene as a logic function of the inputs. A gene can be either expressed (the output is true) or not expressed (the output is false).

A Boolean network with n genes has 2^n possible states, denoted as $\widehat{S}$. Each network state $\widehat{s}_t$ is the collection of all gene values at time t, $\widehat{s}_t = \{g_1, g_2, \ldots, g_n\}$. Given the current state $\widehat{s}_t$, the next network state $\widehat{s}_{t+1}$ is obtained by applying each gene's function to the the current gene values. The gene's logic functions are deterministic. Thus, the the mapping function $D(\widehat{s}_t)$ that finds the next network state is also deterministic: $\widehat{s}_{t+1} \leftarrow D(\widehat{s}_t)$. By repeatedly applying deterministic updating, the network dynamics will eventually reach a previously visited state. This cycle is called an attractor ($\widehat{a}$). Attractors can be single states, called point attractors or cyclic attractors in which the cycle consists of more than one state. Note that to find all attractors of a given network all possible starting states need to be considered (the code can be obtained from http://code.google.com/p/pbn-matlab-toolbox).

In this work, cell types are considered attractors in the state space of possible gene expression profiles [26] and cell differentiation is modeled as the process of transitioning from one attractor to another [6].

3.2. Simulating and Measuring Noise Dynamics. Noise at the molecular level plays a key role in many biological processes including protein folding, transcription factor binding to DNA, and the rate of initiating transcription and translation [27, 28]. At the systems level, noise influences the likelihood of cell type transitions [26]. Noise can be modeled in Boolean regulatory networks by random bit flips during network operation, with these bit flips representing noise-driven changes in gene expression. Let $\widehat{s}_j \leftarrow \eta(\widehat{s}_i, r)$ be the spontaneous noise function that maps a state of the network $\widehat{s}_i$ to a new state $\widehat{s}_j$ with the addition of noise, implemented as r bit flips, with each single bit flip occurring with probability p. Noise modifies the probability of state transitions as the states are updated and the switching among network attractors. Since attractors represent cell types, measures of noise tolerance can estimate the magnitude of the barrier between attractors, the so-called epigenetic barrier. In the following section, three measures of the epigenetic barrier are introduced and compared.

3.2.1. Hamming Distance. Hamming distance is the direct measure of the difference between corresponding elements of two bit vectors. In GRNs, Hamming distance measures the differences in expression levels between two network states. Differences between gene expression profiles are used to identify cell type or cell physiology [29]. However, as a measure of the epigenetic barrier between states, Hamming distance does not utilize $\eta(\widehat{s}, r)$ and also ignores the constraints that regulatory network dynamics impose upon state transitions $D(\widehat{s})$. For these reasons, Hamming distance is a poor measure of the epigenetic barrier.

3.2.2. Transitory Perturbation (Single-Bit-Flip). An alternative measure of the likelihood of attractor transition under expression noise was introduced by Villani et al. [30]. Once the set of attractors is identified, this measure inserts noise as a single bit flip one-off event followed by deterministic updating. So given $\widehat{a}_i$ as an attractor state, $\widehat{s}_i \leftarrow \eta(\widehat{a}_i, 1)$ is applied to a single bit, and then the network defined updating rules are applied determinatively until an attractor state $\widehat{a}_j \leftarrow D^*(\widehat{s}_i)$ is reached. For each attractor and each bit, the process is repeated. Let $c_{i,j}, 1 \le i, j \le m$ (where m is the number of attractors), be the count of cases when $\widehat{a}_j \leftarrow D^*(\eta(\widehat{a}_i, 1))$. Then, $P(\widehat{a}_i, \widehat{a}_j) = c_{i,j}/m$. For each pair of attractors $\{\widehat{a}_i, \widehat{a}_j\}$, $P(\widehat{a}_i, \widehat{a}_j)$ is the portion of single one-step bit flips (transitory perturbations) in the nodes of all states of attractor $\widehat{a}_i$ which will result in a transition from $\widehat{a}_i$ to $\widehat{a}_j$ under noise-free dynamics.

This single-bit-flip measure of likelihood of network transition under noise efficiently estimates the epigenetic barrier (since it is $O(nm)$), but it assumes that expression noise is an infrequent event during network dynamics.

3.3. Mean First Passage Time. Introduced by Shmulevich et al. [16], mean first passage time (MFPT) is the the average time it takes to reach state y from state x in the presence of noise. Mathematically, first passage time (FPT) is defined as $F_k(\widehat{s}_x, \widehat{s}_y)$, the probability that starting in state $\widehat{s}_x$; the first time the system visits a state $\widehat{s}_y$ will be at time k; in Boolean networks, time is measured as the number of state updates. MFPT is then defined as

$$\mathrm{MFPT}\left(\widehat{s}_x, \widehat{s}_y\right) = \sum_k k F_k\left(\widehat{s}_x, \widehat{s}_y\right), \tag{4}$$

where the F_k itself is formulated as

$$F_k\left(\widehat{s}_x, \widehat{s}_y\right) = \sum_{\widehat{s}_z \in \{0,1\}^n, z \neq y} p_{xz} F_{k-1}\left(\widehat{s}_z, \widehat{s}_y\right). \tag{5}$$

In this recursive formula, $F_1(\widehat{s}_x, \widehat{s}_y)$ is the probability of direct transition from state $\widehat{s}_x$ to $\widehat{s}_y$. p_{xz} is the probability of transition from state $\widehat{s}_x$ to state $\widehat{s}_z$. Probabilistically, there are two ways to reach state $\widehat{s}_z$ from $\widehat{s}_x$; either $\widehat{s}_z$ is a deterministic target for $\widehat{s}_s$ and no bit flips occur due to the noise or an aggregate of bit flips drives the transition from $\widehat{s}_x$ to $\widehat{s}_z$.

When the MFPT between two states is low, it implies that, starting from the first state, the second state is easily reached by molecular noise. Figure 6 shows F_k and kF_k for the transition between two arbitrary attractors. As this figure shows, the b to a transition has a lower MFPT compared with a to b. Note that when an attractor has more than one state; that is, it is a cyclic attractor, the MFPT is calculated for each state separately and then is averaged over all states of that attractor.

At each network state update $D(\widehat{s})$ there is a probability that the state will change as a function of the Hamming distance (h) between the current state and the subsequent state $\widehat{s}_{t+1} \leftarrow D(\eta(\widehat{s}_t, r))$. MFPT models uniform expression noise by considering probabilistic bit flips at every possible state of the network and deriving the distribution of passage times from analysis of the corresponding Markov process. Statistically, the probability distribution of bit flips can be seen as a binomial distribution, and thus the probability of r bit flips, $\eta(\widehat{s}_a, r)$, is $\binom{n}{r} p^r (1-p)^{n-r}$, where p is the probability of a single bit flip and n is the total number of bits.

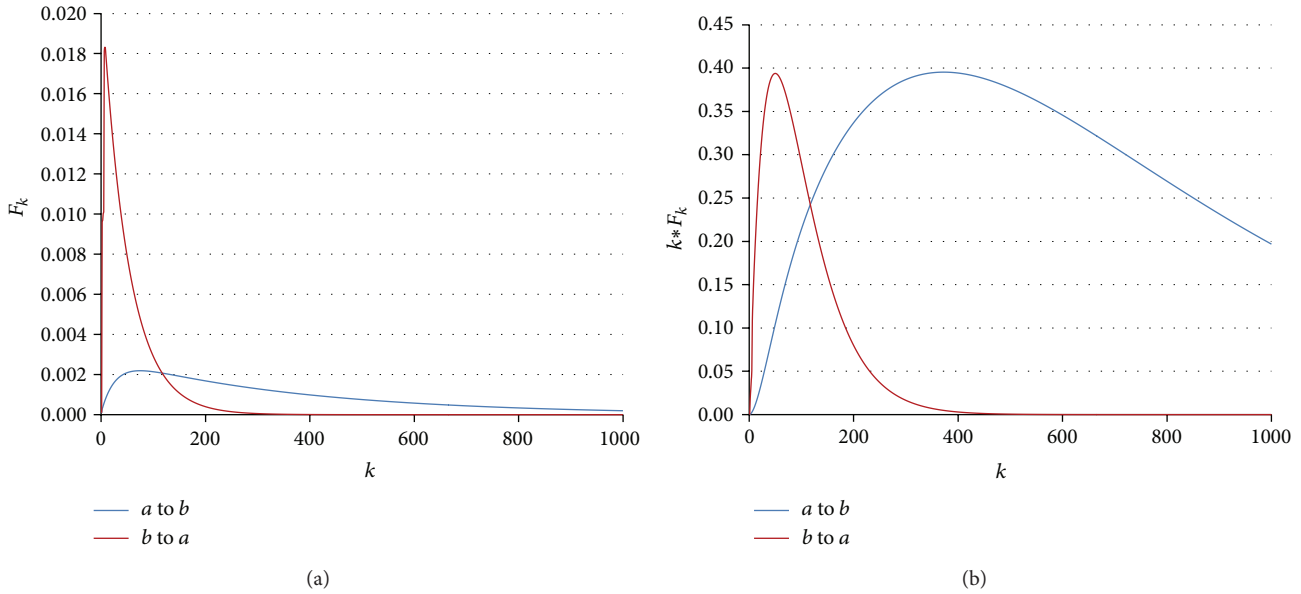

FIGURE 6: (a) F_k (probability of first visit at time step k) plotted for two arbitrary attractors, called a and b in a random Boolean network for 1000 steps (k). The red curve is for the transition from b to a that has a low MFPT compared to the reverse transition; a to b is shown with the blue curve; (b) kF_k plotted for the F_k curves in (a). Note that MFPT is the centroid of the area under the kF_k curve.

Mean first passage time quantifies the epigenetic barriers between all attractor states during network execution. Therefore, this work only considers MFPT because of its realism in modeling expression noise. However, the time required for MFPT computation is an exponential function of the number of genes, so if the number of genes in the network is large, calculating MFPT may become intractable. In this case, transitory perturbation can be used as a possible alternative.

4. Summary

In this work, we developed a technique and a supporting method for visualization, *CellDiff3D*, that estimates the likelihood and directionality of noise-driven transitions between different cell types and allows the three-dimensional visualization of these relationships. A Boolean network model of myeloid cell differentiation [4] was used as a demonstration system for this research.

The metric of mean first passage time (MFPT) assesses the likelihood that noise in the GRN for myeloid differentiation will trigger a transition between cell types. Low MFPT values indicate a high probability of a cell type transition. The difference in MFPTs for forward (cell type A to cell type B) and reverse (cell type B to cell type A) transitions provides a measure termed flux. Flux is analogous to the difference in forward and reverse rates of a chemical reaction and it gives the anticipated direction and the strength of the directionality in transitions between cell types.

Our technique calculated the MFPT separation and flux between all pairs of cell types in a simplified myeloid lineage tree that included one multipotent stem cell, two intermediate cells, and four terminal cell types to produce a graph to display all 42 pairwise relationships $m(m-1)$ where $m = 7$ between the myeloid cell types. A VRML-based graphics tool was employed as part of *CellDiff3D* to visualize all attractor type transitions by placing all pairs of different cell types in 3-dimensional space. It shows the likelihood of a transition between cell types as the separation between each pair and the directionality of the transition as arrows with a width proportional to the flux. The VRML output, viewable in any web browser (with the proper plugin), allows the free rotation and zooming of the differentiation network to reveal its features. It can be used for any cell differentiation network, can include many more than the 7 cell types considered here, and is capable of showing all possible transitions (e.g., dedifferentiation and transdifferentiation) between different types of cells. Our technique readily revealed changes in the dynamics of mutationally altered myeloid differentiation networks, the loss of cell types, and unusual cell type transitions that included dedifferentiation, transdifferentiation, and off-differentiation.

This work has introduced a 3D graph approach to visualize the influence of noise on cell type switching of wild-type and mutated regulatory networks. However, the system is not limited to noise analysis and can incorporate other influences that drive cell type switching. The *CellDiff3D* tool can be downloaded from http://www.celldiff3d.org/.

Conflict of Interests

The authors declare that there is no conflict of interests regarding the publication of this paper.

Authors' Contribution

Ahmadreza Ghaffarizadeh, Gregory J. Podgorski, and Nicholas S. Flann conceived the system and wrote the text.

Ahmadreza Ghaffarizadeh designed and implemented the software and performed all the experiments.

Acknowledgments

Research reported in this paper was supported by the National Institute Of General Medical Sciences of the National Institutes of Health under Award no. P50GM076547, Luxembourg Centre for Systems Biomedicine, the University of Luxembourg, and the Institute for Systems Biology, Seattle, USA. Thanks are due to Ilya Shmulevich and Merja Heinaniemi for helpful discussions. The content is solely the responsibility of the authors and does not necessarily represent the official views of the National Institutes of Health.

References

[1] S. Huang, "Reprogramming cell fates: reconciling rarity with robustness," *BioEssays*, vol. 31, no. 5, pp. 546–560, 2009.

[2] T. Masaki, J. Qu, J. Cholewa-Waclaw, K. Burr, R. Raaum, and A. Rambukkana, "Reprogramming adult Schwann cells to stem cell-like cells by Leprosy Bacilli promotes dissemination of infection," *Cell*, vol. 152, no. 1, pp. 51–67, 2013.

[3] J. P. Their, "Epithelial-mesenchymal transitions in tumor progression," *Nature Reviews Cancer*, vol. 2, no. 6, pp. 442–454, 2002.

[4] J. Krumsiek, C. Marr, T. Schroeder, and F. J. Theis, "Hierarchical differentiation of myeloid progenitors is encoded in the transcription factor network," *PLoS ONE*, vol. 6, no. 8, Article ID e22649, 2011.

[5] S. Huang, G. Eichler, Y. Bar-Yam, and D. E. Ingber, "Cell fates as high-dimensional attractor states of a complex gene regulatory network," *Physical Review Letters*, vol. 94, no. 12, Article ID 128701, 2005.

[6] H. H. Chang, M. Hemberg, M. Barahona, D. E. Ingber, and S. Huang, "Transcriptome-wide noise controls lineage choice in mammalian progenitor cells," *Nature*, vol. 453, no. 7194, pp. 544–547, 2008.

[7] D. Orrell and H. Bolouri, "Control of internal and external noise in genetic regulatory networks," *Journal of Theoretical Biology*, vol. 230, no. 3, pp. 301–312, 2004.

[8] S. Huang, I. Ernberg, and S. Kauffman, "Cancer attractors: a systems view of tumors from a gene network dynamics and developmental perspective," *Seminars in Cell and Developmental Biology*, vol. 20, no. 7, pp. 869–876, 2009.

[9] L. T. MacNeil and A. J. M. Walhout, "Gene regulatory networks and the role of robustness and stochasticity in the control of gene expression," *Genome Research*, vol. 21, no. 5, pp. 645–657, 2011.

[10] Q. Hu, A. M. Friedrich, L. V. Johnson, and D. O. Clegg, "Memory in induced pluripotent stem cells: reprogrammed human retinal-pigmented epithelial cells show tendency for spontaneous redifferentiation," *Stem Cells*, vol. 28, no. 11, pp. 1981–1991, 2010.

[11] C. H. Waddington, *The Strategy of Genes*, George Unwin & Unwin, 1957.

[12] C. Furusawa and K. Kaneko, "A dynamical-systems view of stem cell biology," *Science*, vol. 338, no. 6104, pp. 215–217, 2012.

[13] N. Suzuki, C. Furusawa, and K. Kaneko, "Oscillatory protein expression dynamics endows stem cells with robust differentiation potential," *PLoS ONE*, vol. 6, no. 11, Article ID e27232, 2011.

[14] J. X. Zhou, M. D. S. Aliyu, E. Aurell, and S. Huang, "Quasi-potential landscape in complex multi-stable systems," *Journal of the Royal Society Interface*, vol. 9, no. 77, pp. 3539–3553, 2012.

[15] S. Bhattacharya, Q. Zhang, and M. Andersen, "A deterministic map of Waddington's epigenetic landscape for cell fate specification," *BMC Systems Biology*, vol. 5, article 85, 2011.

[16] I. Shmulevich, E. R. Dougherty, and W. Zhang, "Gene perturbation and intervention in probabilistic Boolean networks," *Bioinformatics*, vol. 18, no. 10, pp. 1319–1331, 2002.

[17] S. A. Kauffman, "Metabolic stability and epigenesis in randomly constructed genetic nets," *Journal of Theoretical Biology*, vol. 22, no. 3, pp. 437–467, 1969.

[18] Y. Xue, K. Ouyang, J. Huang et al., "Direct conversion of fibroblasts to neurons by reprogramming PTB-regulated MicroRNA circuits," *Cell*, vol. 152, pp. 82–96, 2013.

[19] T. Vierbuchen, A. Ostermeier, Z. P. Pang, Y. Kokubu, T. C. Südhof, and M. Wernig, "Direct conversion of fibroblasts to functional neurons by defined factors," *Nature*, vol. 463, no. 7284, pp. 1035–1041, 2010.

[20] J. Ellson, E. R. Gansner, E. Koutsofios, S. C. North, and G. Woodhull, "Graphviz and dynagraph—static and dynamic graph drawing tools," *Graph Drawing Software*, pp. 127–148, 2003.

[21] R. Albert and H. G. Othmer, "The topology of the regulatory interactions predicts the expression pattern of the segment polarity genes in Drosophila melanogaster," *Journal of Theoretical Biology*, vol. 223, no. 1, pp. 1–18, 2003.

[22] J. W. Bodnar, "Programming the *Drosophila* Embryo," *Journal of Theoretical Biology*, vol. 188, no. 4, pp. 391–445, 1997.

[23] A. L. Bauer, T. L. Jackson, Y. Jiang, and T. Rohlf, "Receptor cross-talk in angiogenesis: mapping environmental cues to cell phenotype using a stochastic, Boolean signaling network model," *Journal of Theoretical Biology*, vol. 264, no. 3, pp. 838–846, 2010.

[24] I. Shmulevich, S. A. Kauffman, and M. Aldana, "Eukaryotic cells are dynamically ordered or critical but not chaotic," *Proceedings of the National Academy of Sciences of the United States of America*, vol. 102, no. 38, pp. 13439–13444, 2005.

[25] S. Kauffman, C. Peterson, B. Samuelssont, and C. Troein, "Random Boolean network models and the yeast transcriptional network," *Proceedings of the National Academy of Sciences of the United States of America*, vol. 100, no. 25, pp. 14796–14799, 2003.

[26] A. C. Huang, L. Hu, S. A. Kauffman, W. Zhang, and I. Shmulevich, "Using cell fate attractors to uncover transcriptional regulation of HL60 neutrophil differentiation," *BMC Systems Biology*, vol. 3, article 20, 2009.

[27] A. Bar-Even, J. Paulsson, N. Maheshri et al., "Noise in protein expression scales with natural protein abundance," *Nature Genetics*, vol. 38, no. 6, pp. 636–643, 2006.

[28] G. Tkačik, T. Gregor, and W. Bialek, "The role of input noise in transcriptional regulation," *PLoS ONE*, vol. 3, no. 7, Article ID e2774, 2008.

[29] L. Bruno, R. Hoffmann, F. McBlane et al., "Molecular signatures of self-renewal, differentiation, and lineage choice in multipotential hemopoietic progenitor cells in vitro," *Molecular and Cellular Biology*, vol. 24, no. 2, pp. 741–756, 2004.

[30] M. Villani, A. Barbieri, and R. Serra, "A dynamical model of genetic networks for cell differentiation," *PLoS ONE*, vol. 6, no. 3, Article ID e17703, 2011.

Hindawi Publishing Corporation
Computational and Mathematical Methods in Medicine
Volume 2014, Article ID 258627, 8 pages
http://dx.doi.org/10.1155/2014/258627

Research Article

Designing Lead Optimisation of MMP-12 Inhibitors

Matteo Borrotti,[1,2] Davide De March,[1,2] Debora Slanzi,[1,2] and Irene Poli[1,2]

[1] *European Centre for Living Technology, 30124 Venice, Italy*
[2] *Department of Environmental Sciences, Informatics and Statistics, Ca' Foscari University of Venice, 30123 Venice, Italy*

Correspondence should be addressed to Irene Poli; irenpoli@unive.it

Received 9 October 2013; Revised 16 December 2013; Accepted 16 December 2013; Published 12 January 2014

Academic Editor: Rudolf Füchslin

The design of new molecules with desired properties is in general a very difficult problem, involving heavy experimentation with high investment of resources and possible negative impact on the environment. The standard approach consists of iteration among formulation, synthesis, and testing cycles, which is a very long and laborious process. In this paper we address the so-called lead optimisation process by developing a new strategy to design experiments and modelling data, namely, the evolutionary model-based design for optimisation (EDO). This approach is developed on a very small set of experimental points, which change in relation to the response of the experimentation according to the principle of evolution and insights gained through statistical models. This new procedure is validated on a data set provided as test environment by Pickett et al. (2011), and the results are analysed and compared to the genetic algorithm optimisation (GAO) as a benchmark. The very good performance of the EDO approach is shown in its capacity to uncover the optimum value using a very limited set of experimental points, avoiding unnecessary experimentation.

1. Introduction

Designing molecules with particular properties is usually a long and complex process, in which the nonlinearity of the model, the high number of variables with a leading role, and the categorical structure of these variables can make difficult modelling, experimentation, and analysis. In new drug discovery, a key phase concerns the generation of small molecules modulators of protein function, under the hypothesis that this activity can affect a particular disease state. Current practices rely on the screening of vast libraries of small molecules (often 1-2 million molecules) in order to identify a molecule that specifically inhibits or activates the protein function, commonly known as the lead molecule. The lead molecule interacts with the required target, but it generally lacks the other attributes needed for a drug candidate such as absorption, distribution, metabolism, and excretion (ADME). In order to achieve these attributes, retaining the interaction capacity with the target protein, the lead molecule must be modified. This transformation of the lead molecule is known as lead optimisation. Lead optimisation research involves long synthesis and testing cycles, analyses of the structure-activity relationships (SAR), and quantitative structure activity relationships (QSAR), which are currently the bottleneck of this process [1]. Under traditional approaches these analyses are conducted by experimentation involving an extremely large number of experimental units, which requires large investments of resources and time to reach the target and measure the possible impact on the environment. Computational approaches for the SAR and QSAR analyses, mostly based upon machine learning techniques, have been proposed over the last few years [2–5]. Search and optimisation algorithms inspired by evolution have been also developed and applied with success to drug discovery process and related activities. In Clark [6], different evolutionary algorithms are presented and discussed, such as genetic algorithms (GAs), evolutionary programming (EPs), and evolution strategies (ESs). In this work, several applications of these computational methods have been derived for a wide range of research. Other bio-inspired algorithms such as Ant Colony Optimisation (ACO) and Artificial Neural Networks (ANNs) have been applied in drug discovery [7]. The evolutionary principle is the basic structure of a new approach proposed for designing experiments in an efficient

way [8–12]. In this paper we would like to contribute to the development of this research by proposing a new procedure with the objective of finding the optimal value of MMP-12 conducting a very small number of tests and thus with small investments of resources and limited negative impact on the environment. This new procedure is an evolutionary model-based design of experiments: the search for the optimum value is restricted to relatively few experimental points, chosen with the evolutionary paradigm and the information provided by statistical models. Starting from lead molecules, randomization augmented by expert knowledge is used to choose the initial set of compositions to be tested in the laboratory. After chemical synthesis and in vitro screening of these molecules, the resulting response data are evaluated with respect to their capacity to reach the target. They are then transformed according to the operators involved in the evolutionary search and to the information from statistical models estimated on the data. Successive populations of molecules are analysed, modelled, and transformed to generate compositions that are closer to the optimum value. The procedure will be developed and validated, and its efficiency will be measured by a suitable index. Given the successful performance of the simple genetic algorithm for lead optimisation of MMP-12 inhibitors developed by Pickett et al. [1], we will compare our procedure with GAO on this problem. To allow the comparison we will consider the same number of experimental points considered in Pickett et al. [1]. Results exhibit a better performance of our approach in reaching the optimum value and reducing the number of experiments. The paper is organised as follows: in Section 2 we describe the data set on which we developed the procedure and the key idea of the proposed design. In Section 3 we present the results and make comparison with the GAO approach. Section 4 offers some concluding remarks.

2. Materials and Methods

2.1. Data Set. We build the design for optimisation using a data set presented and analysed by Pickett et al. [1]. These data, available at http://pubs.acs.org, have been constructed by the authors as a test environment on which assessing the effectiveness and the efficiency of new designs for lead optimisations. The data concern a library of 2500 molecules, identified by their chemical compositions (*reagents*) and their experimental response (*activity*). These data represent the whole experimental space. Each data point, coding a particular experiment, is described by two categorical variables, which represent the reagents, each of which can assume 50 different values. The response variable measures the molecular activity of the reaction product. The aim of the analysis is to find the reaction whose product maximises the molecular activity. As a first exploratory analysis of these data we compute a set of descriptive statistics to get some insights into the frequency distribution of the response variable. These data are represented in Figure 1, reporting the histogram and the boxplot. From the exploratory analysis we learn that the maximum value of the molecular activity is 8.00 and the minimum value is 3.40. The mean of the response is equal to 5.28 and the median 5.20; the first quartile is 4.40 and the third quartile is 6.20. These values indicate a right-skewed distribution, and this particular shape is clearly shown in the histogram. In designing experiments for optimisation we will have the objective to find the experimental point with the maximum value of 8.00.

To describe the behaviour of the response in relation to the molecule composition, we built a *heatmap plot* as presented in Figure 2. The two reagents, say reagents A and B, are reported in the axes of the plot with 50 levels each. For each combination of the reagent levels we can read the value of the molecular activity: high activity values are represented by dark blue squares and small activity values by light blue squares. White squares indicate molecules for which the response is not available. From Figure 2 we can see that just two molecule compositions reach the maximum value of 8.00 (A21; B07 and A31; B25, marked by red circle); also we notice that some reagents, B16 and B20, can give rise to molecules with very high activity values.

2.2. Design for Optimisation. An *optimisation* problem is commonly described as follows.

Let S be a subset of the Euclidean space $\mathbb{R}^d$ and let f be the function $f : S \to \mathbb{R}^+$. Let $\mathbf{x} = (x_1, \ldots, x_d)$ be a point in S; $\mathbf{x}$ can affect the response variable y, and the response can then be described as $y = f(x_1, \ldots, x_d)$. The optimisation problem consists in searching the element $\mathbf{x}^*$ in S such that $f(\mathbf{x}^*) \geq f(\mathbf{x})$ for all $\mathbf{x}$ in S.

For the lead optimisation problem that we are addressing in this research the dimension d equals 2, since two variables are considered in the dependence relation.

These variables are categorical variables, namely, the reagents, and can take $l = 50$ different levels.

With this setting of the problem the experiment is run to provide each experimental point with a response value that is a measure of the activity of the resulting molecule. The experimental data set is then $(\mathbf{X}; \mathbf{y})$, with $\mathbf{X}$ being an $(N \times 2)$-matrix, where $N = 2500$ is the size of S, and $\mathbf{y}$ being an N-vector. This data set represents the evidence for inferring the dependence relation among variables and identifies the design point that gives the optimum value of the response.

The *design* problem for optimisation consists in finding a small set of experimental points that contain the relevant information to reach the optimal value. Our contribution to address this problem is to adopt evolution as a paradigm to build a design approach guiding the evolution with the information achieved by statistical models.

2.3. Evolutionary Design for Optimisation. Building on the evolutionary strategy we introduce a new approach, named evolutionary design for optimisation (EDO), testing a very small set of different experimental points able to find the optimal response value or the region of optimality. This approach evolves an initial design through K generations by means of a set of genetic operators (selection, recombination, and mutation) that are built on the information provided by models estimated on the data of each design generation $(\mathbf{X_k}; \mathbf{y_k})$, $k = 1, \ldots, K$.

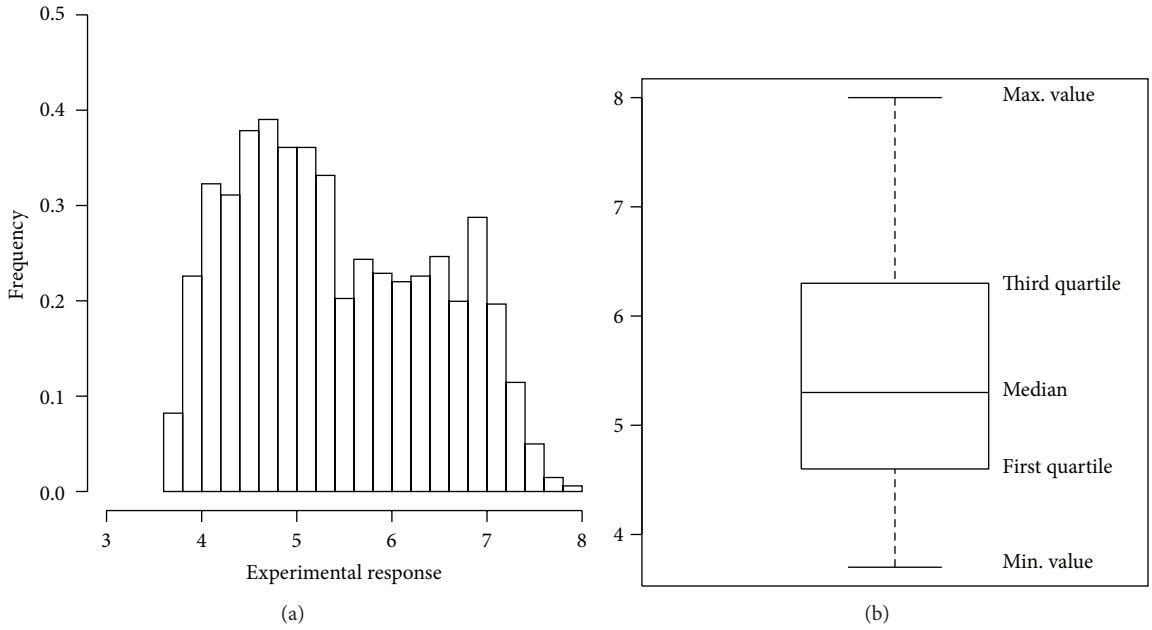

FIGURE 1: (a) Histogram and (b) boxplot of the experimental response variable.

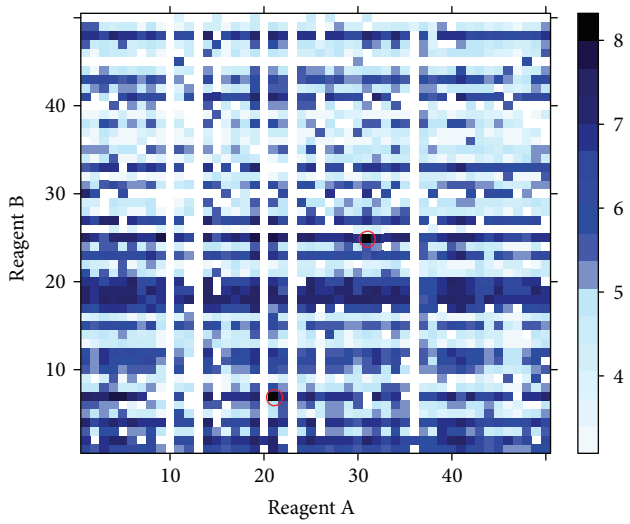

FIGURE 2: Heatmap for the whole experimental space: 2500 molecules evaluated with respect to their activity. Each square represents a molecule and the colour describes the intensity of the activity, from the light blue to the dark blue. Red circles mark the optimal molecules. White squares represent molecules with not available response.

For the lead optimisation problem addressed in this research we build the EDO approach with the objective of achieving the optimum value of the molecule activity testing 140 experimental points as in genetic algorithm optimisation (GAO) strategy introduced by [1]. More specifically, we select an initial population of experimental points $\mathbf{X}_1$, consisting of two sets of compounds: the first set is created by assigning at each level of reagent A a randomly selected level of reagent B; then, the second set is created by assigning at each level of reagent B a randomly selected level of reagent A. Each of these sets include 50 compounds, and then the design consists of $m_1 = 100$ different compounds. Each of these experimental points receives a response value $\mathbf{y_1}$. Therefore on the data set $(\mathbf{X_1}; \mathbf{y_1})$, a statistical model is estimated to achieve information on the goodness of these compositions in reaching the target of the optimisation. In this research we developed several Monte Carlo simulation studies comparing different classes of statistical models in their predictive capacity, and we selected the random forest model [13–15] as our best choice. The random forests are regression methods frequently used when the relationship between response and predictors is complex, and the predictors are categorical variables [16].

Following the evolutionary paradigm, we then adopt a selection operator where the probability of each experimental point to be selected for next generation is proportional to the square of the response value, according to the following expression:

$$\pi_i = \frac{y_i^2}{\sum_{i=1}^{n} y_i^2}, \tag{1}$$

where n is the total number of experimental points tested up to and including the current generation. For this optimisation problem we select 10 compounds, and each selected compound is then recombined in order to create a set of new and not already tested points. We estimate a random forest model and proceed in the following way: for each selected compound we fix the reagent, randomly chosen between A and B, and its corresponding level in the compound, and then we generate all the possible compounds by changing the 50 levels of the other reagent. For all these new generated experimental points we then predict the responses using

the estimated random forest model and the compound with the highest estimated response value is considered for the following generation. A mutation operator is then performed (with probability $P = 0.05$) by randomly changing one reagent level. The second population of $m_2 = 10$ experimental points $\mathbf{X_2}$ is then defined. We iterate the procedure across generations until the optimum value is archived or a stopping rule is satisfied.

The EDO procedure is represented in Figure 3 and described as follows.

(1) Create a population of m_1 compounds ($m_1 = 100$).

(2) Conduct experimentation and evaluate the response.

(3) Estimate the statistical model (i.e., random forest).

(4) Select a compound (according to (1)).

(5) Combine the reagents using EDO crossover as follows:

  (i) select a reagent in a random way;

  (ii) generate all the possible compounds by changing the 50 levels of the other reagent;

  (iii) infer the molecules activity with the estimated model (random forest);

  (iv) select the compound with the highest estimated activity value for next generation.

(6) Repeat step's 4 and 5 until the 10 new compounds are created.

(7) Mutate the new compounds with $p = 0.05$.

(8) Conduct experimentation and evaluate the response.

(9) If number of generations is equal to K stop the algorithm. Otherwise repeat steps from 3 to 8.

The EDO procedure is developed in R code (http://cran.r-project.org/) and uses `randomForest` package [16]. Random forest model is estimated running 500 trees, and model selection is performed with standard parameterisation of the package.

2.4. Measure of the Design Goodness. To evaluate the design goodness we introduce two criteria. The first criterion is a measure of the distance between the response value of the best experimental point provided by the design and the actual optimal value of the whole system response. In particular, let $\widehat{y}_{\max}$ be the maximum value found by the design, and let $y_{\max}$ and $y_{\min}$ be the known maximum and minimum of y on the whole search space. The design goodness for optimisation criterion (DGO) is

$$\mathrm{DGO} = 1 - \frac{\left|\widehat{y}_{\max} - y_{\max}\right|}{\left|y_{\min} - y_{\max}\right|}. \tag{2}$$

This measure ranges in value from 0 to 1. The second criterion of design goodness evaluates the capacity of the approach to find response values in defined regions of optimality. We derive this indicator by counting the number of experimental points with response value greater than a defined threshold. This threshold is identified by the right tail area of the response values distribution measured by the probability values $\alpha = 0.01$ and $\alpha = 0.05$. The DGO_α can be expressed as follows:

$$\mathrm{DGO}_\alpha = \frac{\sum_{i=1}^{m} I\left(y_i \geq y_\alpha\right)}{\sum_{j=1}^{N} I\left(y_j \geq y_\alpha\right)}, \tag{3}$$

where m is the total number of tested compounds, N is the number of compounds of the whole experimental space, y_α is the percentile of the response distribution at α level, and $I(\cdot)$ is the indicator function. The DGO_α ranges from 0 to 1, where $\mathrm{DGO}_\alpha = 0$ indicates that no compound selected by the design is in the optimal region and $\mathrm{DGO}_\alpha = 1$ indicates that all the selected compounds are in the optimal region.

3. Results

To derive an efficient design for the lead optimisation problem we apply the EDO design and search in the experimental space of 2500 compounds for the optimum value. The initial population of $m_1 = 100$ compounds sampled from the whole experimental space (as in Section 2.3) are spread in the response distribution as described in Figure 4.

This result and the evolution of the experimental response achieved by generations are shown in Figure 5 (response values greater than 6) where we notice that EDO finds the optimal value of 8.00 (global optimum of the whole experimental space) at the third generation. We also notice that this approach is able to find a set of very good values close to the optimum.

To evaluate the performance of the procedure we developed a comparison of the EDO approach with the GAO, which is considered as a benchmark for this new approach. Reporting the response values by generations of the GAO in Figure 6 (response values greater than 6) we observe that the simple GA, without the statistical modelling contribution, is not able to find the optimum value testing 140 compounds and conducting 10 generations of experiments. Moreover we notice that most of the GAO response values remain under the threshold of 7.50.

Since the GAO approach has shown very good performance with respect to the traditional approach in lead optimisation, the results achieved under EDO design can be regarded as satisfactory. The EDO design on this set of data discovers the global optimum testing just 120 compounds.

Computing the design goodness criterion presented in (2) we compare the optimal response values achieved by the GAO, ${}_{\mathrm{GAO}}\widehat{y}_{\max} = 7.60$, and by EDO, ${}_{\mathrm{EDO}}\widehat{y}_{\max} = 8.00$, with the known optimum value of the whole space and derive the following measures of design goodness:

$${}_{\mathrm{GAO}}\mathrm{DGO} = 0.90, \qquad {}_{\mathrm{EDO}}\mathrm{DGO} = 1.00, \tag{4}$$

confirming the superior performance of the EDO design.

As a principal result the new procedure has been able to discover this value testing just 120 compounds and conducting 3 generations of the algorithm. Furthermore, the comparison in performance between EDO and GAO can

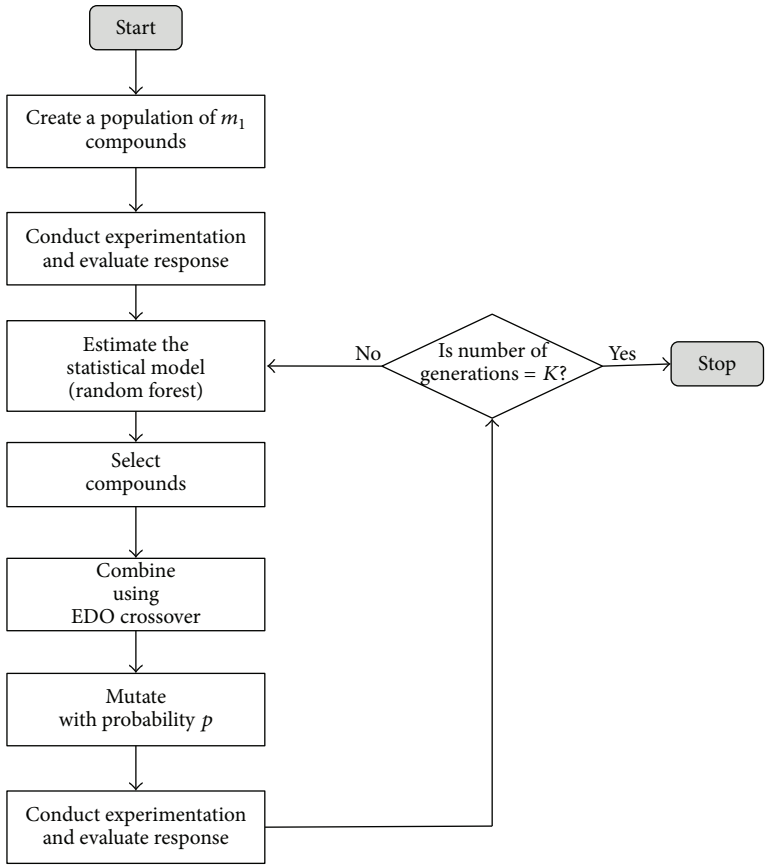

Figure 3: Flow diagram of EDO design for lead optimisation.

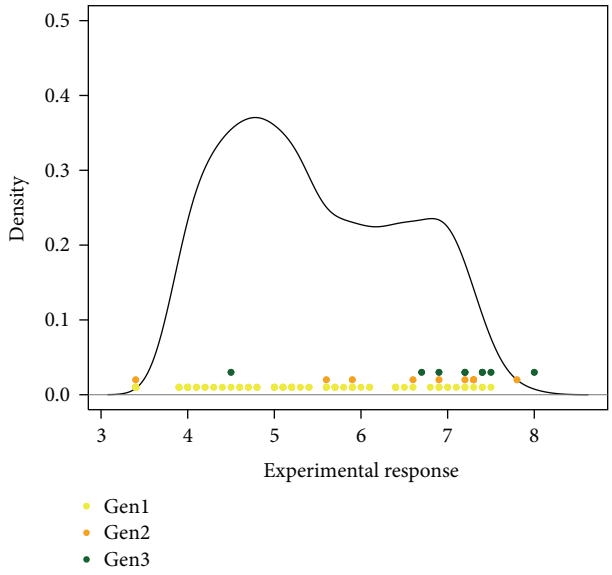

Figure 4: Estimated density function of response variable of the whole experimental space (2500 compounds). In yellow the response values of the initial population composed of $m_1 = 100$ compounds. The next populations, composed of $m_k = 10$ compounds, $k = 2, 3$, are represented by orange and green points.

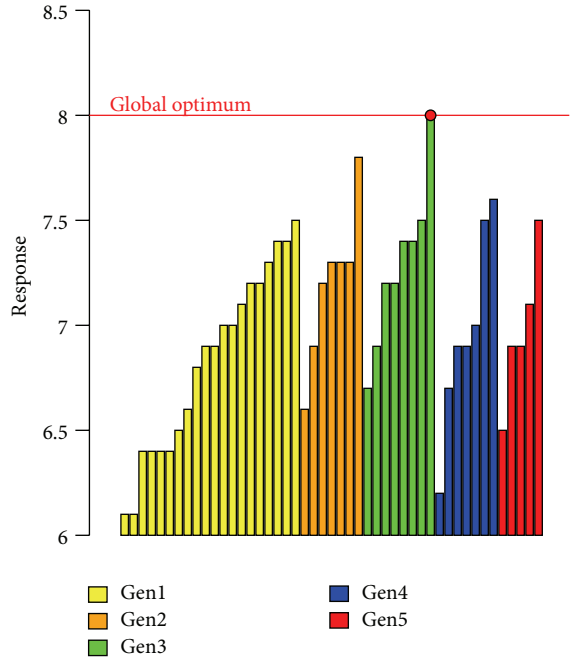

Figure 5: EDO response values greater than the threshold equal to 6, ordered by generation.

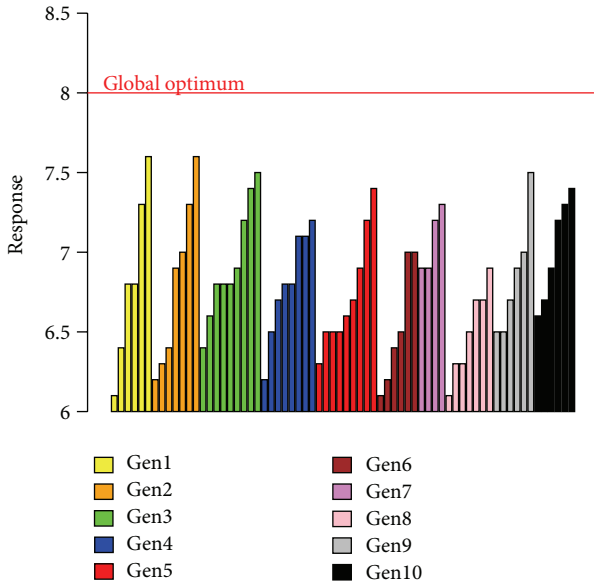

Figure 6: GAO response values greater than the threshold equal to 6, ordered by generation.

Table 1: Evaluation of the goodness of the design in terms of optimality area: the proportion of the best compounds found by EDO and GAO procedures over the given thresholds.

	Proportion of exp. points with responses in the optimality region (%)	
	EDO	GAO
$DGO_{0.01}$	29	17
$DGO_{0.05}$	21	16

be realised considering a region of optimality instead of the single optimal value.

Deriving the measure DGO_α, as presented in (3) for both optimisation approaches, we obtain that, in the right tail region of the distribution of the responses with $\alpha = 0.01$, the EDO approach can find 29% of the best compounds, while the GAO is able to discover just 17% of these compounds. We achieve similar results considering the region of the right tail distribution $\alpha = 0.05$, where EDO approach outperforms the results of GAO finding 21% of the best experimental units. These results are reported in Table 1.

We test the statistical significance of the null hypothesis that EDO and GAO have equal proportion of responses in the best response region. From this statistical test, we compute the one-tailed P value to evaluate the improvement of EDO compared to GAO: we obtain P value = 0.0991 considering the optimality region $\alpha = 0.01$ and P value = 0.1361 considering the optimality region $\alpha = 0.05$. These statistical tests confirm the improvement of EDO design compared to GAO design.

Studying the evolution of the proportion of the best compounds found in the optimality area and described in Figure 7, we notice that this proportion increases much faster and more intensively for the EDO design than for the GAO design. Selecting the region of optimality $\alpha = 0.01$ (Figure 7(a)) the number of responses from the EDO design that fall in this area increases rapidly reaching in 5 generations 29% of the best responses, instead of the 17% of the GAO design. Similar behaviour can be observed for the region of optimality with size $\alpha = 0.05$ (Figure 7(b)). Finally we derived the frequency distributions of the best response values ($y_i > 6.0$) comparing the EDO and GAO optimisation procedures, as described in Figure 8. We can observe that the proportion of the compounds achieved with EDO design (blue bars) grows for increasing values of the responses. Moreover for values greater than 7.5 this proportion is very high and is much higher than the proportion achieved with GAO procedure.

In order to study the robustness of EDO design with respect to changes in the initial population, we performed a simulative study where we run our algorithm 100 times with different initial populations.

As a result, 90% of the simulations have been able to find greater or equal response values with respect to the best result obtained in Pickett et al. [1]. This result shows the robustness of the EDO with respect to the choice of the initial population confirming the good performance of the approach.

4. Concluding Remarks

In this research we addressed the lead optimisation problem for drug discovery process by developing a design for experiments which is evolutionary and based on the information provided by statistical models. The motivation of this research is to give a contribution to the study of finding an efficient design that tests a very small set of experimental points instead of the whole space, which due to the high dimensionality of the system or the high number of the variable levels may be very large.

The approach that we derived outperforms the GAO methodology developed by Pickett et al. [1]. In fact selecting 120 experimental points from the whole search space, EDO is able to find the global optimum value. These results suggest that the development of an evolutionary design as in GAO is certainly successful in optimisation problems, but the introduction of statistical models at each step of the evolution as in EDO can improve the optimisation procedure.

Conflict of Interests

The authors declare that there is no conflict of interests regarding the publication of the paper.

Acknowledgments

The authors would like to acknowledge the European Centre for Living Technology (www.ecltech.org) for providing opportunities of presentations and fruitful discussions of the research. Thanks are due to the optimisation team in GlaxoSmithKline (www.gsk.com) led by Dr. Darren Green and Professor Philip Brown from University of Kent (www.kent.ac.uk) for valuable suggestions to this work. The

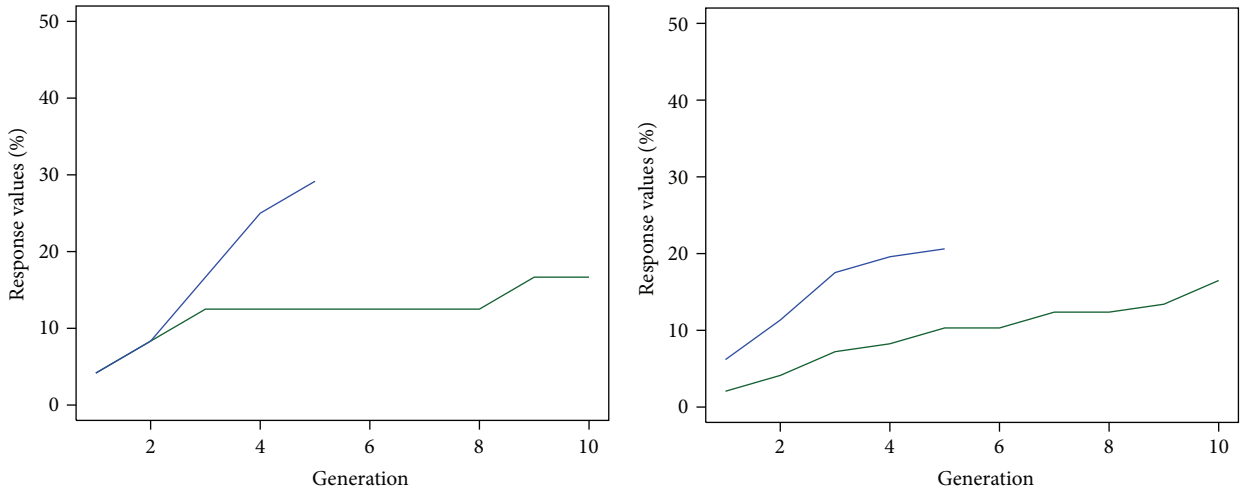

FIGURE 7: Evolution of the proportion of the best compounds found by the optimisation designs in the $\alpha = 0.01$ optimality region (a) and $\alpha = 0.05$ optimality region (b). The EDO design is represented by the blue line and the GAO by the green line.

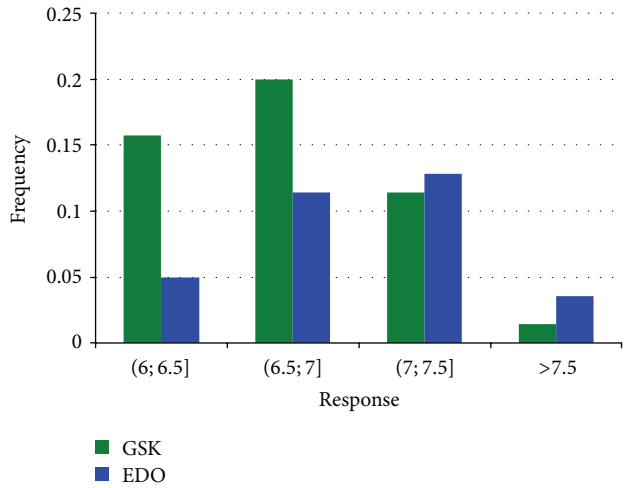

FIGURE 8: Frequency distribution of the response for values greater than the threshold equal to 6. EDO compounds are represented in blue, and GAO compound, are represented in green.

authors gratefully acknowledge the two anonymous reviewers and the editor for their helpful comments.

References

[1] S. D. Pickett, D. V. S. Green, D. L. Hunt, D. A. Pardoe, and I. Hughes, "Automated lead optimization of MMP-12 inhibitors using a genetic algorithm," *ACS Medicinal Chemistry Letters*, vol. 2, no. 1, pp. 28–33, 2011.

[2] A. Z. Dudek, T. Arodz, and J. Gálvez, "Computational methods in developing quantitative structure-activity relationships (QSAR): a review," *Combinatorial Chemistry and High Throughput Screening*, vol. 9, no. 3, pp. 213–228, 2006.

[3] M. Butkiewicz, R. Mueller, D. Selic, E. Dawson, and J. Meiler, "Application of machine learning approaches on quantitative structure activity relationships," in *Proceedings of the IEEE Symposium on Computational Intelligence in Bioinformatics and Computational Biology (CIBCB '09)*, pp. 255–262, April 2009.

[4] J. C. Stalring, L. A. Carlsson, P. Almeida, and S. Boyer, "AZOrange—high performance open source machine learning for QSAR modeling in a graphical programming environment," *Journal of Cheminformatics*, vol. 3, no. 28, 2011.

[5] R. Cox, D. V. S. Green, C. N. Luscombe, N. Malcolm, and S. D. Pickett, "QSAR workbench: automating QSAR modeling to drive compound design," *Journal of Computer-Aided Molecular Design*, vol. 27, no. 4, pp. 321–336, 2013.

[6] D. E. Clark, *Evolutionary Algorithms in Molecular Design*, John Wiley and Sons, 2008.

[7] T. Solmajer and J. Zupan, "Optimization algorithms and natural computing in drug discovery," *Drug Discovery Today*, vol. 1, no. 3, pp. 247–252, 2004.

[8] M. Forlin, I. Poli, D. De March, N. Packard, G. Gazzola, and R. Serra, "Evolutionary experiments for self-assembling amphiphilic systems," *Chemometrics and Intelligent Laboratory Systems*, vol. 90, no. 2, pp. 153–160, 2008.

[9] D. De March, M. Forlin, D. Slanzi, and I. Poli, "An evolutionary predictive approach to design high dimensional experiments," in *Proceedings of the Articial Life and Evolutionary Computation (WIVACE '08)*, R. Serra, I. Poli, and M. Villani, Eds., pp. 81–88, World Scientific, 2008.

[10] R. Baragona, F. Battaglia, and I. Poli, "Evolutionary Statistical Procedures," in *Statistics and Computing*, Springer, Berlin, Germany, 2011.

[11] D. Ferrari, M. Borrotti, and D. De March, "Response improvement in complex experiments by co-information composite likelihood optimisation," *Statistics and Computing*, pp. 1–13, 2013.

[12] M. Borrotti and I. Poli, "Nave Bayes ant colony optimisation for experimental design," in *Synergies of Soft Computing and Statistics for Intelligent Data Analysis, Advances in Intelligent Systems and Computing*, R. Kruse, M. R. Berthold, C. Moewes et al., Eds., vol. 190, pp. 489–497, Springer, 2013.

[13] L. Breiman, "Random forests," *Machine Learning*, vol. 45, no. 1, pp. 5–32, 2001.

[14] A. Verikas, A. Gelzinis, and M. Bacauskiene, "Mining data with random forests: a survey and results of new tests," *Pattern Recognition*, vol. 44, no. 2, pp. 330–349, 2011.

[15] A. L. Boulesteix, S. Janitza, J. Kruppa, and I. R. Knig, "Overview of random forest method- ology and practical guidance with emphasis on computational biology and bioinformatics," *Wiley Interdisciplinary Reviews*, vol. 2, no. 6, pp. 493–507, 2012.

[16] A. Liaw and M. Wiener, "Classification and regression by random forest," *R News*, vol. 2, no. 3, pp. 18–22, 2002.

Hindawi Publishing Corporation
Computational and Mathematical Methods in Medicine
Volume 2013, Article ID 467428, 8 pages
http://dx.doi.org/10.1155/2013/467428

Research Article

The MATCHIT Automaton: Exploiting Compartmentalization for the Synthesis of Branched Polymers

Mathias S. Weyland,[1] Harold Fellermann,[2] Maik Hadorn,[3] Daniel Sorek,[4] Doron Lancet,[4] Steen Rasmussen,[2,5] and Rudolf M. Füchslin[1,6]

[1] *European Centre for Living Technology, S. Marco 2940, 30124 Venice, Italy*
[2] *Center for Fundamental Living Technology (FLinT), Department of Physics, Chemistry and Pharmacy, University of Southern Denmark, 5230 Odense, Denmark*
[3] *Department of Chemistry and Applied Biosciences, ETH Zurich, 8093 Zurich, Switzerland*
[4] *The Lancet Lab, Department of Molecular Genetics, Weizmann Institute of Science, 76100 Rehovot, Israel*
[5] *Santa Fe Institute, Santa Fe, NM 87501, USA*
[6] *Institute of Applied Mathematics and Physics, School of Engineering, Zurich University of Applied Sciences, 8401 Winterthur, Switzerland*

Correspondence should be addressed to Mathias S. Weyland; mathias@weyland.ch

Received 31 October 2013; Accepted 8 December 2013

Academic Editor: Roberto Serra

We propose an automaton, a theoretical framework that demonstrates how to improve the yield of the synthesis of branched chemical polymer reactions. This is achieved by separating substeps of the path of synthesis into compartments. We use chemical containers (chemtainers) to carry the substances through a sequence of fixed successive compartments. We describe the automaton in mathematical terms and show how it can be configured automatically in order to synthesize a given branched polymer target. The algorithm we present finds an optimal path of synthesis in linear time. We discuss how the automaton models compartmentalized structures found in cells, such as the endoplasmic reticulum and the Golgi apparatus, and we show how this compartmentalization can be exploited for the synthesis of branched polymers such as oligosaccharides. Lastly, we show examples of artificial branched polymers and discuss how the automaton can be configured to synthesize them with maximal yield.

1. Introduction

Recently, small scale personal manufacturing has seen a rapid increase in popularity with emerging technologies such as 3D printing. In place of central production and physical distribution of goods, personal manufacturing offers a transfer of information (e.g., designs, protocols) followed by in-place, customizable production. Although mainly discussed in the context of macroscale personal manufacturing (i.e., 3D printing), personal manufacturing is also found in the domain of (bio-)chemistry. In custom oligonucleotide and peptide synthesis, the information, that is, DNA or protein sequence, is sent by the customer to the supplier. Even though the synthesized DNA oligonucleotides or peptides are shipped back to the customer (i.e., transfer of goods), this example demonstrates how transferred information can lead to in-place, customizable production of (bio)chemical goods. However, often the desired product cannot be synthesized via either one-pot synthesis or sequential one-pot synthesis. Consequently, distinct confinement and transport of substances and an elaborate temporal and spatial reaction management are needed.

The European Commission funded project MATCHIT (Matrix for Chemical IT [1, 2]) aims to open the domain of chemistry for distributed manufacturing by implementing unconventional embedded computation systems. By employing addressable soft colloid supermolecular chemical containers (chemtainers) that act both as transport and reaction vessels and that are interfaced with electronic computers via microelectromechanical systems (MEMS), the topological

organization of the cytoplasm of natural cells is mimicked, where a multitude of chemicals is organized in addressable compartments and where transport and fusion of compartments trigger reactions of previously separated chemicals. By utilizing a hybrid biochemical and information technological system, an integrated programmable material transportation, information processing and material production system was implemented resulting in a generic programmable platform for complex molecular processing tasks.

In contrast to other approaches that either employ "traditional" 3D printing techniques to implement small scale personal manufacturing in (bio)chemistry [3] or use of simpler building blocks like lipid-coated aqueous droplets in oil [4], in the MATCHIT machine, DNA oligonucleotides attached to the surface of the chemtainers (DNA addresses) are employed to guide the chemtainer's assembly, fusion promoting chemical reactions, and reversible docking on defined spots of the microfluidic environment through reversible hybridization. The DNA addresses thereby dynamically change and adapt as a result of ongoing DNA-computation operations such as relabeling and simple Boolean operations [5–7]; the current set of DNA addresses therefore both portrays the chemtainers history and defines the next steps to take (e.g., with whom to bind and fuse, where to dock). In this context, the MEMS technology is perfectly suited not only for precise and accurate guidance the chemtainers creation [8], loading, and manipulation but also for an on-chip pre- and postprocessing (e.g., electrophoretic separation) of substances released from the chemtainers or waiting for reencapsulation.

The modular design of the MATCHIT machine allowed for an individual testing and optimization of each of its components (i.e., chemtainers, MEMS, and computer science). In the context of the chemtainers, we reported the first DNA-computation operations on the surface of artificial giant unilamellar vesicles (GUVs), DNA-mediated self-assembly [9, 10] and controlled fusion [11–13] of GUVs and oil-in-water droplets, and increase in the complexity of available soft colloid chemtainers by preparing hierarchically organized GUVs [14]. The research efforts of integrating chemical and electronic systems in a MEMS device resulted in unconventional embedded computation systems that performed complex nanoscale chemical tasks autonomously [15]. Traditional computer science was not only used for programing the MEMS devices. By using the same language for simulating the inherent complexity of MATCHIT objects and operations and to program the MEMS devices, solutions found *in silico* were directly transferred to control the MEMS devices. In this context, the MATCHIT automaton (MA) is able to optimize the microfluidics design in terms of structure, MEMS and chemtainer DNA addresses, chemtainer types, and interaction rules.

Our motivation to demonstrate how the MA can be applied to the synthesis of branched polymers (e.g., branched oligosaccharides) is as follows: often oligosaccharides are attached to proteins and impart an additional level of information content to the underlying protein structures [16]. The glycosylation is a critical function of the biosynthetic-secretory pathway in the endoplasmic reticulum (ER) and the Golgi apparatus. Glycoproteins associated with cell surface and intracellular proteins have crucial biological and physiological roles, from contributions in protein folding and quality control to involvement in a large number of biological recognition events [16, 17]. In the ER, for example, glycosylation is used to monitor the status of protein folding, acting as a quality control mechanism to ensure that only proteins properly folded are trafficked to the Golgi. Oligosaccharides are composed of monosaccharides each having four to five binding sites. This large number of binding sites and the vast number of distinct monosaccharides constitute the large variety of oligosaccharides. Thus, the glycan structures attached to proteins can be highly complex, with numerous possibilities for branching and anomeric linkage. Consequently, glycoproteins have much greater structural diversity than linear nucleic or polypeptide structures. Hence, the custom synthesis of such complex branched molecules is a demanding task because the control of potential side reactions is still not solved [18]. In nature, glycosylation occurs in a stepwise fashion by trafficking glycoproteins to distinct spatially separated compartments (i.e., Golgi cisternae) that contain a distinct set of enzymes.

One approach to tackle the problem of side reactions is to use linker structures to increase the yield in one-pot reactions. Such small linker structures have been implemented and are known by the term click chemistries. The concept of click chemistries is for example, described in Kolb et al. [19–21] and addresses powerful, highly reliable, and selective reactions for the rapid synthesis of new compounds through heteroatom links. In the context of oligosaccharide synthesis however, the number of such click-chemistry linkers is highly limited, leading to a significant, but moderate, increase of yield [22]. Hence, our approach is to augment the effect of these small linker structures by means of additional compartmentalization. Specifically, the substances (e.g., oligosaccharide) are enclosed by chemtainers which can be transported between compartments and which can be addressed by tags.

In this paper, we study an artificial chemistry [23] that models the synthesis of branched polymers. The focus of this work lies in the description of a compiler for a defined reaction environment, the MA. By a compiler we understand a method that takes the description of a branched oligomer as input and maps it onto system parameters of the MA such that this automaton synthesizes the input structure. We refer to these system parameters as the configuration of the MA. With such a compiler, we present an example of what is often called ChemBio-IT [24], the merger of computer science and (bio)chemistry. The MA offers a platform with which such combinatorial variety of different types of branched oligomers—a promising tool in a future personalized medicine—can be generated. This work presents a mathematical formalism to encode a large and biologically important class of such oligomers and thereby enables automatized generation of protocols for the synthesis of specific structures.

The contribution of this work is twofold. First, we present a mathematical framework that describes the MA. Second,

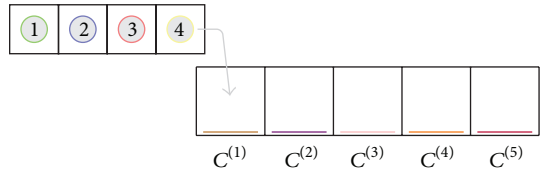

Figure 1: Overview of the elements of the MATCHIT automaton. The inlet is populated with four chemtainers, carrying the substances 1 to 4, respectively, and equipped with different chemtainer tags (color of circle). The tube consists of five cells which are equipped with individual cell tags. The color of the bar at the bottom of each cell implies which particular cell tag is used. The arrow shows how chemtainer at the front of the inlet would be inserted into the tube.

we discuss an algorithm—the compiler—to configure the MA in order to synthesize branched polymers. The remainder of this paper is structured as follows. In Section 2, we describe the MA in mathematical terms (Section 2.1), we suggest how branched polymers can be encoded into a mathematical graph structure (Section 2.2), and we describe how the MA configuration can be derived from a given target polymer (Section 2.3). In Section 3, we discuss some results obtained using these methods. We compare the MA to another artificial reactor and we propose improvements for the shortcomings of the MA. We finish this paper with a conclusion in Section 4 where we hypothesize how real instances of the MA could be used in the future.

2. Methods

2.1. Description of the MATCHIT Automaton. The MA can be seen as a model of the spatially separated compartments of the ER and Golgi that contain distinct sets of enzymes. In particular, the MA consists of the following entities. (a) *Substances.* That is, monomers, polymers or a mixture thereof. (b) *Reactions.* That is, translation rules that determine how two substances react into a third substance (cf. enzymes). (c) *Chemtainers.* That is, compartments containing a substance and equipped with one or more chemtainer tags. (d) *Cells.* That is, compartments containing chemtainers, equipped with a cell tag. (e) *Tags.* That is, a mechanism that induces chemtainers to stick to cells (chemtainer cell interaction) or to each other (chemtainer chemtainer interaction). (f) *Tube.* That is, a chain of concatenated cells. (g) *Inlet.* That is, the mechanism to stage chemtainers and insert them into the tube.

The MA operates in a discretized time domain. Figure 1 shows an overview of the MA and its entities. The general working principle is as follows. Chemtainers containing substances are staged inside an inlet and inserted into the tube consisting of various cells. The chemtainers move from cell to cell and can fuse under some conditions controlled by a tag system. In the event of a chemtainer fusion, the substances carried inside the fused chemtainers mix and can react with each other. The product of such a reaction remains inside the chemtainer, but this chemtainer can fuse with other chemtainers in subsequent steps. As we will demonstrate, this allows for a very granular control of the sequence of reaction steps contained inside the chemtainers. The following sections describe the various aspects of the system in more detail.

2.1.1. Inlet, Tube, and Cells. The tube is a list of m cells $C^{(1)}, \ldots, C^{(m)}$. The movement of chemtainers from cell to cell is governed by the following rules. (a) Chemtainers from the inlet are always inserted into $C^{(1)}$. (b) Chemtainers can only move from $C^{(j)}$ to $C^{(j+1)}$. (c) Chemtainers in $C^{(m)}$ remain there (end of the tube).

The inlet is a list of chemtainers; its purpose is to insert chemtainers into the tube. There is only one inlet and it is inserting chemtainers into the first cell of the tube, that is, $C^{(1)}$.

2.1.2. Chemtainer. A chemtainer c_i is a tuple (s_i, T_i, μ_i) where $s_i \in S$ is a substance and $T_i \subset T^{\text{Chem}}$ is a set of tags assigned to the chemtainer. Each chemtainer maintains a counter μ_i which tells how many time steps are left for the chemtainer to stick to the current cell before moving to the next cell. This allows for colocation and subsequent fusion of chemtainers.

2.1.3. Substance and Reaction. Exactly two substances can react with each other; the result of a reaction is a product substance. The notation for such a reaction is $(s_i + s_j \rightarrow s_p)$ where s_i and s_j react to the product s_p. Note that a reaction exists for any pair s_i and s_j; if the reactants cannot react chemically, the resulting product is a mixture of s_i and s_j which is considered to be waste. S denotes the set of all substances and $S' \subset S$ is the set of all monomers.

2.1.4. Tag and Affinity. Tags are used to determine whether chemtainers can interact with each other and whether they can stick to cells. There are two kinds of tags: chemtainer-tags $t^{\text{Chem}} \in T^{\text{Chem}}$ and cell tags $t^{\text{Cell}} \in T^{\text{Cell}}$. The former are a property of chemtainers; the latter are a property of cells.

For $T = T^{\text{Chem}} \cup T^{\text{Cell}}$ there is an affinity function $a : T \times T \rightarrow \mathbb{N}_0$ which assigns a nonnegative integer to each combination of tags t_i and t_j such that $a(t_i, t_j) = a(t_j, t_i)$. This affinity a between two tags is interpreted as follows. (a) If $t_i \in T^{\text{Chem}}$ and $t_j \in T^{\text{Cell}}$, a indicates the total number of time steps the chemtainer takes to stick to the cell. $a = 0$ means that the chemtainer does not stick to the cell at all. (b) If $t_i, t_j \in T^{\text{Chem}}$, $a > 0$ indicates that two chemtainers can potentially fuse, and $a = 0$ indicates that two chemtainers cannot fuse. (c) If $t_i, t_j \in T^{\text{Cell}}$, a has no meaning since the cells are static

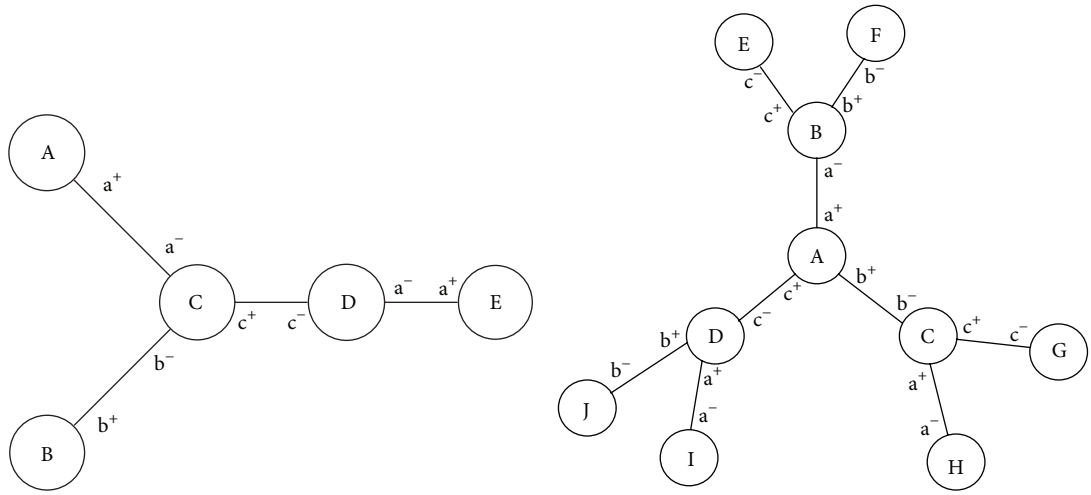

(a) Pentamer (b) Decamer

Figure 2: Examples of target polymers. Monomers are denoted by capital letters, and linkers associated with the bonds between monomers are denoted by lowercase letters and a sign; linkers with the same letter and opposite signs are matching linkers.

and cell tags never interact with each other. Hence this affinity is not defined.

2.1.5. Dynamics. The time domain is discretized into time steps $\tau \in \mathbb{N}_0$. At time step $\tau = 0$, the inlet is filled with n chemtainers and no chemtainer has moved or reacted yet.

Starting from time step $\tau = 1$ onwards, the following steps are executed in the order stated. (a) Move chemtainers from one cell to the next: the counter μ_i of each chemtainer c_i is decreased by 1. If $\mu_i = 0$ before decreasing, c_i is moved to the next cell. The chemtainer counter μ_i is reset according to the largest chemtainer cell affinity; that is,

$$\mu_i = \max_{t_j} \left(a\left(t_j, t_c\right)\right) \tag{1}$$

over all the chemtainer tags t_j of chemtainer c_i; t_c is the chemtainer tag of the next cell. (b) Move one chemtainer from the front of the inlet to the first cell in the tube $C^{(1)}$. (c) Chemtainer fusion and reactions: for all chemtainers that are both sticking to the same cell j (i.e., with $\mu_i > 0$) and sticking together by the means of chemtainer chemtainer interaction, fuse the two chemtainers to a single one and apply the appropriate reaction to the chemtainer contents. Note that a cell may potentially contain more than two chemtainers, in which case the order of fusion has to be defined. The algorithm described below (see Section 2.3.3) however ensures that such a situation never occurs; hence we do not define the order of fusion for such a case.

After the consecutive execution of these three steps, τ is incremented by 1.

2.2. Representation of Chemtainer Content and Fusion Thereof. A graph structure is used to represent substances. The vertices of the graph represent monomers. Each vertex is associated with a label that is an element of S' (i.e., the vertex color) denoting a specific type of monomer. Edges between vertices represent bonds between monomers. In addition to these properties of a colored graph, each vertex contains a tuple of linkers. Edges are associated with these linkers such that the degree of a vertex cannot be greater than its number of linkers. If the degree of the vertex is less than the number of linkers, some linkers are considered to be active, allowing for a reaction.

The ordered nature of the linker tuple allows for a limited preservation of the geometric arrangement of the substance. Two substances are considered equal if and only if their graph representation is isomorphic (i.e., the structure of the substances is equal) and their linker tuples match.

In the event of a chemtainer fusion, the chemtainer resulting from the fusion inherits both sets of chemtainer tags from the original chemtainers. The following cases are to be distinguished when generating the graph of a product substance. (a) The active linkers of both substances do not match. (b) The active linkers of both substances match unambiguously. (c) The active linkers of both substances match ambiguously, such that different product substances may result depending on chance.

In case (a), the resulting substance is the graph union of both reactant substances. An example for this case is the reaction of the polymers shown in Figures 2(a) and 2(b). Both these reactants do not have any matching linkers. In fact, they do not have open linkers at all. In case (b), an edge is introduced between the two matching linkers in the graph union. For example, consider the polymer shown in Figure 2(a) and remove the edge between D and E. The resulting two reactants each have one exposed linker, a− and a+, respectively. A reaction of these two reactants thus leads to the original polymer. Note that there is no ambiguity; the only site the linker a− can bind to is the exposed linker a+. Case (c) however might be a source of waste because the substances may react to a product undesired for the synthesis.

```
(1) build_reaction_tree()begin
(2)     g ← target polymer
(3)     n ← root node
(4)     recursion(g, n)
(5)     return n
(6) recursion(graph g, node n)begin
(7)     for each edge e of g do
(8)         (v1, v2) ← vertices of e
(9)         (g1, g2) ← split(g, e)
(10)        P ← estimate_probability(g1, g2, e)
(11)        r ← add_child(n, P)
(12)        s_v1 ← add_child(r, v1)
(13)        s_v2 ← add_child(r, v2)
(14)        recursion(g1, s_v1)
(15)        recursion(g2, s_v2)
```

Algorithm 1: Algorithm to recursively find possible paths of synthesis for a target polymer.

For example, consider the larger of the two reactants in the previous example, that is, the one consisting of the monomers A, B, C, and D (but not E). Following the same procedure and removing the edge between A and C result in two reactants that can form different products. Particularly The monomer A can bind not only to C but also to D. Since our goal is to maximize yield (i.e., to minimize waste), the algorithm presented in Section 2.3.3 ensures that case (c) is not encountered.

2.3. Compiling a Suitable MA for a Given Target Polymer. In this section, we present the steps that are required to find a suitable MA configuration (i.e., cells, tags, and affinities) to synthesize a given target polymer starting from its monomers. The goal is to only allow for steps that have unambiguously matching linkers and to ensure that chemtainer fusion is only possible for pairs of chemtainers in each cell, thus avoiding any waste. Note that we first need to identify the proper sequential chemical pathway at which point we can implement this pathway by configuring the MA appropriately.

Thus, this is a two-step process. First, the possible paths of synthesis are identified. Second, one of these paths is chosen and the MA configuration is derived. Due to the huge number of synthesis paths, the first step is time consuming and requires a lot of storage space. We show at the end of this section that a suitable path of synthesis can be found without enumerating all possible options.

2.3.1. Identifying Paths of Synthesis. Algorithm 1 generates possible paths of synthesis in a recursive top-down approach. The result is a tree of *reaction nodes* and *edge-split nodes*. Reaction nodes are used to estimate the quality of a particular reaction, and edge-split nodes are used to track the edge that is to be connected during the synthesis.

First, a root node is created and the recursion is started with the assembled target polymer as input graph (lines 2–4). One edge $e = (v_1, v_2)$ is removed from this input graph (lines 8–9), resulting in two disconnected subgraphs g_1 and g_2 representing two intermediate products. In general, there is no guarantee that the removal of an edge will disconnect the graph; for example, removing the first edge from a cyclic structure will lead to an acyclic, connected graph. In the case of branched polymers however, disconnected sub-graphs can be assumed by definition. The probability p for a successful synthesis of the target polymer given the two sub-graphs is computed (line 10). A new reaction node is added as child of the current node in the tree and labelled with p. Furthermore, two edge-split nodes are added to the newly inserted reaction node and labelled with v_1 and v_2, respectively (lines 11–13).

The same procedure is repeated recursively with each of the sub-graphs until no more edges can be removed, meaning that the polymer was decomposed to one of its monomers. On each level of the recursion, every edge of the respective input graph is removed as described above.

The runtime of this brute force algorithm scales factorial with the size of the target structure, which is worse than exponential. The runtime could be improved by dynamic programming techniques, where results of the recursion for sub-graphs are memorized in order to avoid multiple computations for the same structure. We have not taken this route, however, as we will introduce an additional constraint in the next section that will prune the search space such that the algorithm performs in linear time.

2.3.2. Selecting Suitable Path of Synthesis. A suitable path can be selected by walking the tree resulting from the algorithm in a manner that never adds a node with $p < 1$ to the fringe. This approach fails if no solution with 100% yield exists. In the case of branched polymers however, this case can be ruled out if the number of distinct linker pairs is at least as large as the degree of any vertex. This allows us to impose the constraint that the linkers associated with each vertex shall be unique. Under this constraint, we prove our claim as follows.

Let us start with the graph of the target polymer, P_0, and remove an arbitrary edge. This leads to two disconnected sub-graphs P_1 and P_2, each of which has one active linker. Because there is only one active linker per subgraph, mixing the substances represented by the two sub-graphs would

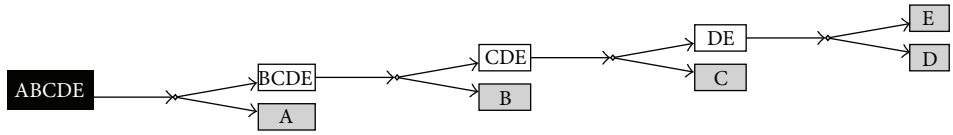

Figure 3: Example of a path of synthesis by sequential insertion for the target polymer shown in Figure 2(a). Edge-split nodes are drawn as rectangles and reaction nodes as small diamonds. The black rectangle denotes the target polymer, white rectangles denote intermediate products, and gray rectangles are monomers. The nodes are added to the tree from left to right as the algorithm progresses. Because the algorithm starts at the target polymer, decomposing it into its monomers, the tree shows the reverse of a synthesis.

result in the unambiguous synthesis of the target polymer. Without loss of generality, let us now continue with the first of the two sub-graphs, P_1, and remove an edge from the vertex with the active linker. This decomposition leads to two sub-graphs P_3 and P_4. As before, P_1 can be synthesized by mixing P_3 and P_4 because the newly exposed active linkers are different from the previously exposed ones due to the constraint. Moreover, we can ensure that neither P_3 nor P_4 can react with P_1 by isolating subreactions in different chemtainers. In general, the repeated application of this procedure eventually leads to a monomer which cannot be decomposed any further. Because the constraint ensures that each decomposition can be uniquely synthesized by mixing the substances represented by the resulting sub-graphs, $p = 1$ is guaranteed for each step.

2.3.3. Configuration of the MA. Once a suitable path of synthesis is chosen, the MA is configured. A suitable configuration results in the synthesis of the target polymer from monomers and can be found as follows. First, the reaction nodes of the selected path are visited in a breadth-first manner. This means that the tree is visited level by level, starting from the target polymer at the root, visiting the reactions of the intermediate products. For each node that is visited, a cell is created. Because the root represents the last step of the synthesis, the first node that is visited corresponds to the last cell of the tube and the last node that is visited corresponds to the first cell of the tube. The m cells created in that manner are equipped with a unique cell tag.

Second, all monomers of the target polymer are filled into chemtainers. If the molecular graph corresponding to the target polymer consists of n nodes, n chemtainers are created, each containing the respective monomer. Note that two chemtainers are created if two nodes with a particular color are present. The n chemtainers created in this manner are equipped with a unique chemtainer tag.

Third, the affinities are defined. As a consequence of the breadth-first traversal, the first cell corresponds to a reaction node that has two external children. These two children correspond to two chemtainers c_i and c_j containing monomers, which are to be staged inside the inlet. Hence, a positive affinity $a(t_i, t_j) > 0$ is defined for the interaction between the two tags of the chemtainers c_i and c_j. Furthermore, c_i and c_j shall stick to the first cell, and therefore an affinity a for the interaction between the cell tag of cell 1 and the tag of chemtainer c_i is defined. The same affinity is also defined for the interaction between the cell tag and the tag of c_j, such that (a) both chemtainers stick together and (b) both chemtainers stick to cell 1, thus satisfying the requirements for the fusion of c_i and c_j in the first cell. The selection of a suitable value for a is discussed below.

In general, a cell is responsible for either (a) the fusion of chemtainers containing a monomer each, (b) the fusion of a chemtainer containing a monomer with a chemtainer containing an intermediate product, or (c) two chemtainers containing intermediate products each. If a chemtainer contains a monomer, its tag is known because it was assigned while staging the inlet and can therefore readily be used as discussed above. If a chemtainer contains an intermediate product, it is the result of a chemtainer fusion since all original chemtainers were containing monomers. As a consequence, such a chemtainer will carry each of the tags of the fused original chemtainers and a tag can be found by a lookup in the subtree of the corresponding reaction node.

The following considerations are made to compute the affinity of chemtainer-cell interaction a. If a is too small, the counter μ_i of a chemtainer waiting for fusion with another chemtainer may elapse before the other chemtainer reaches the cell. Therefore, the rule

$$a_i = n + \sum_{j=1}^{i-1} a_j \tag{2}$$

is suggested for any affinity a_i involving the cell tag of the ith cell. The rule takes into account the release of the n chemtainers from the inlet, as well as the maximal time a chemtainer could spend sticking in previous cells.

To summarize, the procedure described above ensures that (a) there is a bijection between reaction nodes and cells, (b) the reactions occur in the proper order, (c) the proper conditions with respect to tag affinity are created for successful chemtainer fusion and subsequent reaction of chemtainer content, and (d) chemtainer fusion does not occur in the absence of a planned reaction.

3. Results and Discussion

The strategy to find all paths of synthesis(recall Algorithm 1) and to configure the MA was implemented and a simulator for the MA was developed. A path of synthesis for the target polymer in Figure 2(a), as computed by Algorithm 1, is displayed in Figure 3. Note that any path of synthesis is a

tree by itself. The one shown in the figure is equivalent to a synthesis by sequential insertion because at least one of the two children of each reaction node is a monomer. Although not investigated further in this paper, it did not escape our attention that such a "bushy" path of synthesis would allow the synthesis of several intermediate products in parallel, leading to faster completion of the target polymer.

We also applied our algorithm to the decamer in Figure 2(b) in which case no path of synthesis by sequential insertion without loss (i.e., $p < 1$) was found. This was expected because the polymer was carefully designed to demonstrate that some polymers cannot be synthesized if the number of available linkers is restricted. However the polymer satisfies the constraint of distinct linkers per monomer, and hence our algorithm was able to derive a path of synthesis that does not result in any waste and was also able to compute a configuration of the MA that led to the successful synthesis in simulation.

Our work shows the advantages of compartmentalization for the synthesis of branched polymers. If the number of linkers is limited, we can suppress unwanted reactions by spatially separating the substances. A disadvantage of our method is that Algorithm 1 is computationally heavy and requires a lot of memory as it lays out the whole tree of all possible paths of synthesis. This allows us to find the path which leads to maximal yield by multiplying the probabilities p as we traverse the tree, but in the case of branched polymers we know that there exists a path for which $p = 1$ holds at every step as long as the constraint of distinct linkers per vertex is met. Hence, building the full tree is not necessary. Instead, we can simply remove an arbitrary edge from the target polymer and continue to remove edges from the same vertices as discussed in Section 2.3.2. This leads to a path of synthesis with maximal yield in linear time.

The representation of substances based on a graph entails some limitations. First, the substances are assumed to be planar. Second, this representation fails to address the selective synthesis of stereoisomers and similar structures. We note however that the substances could be represented in any way as long as products can be split into reactants, and the probability of a successful synthesis of the product out of these reactants can be estimated. This includes extensions of the graph structure used in this paper as well as even physical simulations.

The MA is modeled as a deterministic device. An according stochastic structure has been studied by B. Reller and presented in [22]. Reller proposed, also *in silico*, a self-assembling microreactor, a two-dimensional structure composed of chemtainers that mediate different linking reactions. This microreactor constitutes a spatially heterogeneous reaction environment which, by its spatial structure, controls or at least amplifies desired reaction pathways. In contrast to the MA, no compiler could be given for Reller's approach.

4. Conclusion

In this paper, we have presented a mathematical framework to optimize chemical reactions of branched polymers at high yields by means of compartmentalization. It is emphasized that today no complete implementation of an MA exists. However, MATCHIT delivered important technologies towards an MA. As already mentioned in Section 1 (see references given there), candidates for chemtainers investigated in MATCHIT are vesicles and oil droplets (in water) for which a range of functionalities relevant to the implementation of an MA have been demonstrated. Together with novel types of MEMS devices also resulting from MATCHIT [15], a physical implementation of an MA may be within reach in the near future.

Why may one be interested in the construction of such a system instead of using a series of test tubes in a lab? Besides aspects of automation, there is another, fundamental rationale for investigating designs with the potential for miniaturization [22]. We hypothesize that miniaturized version of the MATCHIT automaton could provide opportunities to use types of catalysts not used in conventional chemical process management. Assume that one synthesizes oligomers with some sort of catalytic activity, catalytic activity that is used in a subsequent step. It may well be the case that the environment in which this catalyst is synthesized (or activated) is different from the environment in which the catalyst has to act. In a macroscopic laboratory, this implies that the catalyst has to be transferred from one environment to the other, a process that takes time. This means that catalysts have to fulfill two requirements: first, they have to be efficient, and, second, they have to be stable. On a microscopic length scale, where transport involves transport over micrometers, ten seconds is quite a time (even if this transport happens by diffusion). This means that in microscopic reactors, catalysts, if they are produced *in situ*, only have to be efficient but no longer need to be particularly stable. An average life time of minutes to fractions of a second is sufficient for typical lengths ranging from several ten μm down to part of μm, depending on passive diffusion and active processes such as electrical fields [15]. As a result, many more molecules qualify as potential catalysts. The possibility that microreactors could enable the use of metastable catalysts in a technically feasible manner is a more than sufficient justification for the study of such systems.

Conflict of Interests

The authors declare that there is no conflict of interests regarding the publication of this paper.

Acknowledgments

The research leading to these results has received funding from the European Community's Seventh Framework Programme (FP7/2007–2013) under Grant Agreement no. 249032 (project acronym: MATCHIT), the Danish National Research Foundation, and the University of Southern Denmark through the Center for Fundamental Living Technology (FLinT). M. Hadorn was supported by the Swiss National Science Foundation (SNSF).

References

[1] MATCHIT Matrix for Chemical IT, http://fp7-matchit.eu.

[2] M. Amos, P. Dittrich, J. McCaskill, and S. Rasmussen, "Biological and chemical information technologies," in *Proceedings of the 2nd European Future Technologies Conference and Exhibition (FET '11)*, vol. 7, pp. 56–60, May 2011.

[3] M. D. Symes, P. J. Kitson, J. Yan et al., "Integrated 3D-printed reactionware for chemical synthesis and analysis," *Nature Chemistry*, vol. 4, no. 5, pp. 349–354, 2012.

[4] G. Villar, A. D. Graham, and H. Bayley, "A tissue-like printed material," *Science*, vol. 340, no. 6128, pp. 48–52, 2013.

[5] G. Seelig, D. Soloveichik, D. Y. Zhang, and E. Winfree, "Enzyme-free nucleic acid logic circuits," *Science*, vol. 314, no. 5805, pp. 1585–1588, 2006.

[6] D. Y. Zhang and E. Winfree, "Control of DNA strand displacement kinetics using toehold exchange," *Journal of the American Chemical Society*, vol. 131, no. 47, pp. 17303–17314, 2009.

[7] L. Qian and E. Winfree, "Scaling up digital circuit computation with DNA strand displacement cascades," *Science*, vol. 332, no. 6034, pp. 1196–1201, 2011.

[8] D. van Swaay and A. deMello, "Microuidic methods for forming liposomes," *Lab on a Chip*, vol. 13, no. 5, pp. 752–767, 2013.

[9] M. Hadorn and P. Eggenberger Hotz, "DNA-mediated self-assembly of artificial vesicles," *PloS ONE*, vol. 5, no. 3, article e9886, 2010.

[10] M. Hadorn, E. Boenzli, K. T. Sffrensen, H. Fellermann, P. E. Hotz, and M. M. Hanczyc, "Speciffc and reversible DNA directed self-assembly of oil-in-water emulsion droplets," *Proceedings of the National Academy of Sciences*, vol. 109, no. 50, pp. 20320–20325, 2012.

[11] F. Caschera, S. Rasmussen, and M. M. Hanczyc, "An oil droplet division-fusion cycle," *ChemPlusChem*, vol. 78, no. 1, pp. 52–54, 2013.

[12] T. Sunami, F. Caschera, Y. Morita et al., "Detection of association and fusion of giant vesicles using a fluorescence-activated cell sorter," *Langmuir*, vol. 26, no. 19, pp. 15098–15103, 2010.

[13] F. Caschera, T. Sunami, T. Matsuura, H. Suzuki, M. M. Hanczyc, and T. Yomo, "Programmed vesicle fusion triggers gene expression," *Langmuir*, vol. 27, no. 21, pp. 13082–13090, 2011.

[14] M. Hadorn, E. Boenzli, P. E. Hotz, and M. M. Hanczyc, "Hierarchical unilamellar vesicles of controlled compositional heterogeneity," *PloS One*, vol. 7, no. 11, article e50156, 2012.

[15] P. F. Wagler, U. Tangen, T. Maeke, and J. S. McCaskill, "Field programmable chemistry: integrated chemical and electronic processing of informational molecules towards electronic chemical cells," *BioSystems*, vol. 109, no. 1, pp. 2–17, 2012.

[16] R. D. Cummings, "The repertoire of glycan determinants in the human glycome," *Molecular BioSystems*, vol. 5, no. 10, pp. 1087–1104, 2009.

[17] A. Varki, "Biological roles of oligosaccharides: all of the theories are correct," *Glycobiology*, vol. 3, no. 2, pp. 97–130, 1993.

[18] K. M. Koeller and C.-H. Wong, "Complex carbohydrate synthesis tools for glycobiologists: enzyme-based approach and programmable one-pot strategies," *Glycobiology*, vol. 10, no. 11, pp. 1157–1169, 2000.

[19] H. C. Kolb, M. G. Finn, and K. B. Sharpless, "Click chemistry: diverse chemical function from a few good reactions," *Angewandte Chemie—International Edition*, vol. 40, no. 11, pp. 2004–2021, 2001.

[20] H. C. Kolb and K. B. Sharpless, "The growing impact of click chemistry on drug discovery," *Drug Discovery Today*, vol. 8, no. 24, pp. 1128–1137, 2003.

[21] M. D. Best, "Click chemistry and bioorthogonal reactions: unprecedented selectivity in the labeling of biological molecules," *Biochemistry*, vol. 48, no. 28, pp. 6571–6584, 2009.

[22] R. M. Füchslin, A. Dzyakanchuk, D. Flumini et al., "Morphological computation and morphological control: steps toward a formal theory and applications," *Artiffcial Life*, vol. 19, no. 1, pp. 9–34, 2013.

[23] P. Dittrich, J. Ziegler, and W. Banzhaf, "Artificial chemistries—a review," *Artificial Life*, vol. 7, no. 3, pp. 225–275, 2001.

[24] COBRA Project: EU FP7 project, http://www.cobra-project.eu.

Hindawi Publishing Corporation
Computational and Mathematical Methods in Medicine
Volume 2013, Article ID 634168, 7 pages
http://dx.doi.org/10.1155/2013/634168

Research Article

Generic Properties of Curvature Sensing through Vision and Touch

Birgitta Dresp-Langley

UMR 7357 CNRS, Icube-Unistra, Université de Strasbourg, 67000 Strasbourg, France

Correspondence should be addressed to Birgitta Dresp-Langley; birgitta.dresp-langley@univ-montp2.fr

Received 23 August 2013; Accepted 29 November 2013

Academic Editor: Rudolf Füchslin

Generic properties of curvature representations formed on the basis of vision and touch were examined as a function of mathematical properties of curved objects. Virtual representations of the curves were shown on a computer screen for visual scaling by sighted observers (experiment 1). Their physical counterparts were placed in the two hands of blindfolded and congenitally blind observers for tactile scaling. The psychophysical data show that curvature representations in congenitally blind individuals, who never had any visual experience, and in sighted observers, who rely on vision most of the time, are statistically linked to the same mathematical properties of the curves. The perceived magnitude of object curvature, sensed through either vision or touch, is related by a mathematical power law, with similar exponents for the two sensory modalities, to the aspect ratio of the curves, a scale invariant geometric property. This finding supports biologically motivated models of sensory integration suggesting a universal power law for the adaptive brain control and balance of motor responses to environmental stimuli from any sensory modality.

1. Introduction

Interaction of the human body with technological devices relies on the multisensory integration of visual and tactile signals by the human brain, as in the use of global positioning systems for navigation, or the encoding of visual and tactile spatial information for laparoscopic surgery, for example. Experimental studies have shown that the manipulation of visual objects with the two hands and the visual and tactile integration of shape information play an important role in action planning as well as motor control [1, 2]. This is particularly important in spatial perception by the blind who never had visual experience (congenitally blind people) but who are nonetheless perfectly capable of understanding the physical environments which surround them and of forming exact representations of complex spatial geometry. Visual and tactile representations of space are thus likely to share common generic properties. Understanding how the blind compensate through touch for lack of visual data is relevant in rehabilitation research and for the effective design of technological aids designed to help the blind explore real-world spaces [3]. Moreover, knowing how visual and tactile sensing is interactively programmed in the human brain has implications for medical robotics and clinical neurology as, for example, the study and treatment of neurological disorders such as spatial neglect [4, 5] or tactile allodynia [6]. Physical and perceptual models, tested in the light of statistical probabilities, are needed to extend our knowledge on how visual and tactile brain representations function, how they interact, and what they have in common.

The unified brain processing of signals mediated by vision and touch involves cortical neurons with nonclassic receptive field structures, functionally identified in the monkey brain [7–11]. The receptive fields of such multimodal neurons correspond to action spaces that are consistent with the early theories of active perception proposed by Gibson [12, 13], who was among the first to suggest that visual and tactile representations may share common generic properties. The sensorial pathways for visual and tactile processing are independent at early stages of encoding. At later stages, a coupling of signals must take place in the brain to enable sensory coordination. This inevitably involves feedback signals from motor responses. It is likely that power laws, known to govern the integration of chemosensory signals in modality specific

pathways, reflect the generic mechanism that enables the invariant control and balance of brain activities related to the processing of signals from different sensory pathways. Yet, model hypotheses backed by consistent psychophysical data are still lacking. In this study, we looked for generic properties of spatial representations formed on the basis of vision and touch related to the mathematical properties of curved objects, represented on a computer screen for visual exploration, and their physical counterparts placed in the two hands of blindfolded and congenitally blind observers for tactile exploration.

Curvature is a mathematical property of the physical world that is of considerable importance in complex system science. Curvature guides physical, chemical, and biological processes, like protein folding, membrane binding, and other biophysical transformations [14]. The representation and cognition of curvature starts at the biochemical level of living organisms capable of sensing this property in their near or distant physical environments [15]. Curvature is also a perceptual property extracted from physical stimuli to form veridical representations in highly developed organisms such as the brain. The ability of processing curvature visually is highly developed in humans. The spatial precision with which man can distinguish a curve from a straight line reflects only a fifth of the physical spacing between two neighboring visual receptors and a tenth of the smallest receptive field centre of ganglion cells found in the primate retina [16, 17]. Among the geometric properties of curves exploited by the brain to achieve such an astonishing performance are the distance between the line or chord that joins the two ends of a curve and the parallel line tangent to that curve, the sagitta [18], and the ratio between the sagitta and the length of the chord, also called aspect ratio [19]. Visual images of curves with the same aspect ratio but varying sagitta produce identical detection thresholds, suggesting that the visual processing of curves may well be independent of scale. The aspect ratio of a curve is a scale-invariant parameter which conveys a global representation of the spatial extent or area covered by the curve, while the sagitta provides a strictly local cue to the point of maximum curvature. A mathematical model for planar curve generation based on vertically and horizontally oriented ellipses was found to produce the most reliable psychometric functions for visually mediated estimates of curvature as a function of the aspect ratio of a large number of planar curves, presented in random order on a computer screen to human observers [20]. The stimuli used in these visual experiments were designed to reflect properties of real-world objects that can be manipulated with the hands.

The most parsimonious mathematical definition of curvature relates to circles and ellipses. In terms of geometry, curves derived from circles and ellipses share certain properties, with the circle being a particular case of the ellipse. Also, the choice of elliptic curves for studying perceptual mechanisms is biologically motivated given their symmetry and the observation that, in the real world, the curvature of the contours of natural objects corresponds to a wide range of symmetrical shapes with the Euclidean properties of ellipses. For the purpose of this study, we used projective geometry to generate curves from ellipses, by affinity with concentric circles (Figure 1), as will be explained in the next section.

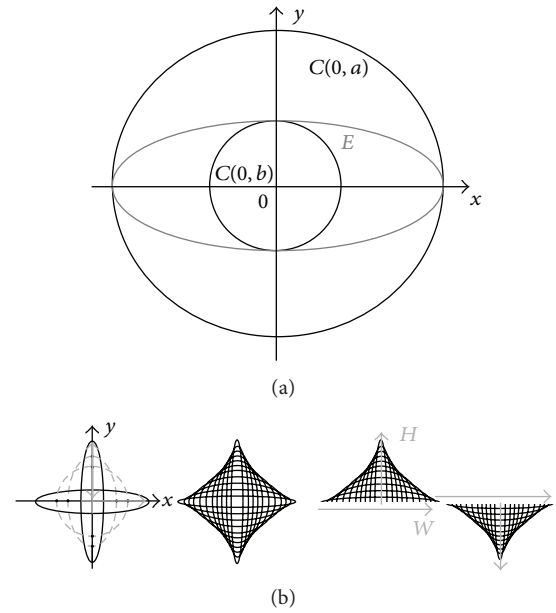

Figure 1: Ellipses were generated in AUTOCAD following the principle of planar projection of ellipses by affinity with concentric circles (a). The major and minor axes of symmetry of an ellipse E determine sagitta, or maximum height (H), and chordlength, or width (W), of the curved contour of half that ellipse. For this study, the ellipses were cut in half at an axis of symmetry (b) to generate curve stimuli with varying orientation (upward and downward), height (H), and width (W).

2. Material and Methods

Virtual curves and their real-world counterparts were presented to human observers for psychophysical scaling in two separate experiments. One experiment consisted of a randomly presented sequence of virtual curves presented as visual stimuli on a computer screen (Figure 2) to observers with normal vision. In the other experiment, the real-world counterparts of these curves (Figure 3) were presented manually, in random order and according to the same procedure, to blindfolded and congenitally blind observers. In both tasks, observers had to rate the perceived magnitude of each stimulus on a standard psychophysical scale [21, 22] with values ranging from 0 for no curvature perceived to 10 for maximum curvature perceived. This classic psychophysical scaling procedure has proven a reliable tool for studying perceptual sensations and their internal representation. Psychophysical scaling aims at linking psychological and physiological mechanisms to the physical or mathematical properties of the outside world and was introduced at the beginning of the last century by eminent medical scientists such as Fechner and Wundt. The method is now widely applied in contemporary medical research and clinical testing.

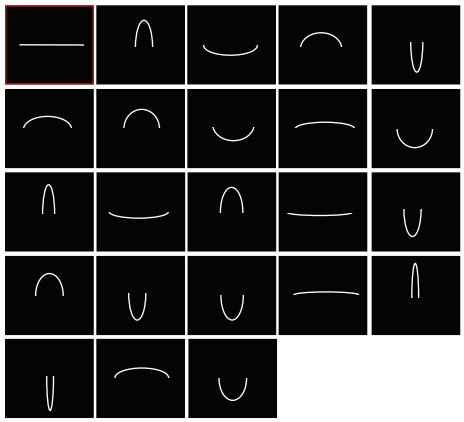

Figure 2: Computer generated (AUTOCAD) curve stimuli for the visual experiment, presented in random order on a computer screen. Curve orientation (upward or downward) varied randomly. All curves were presented at high contrast.

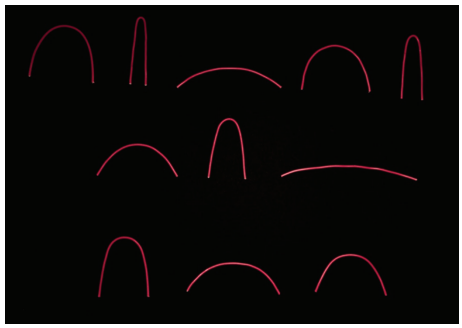

Figure 3: A photograph of the veridical real-world counterparts of the virtual curves, with identical H and W (in centimetres), used in the tactile experiment. As in the visual experiment, curves were presented in random order and curve orientation (curve placed into the two hands of an observer with upward and downward orientation) also varied randomly. Only upward orientation is shown here in this photograph.

2.1. Mathematical Properties of the Curves. The curves for this study were derived from planar ellipses, generated in AUTOCAD on the basis of projective geometry, through transformation by affinity with concentric circles (Figure 1(a)), a procedure frequently used in digital rendering and design. To understand how ellipses are obtained in such a way, it is useful to recall some of the properties of concentric circles, which share the same centre. In the Cartesian plane, the principal circle with centre 0 ($C_{0,a}$) is defined in terms of

$$R^2\left(C_{0,a}\right) = (x)^2 + (y)^2, \tag{1}$$

where R is the radius of the circle and x and y the two-dimensional spatial coordinates of the points falling on its perimeter. The second, concentric circle is obtained from the first one by

$$R^2\left(C_{0,b}\right) = (x + \delta x)^2 + (y + \delta y)^2 \tag{2}$$

or

$$R^2\left(C_{0,b}\right) = (x - \delta x)^2 + (y - \delta y)^2. \tag{3}$$

Table 1: Mathematical parameters of the eleven curves (stimuli) in terms of width (W), sagitta (H), expressed in centimetres, and the scale-invariant aspect ratio (H/W), as defined here in the introduction. Parameters of virtual curves presented on a computer screen to one group (visual experiment) and their real-world counterparts used for tactile sensing by another group of blindfolded or congenitally blind observers (tactile experiment) were the same.

W	H	H/W
2 cm	9 cm	4.50
3 cm	8.5 cm	2.83
4.5 cm	8 cm	1.77
6.5 cm	7.5 cm	1.15
8 cm	7 cm	0.87
8.5 cm	6 cm	0.70
9 cm	5 cm	0.50
10 cm	4 cm	0.40
12 cm	3 cm	0.25
14 cm	2 cm	0.14
18 cm	1 cm	0.05

Ellipses as projected images of concentric circles (Figure 1(a)) may be defined in terms of

$$(x, y) = (bx, ay) \tag{4}$$

of the principal circle $C(0, a)$ and

$$(x, y) = \left(\left(\frac{a}{b}\right)x, y\right) \tag{5}$$

of the secondary circle $C(0, b)$. This transform is sometimes referred to as a particular case of Newton's transform [23]. In the Cartesian plane, the ellipse (E) is defined in terms of

$$E = \frac{x^2}{a^2} + \frac{y^2}{b^2} = 1, \tag{6}$$

with axes a and b being the axes of symmetry intersecting at its center (Figure 1(a)). The larger axis of the two (a) is referred to as the major and the smaller (b) as the minor. The majors and the minors are directly linked to the sagitta, or maximum height (H), and the chordlength, or width (W), of the curves that were derived from the ellipses here (Figure 1(b)), which were cut in half at one of the axes of symmetry to generate curves with varying orientation in the plane (upward or downward), varying height (H), and varying width (W). The numerical values (in centimetres) of these curve parameters are given in Table 1.

2.2. Virtual Curves for Visual Presentation. Curves for visual presentation (Figure 2) generated in AUTOCAD by a group of first-year design students were stored as individual images in an image library for the experiment, which was run on an IBM Pentium III equipped with a standard colour screen. The size of a single pixel on the screen corresponded to 0.0025 cm. The physical curve parameters of maximum height (H) and width (W), given in centimetres here in Table 1, translate

into degrees of visual angle (Deg V), which reflects the size of a given parameter as it is perceived by the human eye as a function of the distance of the observer from the object viewed, using the linear transform,

$$\text{Deg}\, V = 2 \arctan\left(\frac{S}{2D}\right), \tag{7}$$

where S is the physical stimulus parameter (in centimetres) and D the viewing distance (also in centimetres) or distance of the observer's head from the screen, held constant at 120 centimetres in this experiment. All stimuli were presented foveally, bearing in mind that the diameter of foveal vision is limited to approximately 5 degrees of visual angle.

2.3. Real-World Curves for Tactile Exploration. The real-world counterparts of the curves for the tactile experiments were designed by the same group of design students. Ellipses with the same height and width properties as those generated in AUTOCAD to build a visual library of curve images presented for presentation on a computer screen were drawn on cardboard with compass and ruler following a method for drawing ellipses manually (the "gardener's ellipse method," described on http://www.mathopenref.com/). The curves, made of flexible plastic-coated wire cable (Figure 3), were bent by hand and matched visually to the images of the half ellipses. The cable material was flexible but rigid enough for a given curve once formed to retain its shape reliably under gentle manipulation with the fingers of the two hands.

2.4. Participants. Six men and four women, between 25 and 32 years old and equipped with normal vision, participated in the visual experiment. Five women and three men, between 26 and 48 years old and equipped with normal vision but blindfolded for the purpose of the experiment, and two congenitally blind observers, both men, participated in the tactile experiment. Each of the individuals only participated in one of the two experiments, which were conducted in accordance with the Declaration of Helsinki (1964). None of the participants was aware of the aims of the study.

2.5. Procedure. Eleven curves with positive curvature (upward orientation) and eleven curves with negative curvature (downward orientation) in the two-dimensional plane were presented on a computer screen in the visual experiment. The stimuli were presented in random order in 22 successive trials. Each curve was presented once for two seconds in a session. Curve orientation (upward or downward) also varied randomly. All curves were presented at high contrast, defined by a contour segment of the thickness of a single pixel on the screen with a luminance of 40 cd/m^2. The luminance of the screen background on which the curves were presented was 2 cd/m^2. Observers were seated comfortably in a semidark room, with their heads resting on a head-and-chin rest at a distance of 120 centimetres from the computer screen. Their hands rested on a desk with a computer keyboard, which they had to use to indicate the perceived magnitude of curvature for each stimulus by typing a number from zero to ten on the computer keyboard. Typing the "enter" key then triggered presentation of the next stimulus in the visual experiment. Observers were instructed that they were going to view a series of curves, one at a time, and were asked to produce a number between 0 and 10 that was to reflect the intensity (magnitude) of curvature they spontaneously perceive when a given curve comes up on the screen. A straight line was shown at the beginning of each individual session, solely to make sure that the observer spontaneously typed "0" on the computer keyboard and had, indeed, understood the instruction to scale curvature. Psychophysical scaling does not require giving lower and upper limits of a physical stimulus to a healthy adult human observer. Once fully developed, the nonpathological human brain is capable of reliably scaling any stimulus on the basis of internally represented (learnt) upper and lower limits [21]. In the tactile experiment, observers were instructed that they were going to explore a series of curved cables, one at a time, with the fingers of their two hands. They were asked to produce a number between 0 and 10 that was to reflect the intensity (magnitude) of curvature they perceive when a given curve is placed in their hands and to explore each curve very gently without pulling or bending the wire cables. An experimenter was present to make sure that this instruction was adhered to and that none of the observers deformed a cable. A perfectly straight wire cable was placed in the two hands of an observer at the beginning of the trials to make sure that each of them spontaneously replied "zero curvature" and that the instruction to scale curvature had been understood. The stimuli were given to the observers, in random order, one at a time. Each of the eleven curves was presented to each observer twice, once pointing upward and once pointing downward, generating a sequence of 22 successive trials as in the visual experiment.

3. Results and Discussion

The data from the two experiments were analyzed in terms of average sensations of visually and haptically (exploration with the two hands) perceived curvature (average subjective magnitudes and their standard deviations) as a function of the local curve parameter sagitta, or height of the curve (H), and as a function of the scale invariant parameter aspect ratio (H/W). These data were then subjected to mathematical modelling and compared across the two sensory modalities to examine whether common characteristics are found.

3.1. Vision. Visually perceived curvature was found to increase linearly with the local parameter sagitta, or height (H) of the curve (Figure 4(a)). The goodness of the linear fit is satisfactory, as indicated by a linear regression coefficient (R^2) of 0.98. This finding is entirely consistent with previous data [20] showing that sensations of curvature in the visual modality are a linear function of the sagitta. When plotted as a function of the aspect ratio (H/W), average visual magnitude of curvature is found to increase with the aspect ratio according to a power law (Figure 4(b)), with an exponent of 3.57 and a correlation coefficient (R^2) of 0.96. The goodness of the power fit is statistically significant ($F(1, 9) = 211.86$, $P < 0.001$).

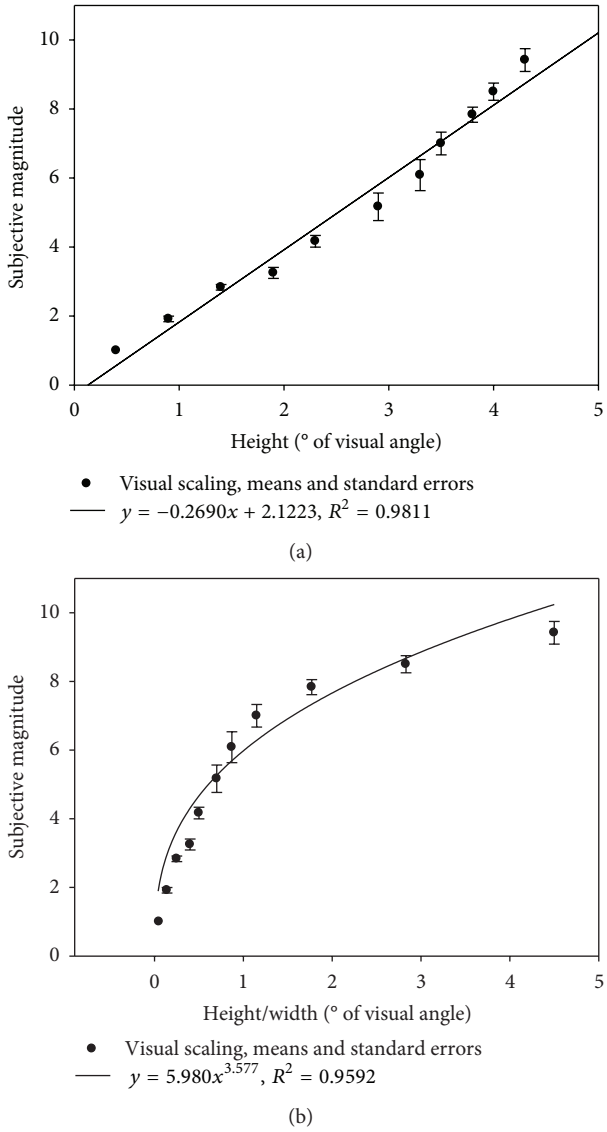

Figure 4: Visually perceived magnitude of curvature as a function of the height (H), expressed in degrees of visual angle (a), and as a function of their aspect ratio (H/W), a scale invariant parameter (b) of the curves, presented on a computer screen for visual scaling in the first experiment.

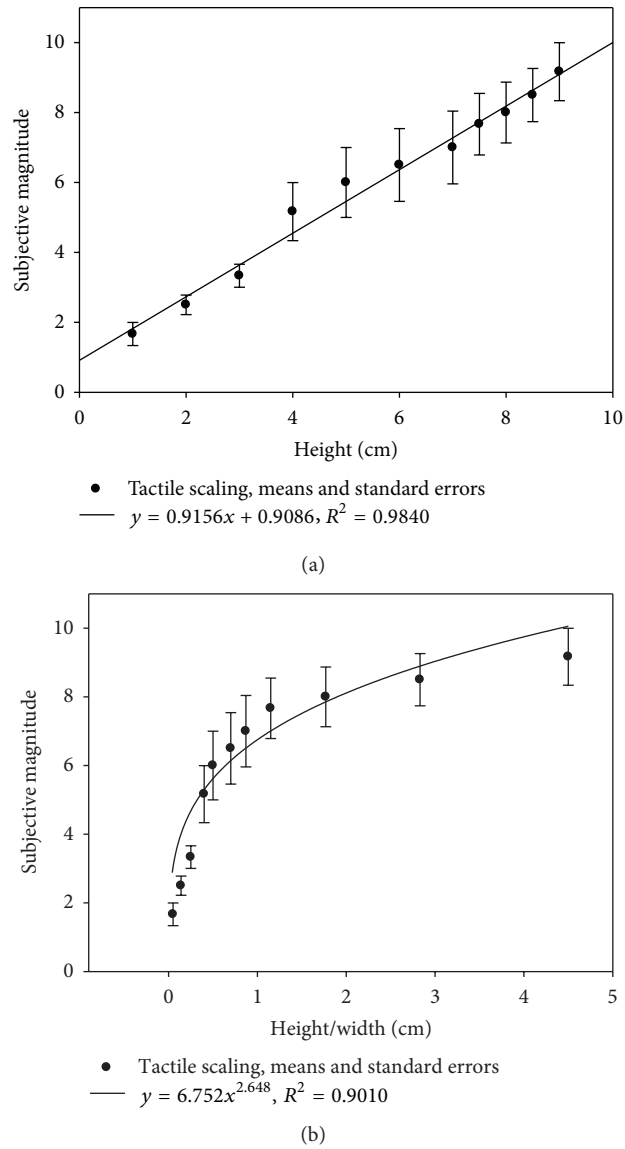

Figure 5: Haptically sensed magnitude of curvature as a function of the height (H), expressed in centimeters (a), and as a function of the scale invariant aspect ratio (H/W) of the curves (b) explored with two hands by blindfolded observers in the second experiment.

3.2. Touch. Haptically perceived curvature by seeing individuals who were blindfolded and could not see the curves and rely mostly on their vision in everyday life was, like visual curvature, found to increase linearly with the local parameter H (Figure 5(a)). The goodness of the linear fit to the tactile data was as for the visual data, with a linear regression coefficient (R^2) of 0.98. When plotted as a function of the aspect ratio (H/W), average haptically sensed magnitude of curvature is, like visually perceived curvature, found to increase with the aspect ratio according to a power law (Figure 5(b)), with an exponent of 2.6 and a correlation coefficient (R^2) of 0.90. The goodness of the power fit is statistically significant ($F(1, 9) = 81.91$, $P < 0.001$). Curvature scaled through touch by congenitally blind individuals, who never had visual experience and rely mostly on their other senses in everyday life, was also found to increase linearly with H. Analysis of the individual data of each of them (Figures 6(a) and 6(b)) shows that the goodness of the linear fits to the data of blind observers is excellent, with regression coefficients (R^2) of 0.95 and 0.98. When plotted as a function of the aspect ratio (H/W), magnitude of curvature haptically sensed by the congenitally blind observers is, again, found to increase with the aspect ratio according to a power law (Figures 6(c) and 6(d)). The goodness of the power fits is statistically significant for both observers ($F(1, 9) = 809.35$, $P < 0.001$ and $F(1, 9) = 88.41$, $P < 0.001$). The exponents of the power functions are similar (2.97 and 3.19). Whether such statistically robust data can be expected from any congenitally blind patient will

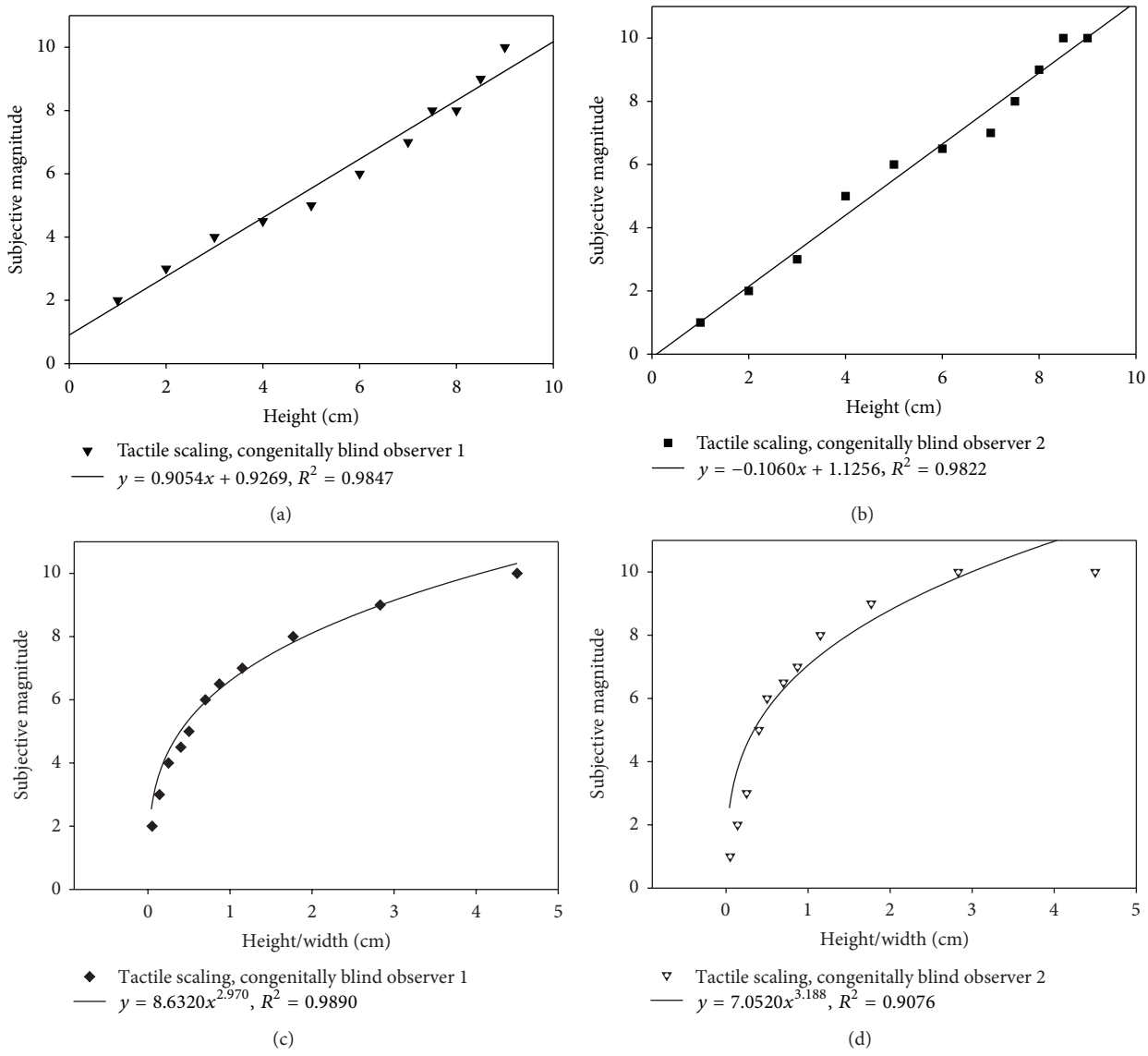

Figure 6: Haptically sensed magnitude of curvature as a function of the height (H), expressed in centimeters ((a), (b)), and as a function of the scale-invariant aspect ratio (H/W) of the curves ((c), (d)) explored with two hands by congenitally blind observers in the second experiment.

largely depend on their ability to perform the psychophysical scaling task and whether other cognitive impairments are diagnosed. We consider the two, otherwise healthy, patients tested here in this experiment as representatives of a larger population of, otherwise healthy, congenitally blind patients.

The results demonstrate that symmetric curvature is consistently scaled by the human brain on the basis of internal representations. These internal representations could be, as the results from this study here would suggest, statistically invariant when derived from either visual or tactile sensations. Such internal scaling of the spatial property of curvature would be similar to the psychophysical scaling of intensities of sensory stimuli. Earlier studies [21, 22] have demonstrated quite comprehensively that in sensory modalities such as vision, audition, olfaction, or taste, the perceived intensity of a stimulus obeys a power law, with exponents similar to those found here in our study. Physiological data and recent biologically motivated mathematical models point towards the functional significance of power laws in neural pathways where they were found to govern mechanisms through which sensory feedback signals enable the brain to adaptively control and balance motor responses to physical stimuli.

4. Conclusions

The findings from this study show that curvature representations in congenitally blind individuals, who never had any visual experience, and in seeing observers, who take in the physical world through their visual systems most of the time, are statistically linked to the same mathematical properties [23–25] of curved objects, whether these are sensed visually

on the basis of virtual representations on a computer screen or directly by the two hands on the basis of real-world objects. This rather novel finding supports the hypothesis that cognitive representations derived from vision and touch have common generic properties [3, 12, 13] that can be exploited for the study and design of technological devices to aid blind individuals to compensate for the lacking visual brain signals.

More importantly, it is shown here that the perceived magnitude of object curvature, sensed through either vision or touch, is linked by the same power law, with similar exponents for the two sensory modalities, to a scale invariant mathematical property of the physical stimuli. This is consistent with the idea that a unified representation of tactile and visual signals in the brain would necessarily involve scale invariant mechanisms at some stage of processing. The similarity of the findings reported here with earlier psychophysical data on chemosensory signal processing in the brain leads to conclude that chemical and tactile signals are at some stage integrated with common mechanisms in the brain. The power model suggested here supports other biologically motivated models of sensory integration suggesting a universal power law for the adaptive brain control and balance of motor responses [26] to chemical as well as tactile or mechanical stimuli.

References

[1] G. di Pellegrino, E. Ladavas, and A. Farnè, "Seeing where your hands are," *Nature*, vol. 388, no. 6644, p. 730, 1997.

[2] A. Farnè and E. Làdavas, "Dynamic size-change of hand peripersonal space following tool use," *NeuroReport*, vol. 11, no. 8, pp. 1645–1649, 2000.

[3] R. Held, "Visual-haptic mapping and the origin of cross-modal identity," *Optometry and Vision Science*, vol. 86, no. 6, pp. 595–598, 2009.

[4] A. Maravita, M. Husain, K. Clarke, and J. Driver, "Reaching with a tool extends visual-tactile interactions into far space: evidence from cross-modal extinction," *Neuropsychologia*, vol. 39, no. 6, pp. 580–585, 2001.

[5] A. Maravita and A. Iriki, "Tools for the body (schema)," *Trends in Cognitive Sciences*, vol. 8, no. 2, pp. 79–86, 2004.

[6] M. Tsuda, Y. Shigemoto-Mogami, S. Koizumi et al., "P2X4 receptors induced in spinal microglia gate tactile allodynia after nerve injury," *Nature*, vol. 424, no. 6950, pp. 778–783, 2003.

[7] M. S. Graziano and C. G. Cross, "The representation of extrapersonal space: a possible role for bimodal, visual-tactile neurons," in *The Cognitive Neurosciences*, M. S. Gazzaniga, Ed., pp. 1054–1057, The MIT Press, Cambridge, Mass, USA, 1995.

[8] C. L. Colby and J.-R. Duhamel, "Spatial representations for action in parietal cortex," *Cognitive Brain Research*, vol. 5, no. 1-2, pp. 105–115, 1996.

[9] Y. Iwamura, A. Iriki, and M. Tanaka, "Bilateral hand representation in the postcentral somatosensory cortex," *Nature*, vol. 369, no. 6481, pp. 554–556, 1994.

[10] G. Rizzolatti, G. Luppino, and M. Matelli, "The organization of the cortical motor system: new concepts," *Electroencephalography and Clinical Neurophysiology*, vol. 106, no. 4, pp. 283–296, 1998.

[11] P. H. Thakur, P. J. Fitzgerald, and S. S. Hsiao, "Second-order receptive fields reveal multidigit interactions in area 3B of the macaque monkey," *Journal of Neurophysiology*, vol. 108, pp. 243–262, 2012.

[12] J. J. Gibson, "Observations on active touch," *Psychological Review*, vol. 69, no. 6, pp. 477–491, 1962.

[13] J. J. Gibson, *The Senses Considered as Perceptual Systems*, Houghton-Mifflin Company, Boston, Mass, USA, 1966.

[14] J. T. Groves, "The physical chemistry of membrane curvature," *Nature Chemical Biology*, vol. 5, no. 11, pp. 783–784, 2009.

[15] N. S. Hatzakis, V. K. Bhatia, J. Larsen et al., "How curved membranes recruit amphipathic helices and protein anchoring motifs," *Nature Chemical Biology*, vol. 5, no. 11, pp. 835–841, 2009.

[16] R. J. Watt and D. P. Andrews, "Contour curvature analysis: hyperacuities in the discrimination of detailed shape," *Vision Research*, vol. 22, no. 4, pp. 449–460, 1982.

[17] R. J. Watt, R. M. Ward, and C. Casco, "The detection of deviation from straightness in lines," *Vision Research*, vol. 27, no. 9, pp. 1659–1678, 1987.

[18] D. H. Foster, D. R. Simmons, and M. J. Cook, "The cue for contour-curvature discrimination," *Vision Research*, vol. 33, no. 3, pp. 329–341, 1993.

[19] D. Whitaker and P. V. McGraw, "Geometric representation of the mechanisms underlying human curvature detection," *Vision Research*, vol. 38, no. 24, pp. 3843–3848, 1998.

[20] B. Dresp, C. Silvestri, and R. Motro, "Which geometric model for the curvature of 2-D shape contours?" *Spatial Vision*, vol. 20, no. 3, pp. 219–264, 2007.

[21] S. S. Stevens, "The direct estimation of sensory magnitudes-loudness," *The American Journal of Psychology*, vol. 69, no. 1, pp. 1–25, 1956.

[22] S. S. Stevens, *Psychophysics*, John Wiley & Sons, New York, NY, USA, 1975.

[23] K. A. Stevens, "The visual interpretation of surface contours," *Artificial Intelligence*, vol. 17, no. 1–3, pp. 47–73, 1981.

[24] J. M. Foley, N. P. Ribeiro-Filho, and J. A. da Silva, "Visual perception of extent and the geometry of visual space," *Vision Research*, vol. 44, no. 2, pp. 147–156, 2004.

[25] C. Q. Howe and D. Purves, "Natural-scene geometry predicts the perception of angles and line orientation," *Proceedings of the National Academy of Sciences of the United States of America*, vol. 102, no. 4, pp. 1228–1233, 2005.

[26] D. L. Young and C.-S. Poon, "Soul searching and heart throbbing for biological modeling," *Behavioral and Brain Sciences*, vol. 24, no. 6, pp. 1080–1081, 2001.

Hindawi Publishing Corporation
Computational and Mathematical Methods in Medicine
Volume 2013, Article ID 587543, 15 pages
http://dx.doi.org/10.1155/2013/587543

Research Article

Using State Variables to Model the Response of Tumour Cells to Radiation and Heat: A Novel Multi-Hit-Repair Approach

Stephan Scheidegger,[1] Hans U. Fuchs,[1] Kathrin Zaugg,[2] Stephan Bodis,[3,4] and Rudolf M. Füchslin[1,5]

[1] *ZHAW School of Engineering, Zurich University of Applied Science, 8401 Winterthur, Switzerland*
[2] *University Hospital Bern, Switzerland*
[3] *Radio-Onkologie-Zentrum KSA-KSB, 5001 Aarau, Switzerland*
[4] *Medical Faculty, University of Zurich, 8006 Zurich, Switzerland*
[5] *European Centre of Living Technology, 30124 Venice, Italy*

Correspondence should be addressed to Stephan Scheidegger; scst@zhaw.ch

Received 30 August 2013; Accepted 31 October 2013

Academic Editor: Roberto Serra

In order to overcome the limitations of the linear-quadratic model and include synergistic effects of heat and radiation, a novel radiobiological model is proposed. The model is based on a chain of cell populations which are characterized by the number of radiation induced damages (hits). Cells can shift downward along the chain by collecting hits and upward by a repair process. The repair process is governed by a repair probability which depends upon state variables used for a simplistic description of the impact of heat and radiation upon repair proteins. Based on the parameters used, populations up to 4-5 hits are relevant for the calculation of the survival. The model describes intuitively the mathematical behaviour of apoptotic and nonapoptotic cell death. Linear-quadratic-linear behaviour of the logarithmic cell survival, fractionation, and (with one exception) the dose rate dependencies are described correctly. The model covers the time gap dependence of the synergistic cell killing due to combined application of heat and radiation, but further validation of the proposed approach based on experimental data is needed. However, the model offers a work bench for testing different biological concepts of damage induction, repair, and statistical approaches for calculating the variables of state.

1. Introduction

In radiation oncology, mathematical models are used to describe clonogenic survival, tumour control probabilities (TCP), or normal tissue complication probabilities (NTCP). The most widely used model for cell survival is the linear-quadratic (LQ) model. The (originally empiric) model was first used by Lea and Catcheside [1] to fit radiation chromosome damage. The model is based on the observation that the logarithmic plot of the surviving cell fraction $S = N/N_0$ (with N = number of viable cells after and N_0 number of cells before radiation) versus radiation dose D can be described by a linear and a quadratic dose-dependent term ($\log S(D) = -(\alpha D + \beta D^2)$). Based on this relationship, adaption of doses for hyper- or hypofractionated radiotherapies can be calculated (e.g., application of the BED concept in clinical oncology [2]). There is also a certain need to calculate equivalent doses in the case of application of moderate hyperthermia (40–43°C) in combination with radiation (HT-RT). But the extension to combined therapies requires some knowledge of the underlying dynamic processes (radiation and heat induced formation of cellular damages, repair, etc.).

Theories about DNA lesion formation or cell survival (e.g., Chadwick and Leenhouts [3]) led to mechanistic interpretations of the LQ model. Such interpretations are problematic, due to different problems related to the LQ-formulation. Criticism of the LQ model can be based on the following points.

(1) For high doses, the shape of the survival plots is not linear-quadratic but shows a linear-quadratic-linear (LQL) behaviour [4].

(2) Cell survival not only depends upon the radiation dose applied to the cells but also upon the dose rate [5]. Dose rate dependencies can in principle be included by a dose rate factor q ($\log S(D) = -(\alpha D + q\beta D^2)$) [1, 6], but the explicit calculation of this factor is limited to certain cases of repair kinetics (e.g., first- and second-order kinetics).

(3) When applying well separated fractions of radiation (time gap larger than 24–48 h), the effect of previously applied radiation dose on the quadratic term in the LQ law (βD^2) fades away. In this context, Oliver [7] introduced a concept using a biological dose equivalent without taking a step toward a dynamic description of the system. Here as well, a dose rate factor or dose protraction factor can be introduced to correctly calculate the survival for split dose experiments or fractionated radiotherapy (with the same limitations as in point 2, if the time gap between the fraction is too short to ensure complete repair).

(4) Survival curves are different for the different phases of the cell cycle. Mitotic cell response to radiation can be characterized in a logarithmic plot of the surviving cell fraction by a linear curve with a steep slope compared to the nonmitotic cells. A similar behaviour is proposed for apoptotic cells [8], whereas the nonapoptotic counterpart can be well characterized by a linear-quadratic curve using different radiation sensitivity coefficients. Also high LET-radiation is leading to a linear curve in the logarithmic survival plot, which has been interpreted in the framework of dual radiation action [9]. For all these reasons, the radiation sensitivity coefficients have to be adapted.

(5) Some cell lines exhibit a phenomenon called low dose hypersensitivity [10, 11]. This seems to be a strong indication for a repair mechanism, which is triggered by the radiation. The resulting logarithmic survival curve is far from a simple linear-quadratic shape.

(6) If radiation is applied in combination with moderate hyperthermia (typical temperatures between 40°C and 43°C), a synergistic effect between radiation and heat can be observed [12]. Heat seems to act as radiosensitizer but does not kill cells directly below 44°C. In principle, the radiosensitivity coefficients of the LQ model can be regarded as temperature dependent, but the effect is also depending upon the duration of heating and the time gap between heating and irradiation. A set of coefficients is therefore only valid for a well-defined application of heat and radiation. Interestingly, both heat prior and after irradiation have an impact on cell killing [13]. This seems to be a result of the underlying dynamic processes, which are not covered by adapted LQ models.

The points listed here (1–6) have a common aspect. Linear-quadratic-linear shapes, dose rate dependence, repair during fractionated radiotherapy, different shapes of survival curves for different situations, and so forth are based on dynamic processes. The use of the LQ-formula and the adaption of the radiosensitivity parameters to a specific situation [14] may be used at best for describing experimental data but definitely does not contribute to a profound understanding of the biological system. Therefore, the mechanistic interpretation of the LQ model seems to be problematic.

It is important to point out the intension behind modelling. The aim of modelling can be prediction,—for example, in the case of radiation oncology the prediction of TCP for a modified fractionation. In our view at least similarly important goal is the effect upon learning. Dynamic modelling can be used to test ideas about the dynamics in a system. Modelling requires making ideas and concepts explicit. This leads to revisions of the ideas often before the results of model based computer simulation are available. The proposed model framework in this paper will focus on modelling as basis for in silico experiments helping us to learn about the relevant dynamic processes responsible for cellular response to radiation only or radiation and heat. Prediction is then considered a subsequent goal.

To overcome the limitations of the LQ model, dynamic models using ordinary differential equations (ODE) have been developed. A good example is the lethal-potentially-lethal- (LPL) model of Curtis [15]. The model describes the formation of lethal and potentially lethal DNA lesions and is able to describe the linear-quadratic-linear behaviour of the logarithmic survival curves and to fit the dose rate dependencies observed by Wells and Bedford [5]. The surviving fraction is calculated by using Poisson statistics. This makes the inclusion of or extension to the dynamic interplay between different tumour subpopulations hard. Non-Poisson approaches have been evaluated by Vassiliev [16]. The proposed multi-hit model is not a dynamic model based on ODE. In contrast to a model based on the calculation of DNA lesions, a population based model offers a more natural and direct approach to the dynamic aspects at the tissue level (interaction of tumour cells with host tissue and vascularisation or forming of subpopulations with a different radiosensitivity as observed *in vivo*). The extension of the model to intratumour heterogeneity seems to be highly important since malignancy of tumours is coupled with genetic instability [17]. This was the main motivation for developing the Γ-LQ model [18]. The key idea of this model is the use of a differential equation for cell killing (for which the LQ law is a solution) and to substitute the absorbed dose D by a biological dose equivalent Γ. This biological dose equivalent is assumed to be proportional to the radiation damage relevant to cell death. Cellular repair is considered by a kinetic model for this dose equivalent. With this model, it is also possible to reproduce the linear-quadratic-linear behaviour of large fraction doses and to approach dose rate dependence similar to the LPL model of Curtis. The Γ-LQ model has been extended to the synergistic effect of heat and radiation [19].

All LQ-type models including dynamic models such as the Γ-LQ model and also models for DNA lesions kinetics (e.g., model of Curtis) are based on the following biological

concept. Lethal damages are not reparable and are produced depending linearly upon the dose rate $R = dN/dt$ (e.g., LQ model with number of viable cells $N : dN/dt = -\alpha R$). This leads to a linear graph in the logarithmic survival plot ($\int dN = -\alpha \int R dt = -\alpha D$). An additional cell killing occurs due to sublethal DNA lesions produced by previously applied radiation doses. In the LQ-type model, this is realised by a second term ($-\beta D^2$). In principle, the LQ law can be interpreted as a solution of the following ODE [18]: $dN/dt = (-\alpha - 2\beta D) \cdot NR$. The cell killing part of the Γ-LQ model is derived by substituting the absorbed dose D by the biological dose equivalent $\Gamma : dN/dt = (-\alpha - 2\beta\Gamma) \cdot NR$. In each of these formulations, the linear graph in the logarithmic survival plot is bent downward by an additional term to a linear-quadratic or a linear-quadratic-linear shape (Figure 1). In this view, the linear-quadratic behaviour is a result of a previous, remaining (not repaired) radiation damage. This damage can be considered as sublethal lesions which combined with lethal lesions by further radiation.

Observations of low dose hypersensitivity or the synergistic effect of moderate hyperthermia with radiation or even the fact that mitotic or apoptotic cells are exhibiting a steep slope of the $\log S$-graph are indicating another type of underlying dynamic process. The linear-quadratic shape in the survival diagrams could be regarded as a result of the combination of induction of potentially lethal DNA damages and a repair process which is bending the $\log S$-curve upward (Figure 1). The biological rationale for this type of dynamics is the following. Ionizing radiation produces DNA lesions with different degree of severity. It seems to be difficult to distinguish between lethal and nonlethal damages since double strand breaks can be repaired as well by homologue recombination or by non-homologues end-joining repair (NHEJ). A radiation dose of 1 Gy produces ca. 25 double strand breaks [20]. Depending on the cell line, cell surviving fraction is of the order of 70–80% [20]. Consequently, lethality would be a result of not repaired, possibly multiple double strand breaks. As soon as a repair process is activated, potentially lethal damages can fade away and the survival will increase.

Regarding the processes of repair and the role of repair proteins, cell survival or cell killing can be considered as a result of the dynamic interplay between DNA and (attached or associated) proteins. Possibly, this does not only include proteins of specific repair pathways but also proteins stabilizing the DNA strands (such as histones) and membrane proteins. In irradiated cells, DNA and proteins are exposed to radiation. In a mammalian cell nucleus, the number of ionisations is of the order of 10^5 per 1 Gy of X-rays, most of them are ionisation of water molecules [20, 21]. At higher doses, severe damages of proteins may be expected as well due to ionisation and subsequent molecular changes leading to protein denaturation. This could result in a decreased repair capacity at higher doses and, in consequence, in a reduced upward correcting of the survival curve as illustrated in Figure 1. Such an approach may be supported by the observation that moderate hyperthermia (40–45°) is affecting proteins [12, 22]. These thermal damages seem to be responsible for the synergistic effect of heat combined with radiation.

A question regarding the dynamic interplay between (repair) proteins and DNA arises: can such a type of process explain the linear-quadratic or linear-quadratic-linear dose response of the survival. This leads to the following hypothesis: a model reflecting dynamic interaction of DNA (DNA damages triggering repair process) and proteins (responsible for repair and also susceptible to radiation damages) can describe aspects of the impact of radiation such linear-quadratic (-linear) behaviour and dose rate dependence of survival.

A key problem of such an approach is the handling of the complexity of biological systems. However, some aspects of biological systems may help to reduce the complexity of the model. First, biological systems are evolved—the biological control processes have certain robustness. As long as the cellular system is not driven too much away from its normal conditions, the cellular response may be covered by a low dimensional description. Second, the response of biological systems can be understood as an emergent phenomenon;—therefore, it could be helpful to use a phenomenological description of the observed dynamics instead of a molecular, mechanistic one. This idea is also supported by the fact that the evolutionary process is governed by the selection of the phenotype (semantic level) although the mutations occur on the molecular (syntactic) level. Some ideas inspired by statistical mechanics could be applied. Cellular damages on the molecular level may be approached by state variables. Similar to thermodynamic quantities such as entropy, variables describing cellular disorder (state of an ensemble) could be employed. Following the idea of a check sum principle, cellular response can be regarded as being governed by such state variables.

The Multi-Hit-Repair (MHR) model presented in this paper is based on a model framework that incorporates the idea of using variables of state. This framework allows expansion to synergistic interplay of heat and radiation. Therefore, the effect of heat and radiation is included. In the following sections, the model framework and MHR model will be clarified. The results using the MHR model as basis for computer simulations (in silico experiments) will focus on the radiation part. The model framework presented here is intended to offer a work bench for testing different ideas or hypothesis about cellular repair processes.

2. Materials and Methods

The first subsection concerning the general model (Section 2.1) describes a model framework which is referring to the relation between the different quantities/variables of state. Based on this, the state variables used in the MHR model will be defined (Section 2.2) and finally the influence of the variables of state upon cell killing will be modelled by a population model for tumour cells.

2.1. General Model Structure. The model framework consists of different levels characterising different aspects of the

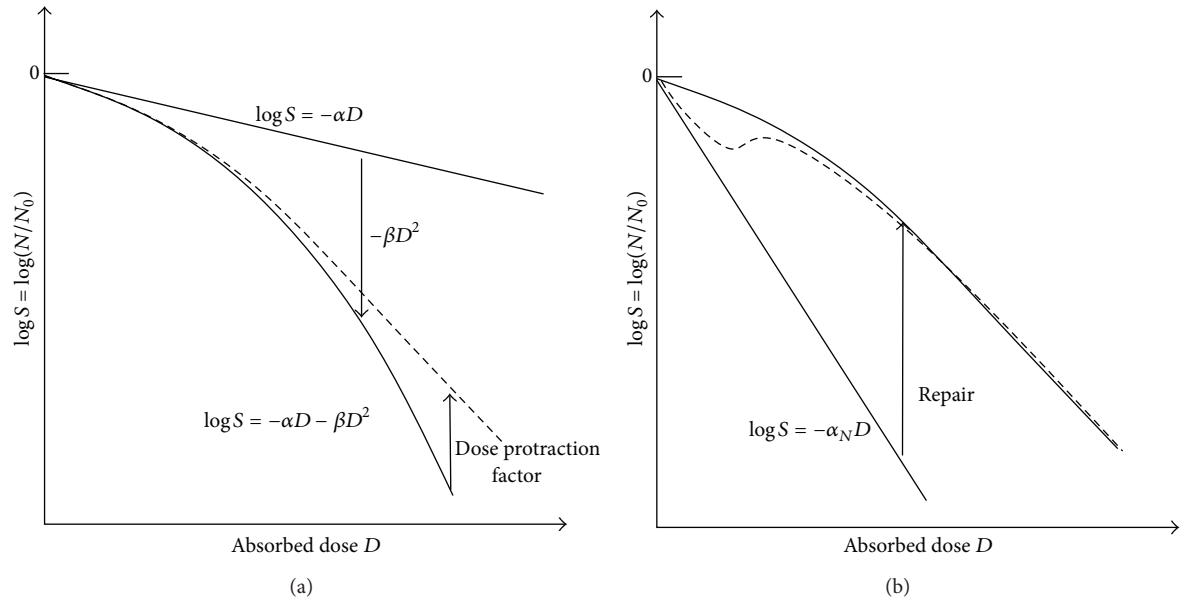

Figure 1: Comparison of two different concepts for describing cell killing or cell survival (schematic illustration). The left diagram (a) shows a correcting down approach (bending down principle by a term describing additional cell killing due to previously acquired sub-lethal lesions). To correct the curve to the observed linear-quadratic-linear shape and to include dose rate dependences, dose protraction factors (e.g., Lea-Catcheside dose protraction factor [1, 6]) have been proposed. The right diagram (b) illustrates a correcting up approach due to the repair of potentially lethal lesions. If the activation of repair will need a certain dose, low dose hypersensitivity (dashed curve) can be explained [23].

biophysical system (Figure 2). At the top level in Figure 2, the physical quantities (caloric quantities) are illustrated. In the case of heat, more or less all molecules absorb energy (large amount of energy absorbed in a distributed manner). In contrast to heat, the energy absorption in the case of ionizing radiation occurs very locally. Szasz and Vincze [24] pointed out that thermal destruction of malignant cells needs energy to break chemical bonds (E_R in Figure 2). This part of the energy does not produce an increase of the temperature T. In principle, the total thermal energy absorbed in the tissue U (including the part used for chemical modifications) can be considered a thermal dose in analogy to the radiation dose D, which is the absorbed radiation energy per mass. Also in the case of radiation, not all the energies lead to chemical reactions since very weak interactions (especially between secondary electrons and atoms) are producing heat without molecular modifications. However, in clinical routine, temperature (for hyperthermia) and absorbed dose (for radiation therapy) are accessible to measurements and therefore used for dosimetric purposes.

The energy deposition in the cells leads to chemical reactions and therefore to a change of the (molecular or structural) configuration. This is incorporated in the general structure by a layer with configuration quantities. Referring to the concepts of statistical mechanics and thermodynamics, these configuration quantities are represented by variables of state. Unfortunately, the microscopic approach for calculating these quantities is, in contrast to ideal gases and crystals, very difficult or impossible. In Section 2.2, a proposal for a macroscopic approach to these state variables for heat and radiation will be made.

In the model framework shown in Figure 2, the configuration quantities or state variables influence the cellular system in two different ways. On the one hand, radiation and heat are damaging proteins with the result of a reduced repair capacity. On the other hand, radiation induced DNA damages are responsible for removing vital cells out of the mitotic cycle. In a more theoretic view, the variables of state are producing a "signal strength" which governs cell death and cellular repair. In the proposed concept, we distinguish clearly between variables of state in the sense of configuration quantities and information (here information about the biological impact upon the system). This information will be decoded at the level of the population, where the "signal strengths" directly influence the transformation of cells from vital to damaged cells.

The use of compartmental population models at the outcome level allows the inclusion of the mitotic cycle (mitotic cell population and cells in the G1-, S-, and G2-phase). The radiosensitivity of mitotic cells, cells in the G2-phase, and cells in the S-phase is different. Also subpopulations with different radiosensitivity are observed in malignant tumours. Therefore, to guide understanding, tumour response in patients and clinical outcome, population-based models are advantageous. However, in this paper a simplified model using one population of viable (tumour) cells is used to compare the survival to experimental data from defined cell lines.

2.2. Variables of State and Repair Probability

2.2.1. Description of Radiation Induced Protein-Related Damages. The key idea of the Γ-LQ model [18] is the substitution

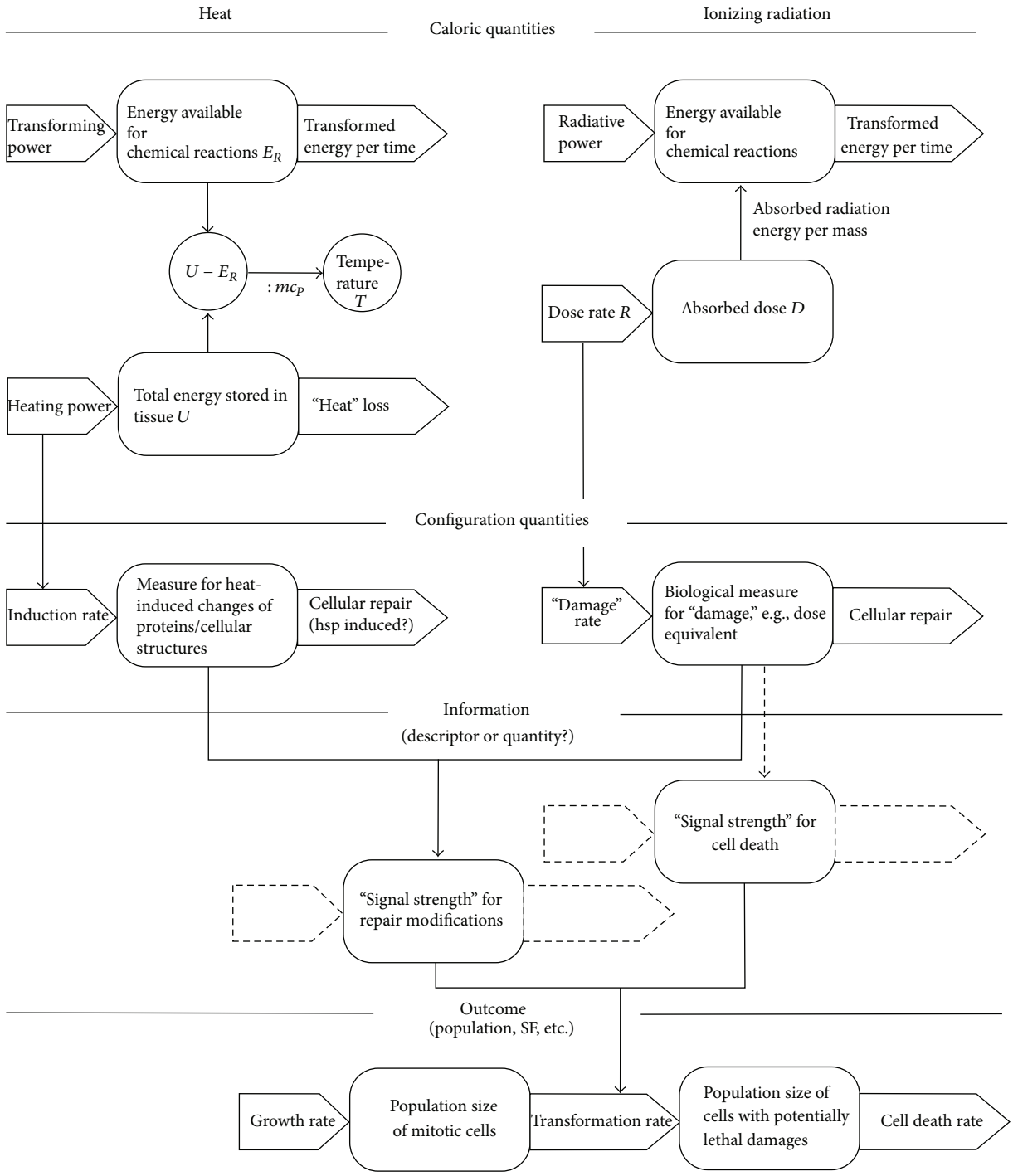

Figure 2: General model structure as a model framework. The structures consisting of boxes and thick arrows symbolise integrators. In the case of extensive quantities, the boxes can be regarded as storage elements and the arrows as flows. The left side of the diagram illustrates the effect of heat, the right side the effect of radiation. The population model is drawn in a simplistic manner. For the MHR model, a chain of population is used (see Section 2.3). In constructing this scheme, we have been critical of attempts to conflate concepts of thermodynamic entropy, statistical entropy, and information. We believe that distinguishing between the three (as caloric, number of configurations and information) leads to advances in understanding systems and processes. See also Corning and Kline [25, 26].

of the absorbed dose by a biological dose equivalent Γ. In the framework of the Γ-LQ model, the dose equivalent Γ is assumed to be proportional to the average number of unrepaired sub-lethal entities per cell produced by irradiation. The discussion in [18] focused on DNA damage repair kinetics, since the dose equivalent was intended to describe DNA-related damages. The model described in this paper uses a different approach. The dose equivalent Γ is dedicated to describing protein-related, radiation induced damage. It is assumed that this dose equivalent increases linearly with the dose rate R. According to the Γ-LQ model, the following kinetic model is chosen for Γ [18]:

$$\frac{d\Gamma}{dt} = R - f(\Gamma). \tag{1}$$

Here, $f(\Gamma)$ is a function of Γ representing the kinetics of repair of protein-related damage. In principle, different types of repair kinetics may be taken into consideration. In the following, a simplistic approach using first-order kinetics is used: $f(\Gamma) = \gamma\Gamma$. The biological dose equivalent can be calibrated to the absorbed dose. By using this calibration, Γ must satisfy the following condition:

$$\lim_{t\to\infty}\left[\int_{-\infty}^{t} f(\Gamma(\tau)\cdot)\, d\tau\right] = \lim_{t\to\infty}[D(t)] = D_{\text{tot}}. \tag{2}$$

For the biological dose equivalent, the unit of the absorbed dose Gray (Gy) can be used. The implicit assumption behind this definition is that no saturation of damages will be achieved by radiation. For very high doses (typically above 200 Gy), this is possibly not the case, since all cellular structures seem to be damaged in a severe manner and even membrane lipids might play an important role for interphase death at such high doses [27]. In the formalism described in the following section, Γ is used to describe only the impact on proteins involved in the repair of DNA-related lesions. Therefore, the concept is limited to DNA-related cell death mechanism (mitotic cell death, aspects of apoptotic cell death will be discussed later).

2.2.2. Description of Heat-Induced Protein-Related Damages. In contrast to radiation, the energy deposition during heating of tissues/cells occurs in a distributed manner. All molecules absorb energy. By exceeding a temperature of 45–46°C (depending on tissue type), proteins will be heavily affected by heat. This leads to a different type of description of damages. Functional proteins can be converted by conformal changes or more generally by chemical reactions into non-functional forms. Johnson et al. [28] applied the Arrhenius law to enzymatic reactions and denaturation of enzyme protein. The activation energies of proteins in melanoma cell lines were determined from Arrhenius plots by Rofstad and Brufstad [29]. Above 43°C, an activation energy E_a of 700 kJ/mol was found. Below, the value for E_a varies between 1118 and 2190 kJ/mol. Based upon these findings, the following temperature depending, simplistic approach is chosen. The amount of functional repair proteins is described by a state variable Υ. If no thermal damage occurs and a maximal repair capacity is reached, this variable is set equal to 1:Υ = 0. If all repair protein molecules are damaged by heat and therefore are nonfunctional, the value should be Υ = 0. In this case, a variable Λ describing the amount of nonfunctional, damaged repair proteins is set to the value 1. The following system is assumed to describe the dynamics of thermal induction and repair (e.g., by Chaperones) of protein damages:

$$\begin{aligned}\frac{d\Upsilon}{dt} &= -k_1\Upsilon + k_2\Lambda,\\ \frac{d\Lambda}{dt} &= k_1\Upsilon - k_2\Lambda,\\ k_1 &= \kappa\cdot e^{-E_a/RT},\end{aligned} \tag{3}$$

where $R = 8.314\,\text{J}\cdot\text{mol}^{-1}\,\text{K}^{-1}$ and T is the temperature. The constants k_1 and k_2 are related to thermal degradation and repair of proteins. Here, first order kinetics is assumed. With these model assumptions, different types of repair proteins are not distinguished and only one value for activation energy is used. When going deeper into the processes of cellular repair, the formalism represented by (1) should be applied separately to different mechanisms of repair such as homologues recombination or nonhomologues end-joining repair. This point will be discussed later.

2.2.3. Calculating Repair Probability Using Γ *and* Λ. According to the systemic structure in Figure 2, the variables of states Γ and Λ are configuration quantities describing radiation- and heat-induced damages (disorder). In a simplistic manner, they cover chemical and structural changes in the cell. The question arising is how these changes lead to a change of the cellular control processes. In Figure 2, the configuration quantities are distinguished from information, but in principle, the configuration quantities are encoding information about the state of the cellular system. This information converts in some way to signal strength for repair modification (increasing or reducing repair capacity). One possible approach is to define a probability of repair P which depends upon Γ and Λ : $P = P(\Gamma, \Lambda)$. Moreover, we choose a very simplistic approach: the repair probability decreases monotonically with increasing values of Γ and Λ. Induced repair leading to low dose hypersensitivity is not considered. The following relations are used:

$$\begin{aligned}\left[\frac{\partial P}{\partial \Gamma}\right]_{\Lambda=\text{const}} &= -\mu_\Gamma P,\\ \left[\frac{\partial P}{\partial \Lambda}\right]_{\Gamma=\text{const}} &= -\mu_\Lambda P.\end{aligned} \tag{4}$$

This leads to the following functional dependence:

$$\begin{aligned}P(\Gamma) &= P_\Gamma = e^{-\mu_\Gamma\Gamma},\\ P(\Lambda) &= P_\Lambda = e^{-\mu_\Lambda\Lambda}.\end{aligned} \tag{5}$$

In the case of P_Γ and P_Λ being statistically independent, the total probability is given by

$$P = P_\Gamma P_\Lambda = e^{-(\mu_\Gamma\Gamma+\mu_\Lambda\Lambda)}. \tag{6}$$

2.3. Multi-Hit-Repair Approach and Population Model. The transformation of the impact of radiation upon cell killing and the impact of radiation and heat upon cellular repair can be realised at the level of a population model. Vital cells (N = number of cells or population size) can be converted to damaged cells by radiation in the following way: the probability to hit the DNA is proportional to the number of cells in the population N and the dose rate R. The cell transformation rate is therefore given by $dN/dt = \dot{N} = -\alpha RN$ (using a radiosensitivity coefficient α). The cells affected by radiation will be removed from the mitotic cycle and converted to damaged cells (population size L_1). It has to be pointed out here that the cells of population L_1 are not considered lethally damaged cells and can be recovered by repair or converted to more damaged cells by a second (population size L_2) and a third hit (population size L_3). No criterion for lethality is applied here—lethality may be regarded as a result of a single hit or of several hits/damages, which will not be repaired. At this point, no exact definition for a "hit" is given (this will be discussed in Section 4). Applying this concept, the following system model describing a chain of populations can be derived:

$$\begin{aligned}
\frac{dN}{dt} &= -\alpha RN + r\left(L_1\right),\\
\frac{dL_1}{dt} &= \alpha RN - \alpha RL_1 - r\left(L_1\right) + r\left(L_2\right),\\
\frac{dL_k}{dt} &= \alpha RL_{k-1} - \alpha RL_k - r\left(L_k\right) + r\left(L_{k+1}\right).
\end{aligned} \tag{7}$$

The index k represents the number of hits. It is assumed that the probability of hits and subsequently the cell transformation rate are the same for all the populations. Moreover, the functions $r(L_k)$ introduced in (7) describing the rates of repair are assumed to be independent of the number of hits. The repair function $r(L_k)$ incorporates the repair probability equation (6) and, in the case of a first order process, may be written as $r(L_k) = c_r e^{-(\mu_\Gamma \Gamma + \mu_\Lambda \Lambda)} \cdot L_k$.

The model represented by (7) is incomplete since the elimination of cells after acquiring radiation induced damages is not considered. A prominent example of such an elimination process is the apoptosis. Apoptotic cell death can be regarded as a result of deactivated or not executed repair processes due to the activation of a separate elimination pathway. Such a process can be included in (7) by an additional elimination rate $\dot{L}_{k,e}$ which is assumed to be a linear function of the population size of damaged cells $\dot{L}_{k,e} = c_e L_k$:

$$\begin{aligned}
\frac{dN}{dt} &= -\alpha RN + c_r e^{-(\mu_\Gamma \Gamma + \mu_\Lambda \Lambda)} \cdot L_1,\\
\frac{dL_1}{dt} &= \alpha RN\\
&\quad - \left(\alpha R + c_r e^{-(\mu_\Gamma \Gamma + \mu_\Lambda \Lambda)} + c_e\right)\\
&\quad \cdot L_1 + c_r e^{-(\mu_\Gamma \Gamma + \mu_\Lambda \Lambda)} \cdot L_2,
\end{aligned}$$

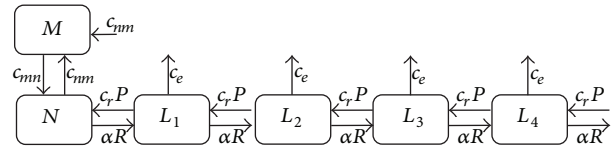

Figure 3: Illustration of the population model. The model flow chart includes a mitotic cell population as well (population size M). The flows (rates) between the populations can be found by multiplying the given constants by the corresponding population size (population where the arrow starts). P is the repair probability from (6).

$$\begin{aligned}
\frac{dL_k}{dt} &= \alpha RL_{k-1}\\
&\quad - \left(\alpha R + c_r e^{-(\mu_\Gamma \Gamma + \mu_\Lambda \Lambda)} + c_e\right)\\
&\quad \cdot L_k + c_r e^{-(\mu_\Gamma \Gamma + \mu_\Lambda \Lambda)} \cdot L_{k+1}.
\end{aligned} \tag{8}$$

These are in principle the core equations of the proposed Multi-Hit-Repair (MHR) model. The underlying structure of the model in (8) is illustrated in Figure 3. There, a mitotic cell population is included as well. For fast growing tumours *in vivo*, the inclusion of this population could be essential since a significant part of mitotic cells is present having a different radiosensitivity.

For practical reasons, the chain of populations has to be interrupted at a certain number of hits and the repair of the subsequent populations in the chain will be neglected. Including this cutoff, the model in (9) should be slightly modified. The last population in the chain is described by the following equation (where $k_{\max}$ denotes the maximal value of k used for simulation):

$$\begin{aligned}
\frac{dL_k}{dt} &= \alpha RN_{k-1}\\
&\quad - \left(\alpha R + c_r e^{-(\mu_\Gamma \Gamma + \mu_\Lambda \Lambda)} + c_e\right)\\
&\quad \cdot L_k + c_r e^{-(\mu_\Gamma \Gamma + \mu_\Lambda \Lambda)} \cdot L_{k+1},\\
\frac{dL_{k_{\max}}}{dt} &= \alpha RN_{k_{\max}-1}\\
&\quad - \left(\alpha R + c_r e^{-(\mu_\Gamma \Gamma + \mu_\Lambda \Lambda)} + c_e\right) \cdot L_{k_{\max}}.
\end{aligned} \tag{9}$$

The error resulting from the cutoff at $k_{\max}$ will be investigated in Section 3.2.

3. Results

For Sections 3.1–3.3, only the radiation part of the model (8) is investigated (P is set to P_Γ and $P_\Lambda = 1$). In these sections, different radiobiological aspects are discussed. To give an overview, the used parameters are summarized in Table 1.

The differential equations (1) and (3) (see Section 3.4) and (8) are integrated numerically by a Runge-Kutta algorithm (4th order). The time steps were set to values between $\Delta t = 10^{-3}$ h and $\Delta t = 5 \cdot 10^{-5}$ h.

Table 1: Parameters in use for the radiobiological investigations of Sections 3.1–3.3. The typical range in column 3 represents the range used for fitting radiobiological data.

Parameter	Related equation	Typical range
α	$\frac{dN}{dt} = -\alpha RN + c_r e^{-(\mu_\Gamma \Gamma)} \cdot L_1$	
	$\vdots$	0.5–2 Gy^{-1}
	$\frac{dL_k}{dt} = \alpha R L_{k-1} - \left(\alpha R + c_r e^{-(\mu_\Gamma \Gamma)} + c_e\right) \cdot L_k + c_r e^{-(\mu_\Gamma \Gamma)} \cdot L_{k+1}$	
c_r	Same as for α	4–100 h^{-1}
c_e	Same as for α	1–60 h^{-1}
μ_Γ	Same as for α	0.2–1.0 Gy^{-1}
γ	$\frac{d\Gamma}{dt} = R - \gamma\Gamma$	1–10 h^{-1}
R	Same as for α and γ	0.49–240 Gy/h

If not otherwise indicated in the following sections, $k_{\max}$ is set to a value of 6. In Section 3.2, the effect due to the cutoff at $k_{\max}$ according to (9) is investigated for a typical radiobiological example.

If not stated otherwise, the parameters which we present for the different variants of investigated models have been obtained by evolutionary optimization procedures. For a set of parameters $(A_1, \ldots, A_n)$ with $(A_1, \ldots, A_n)$ either equal to $(\alpha, c_r, c_e, \gamma, \mu_\Gamma)$ or $(\alpha, c_r, c_e, \gamma, \mu_\Gamma, \kappa, k_2, \mu_\Lambda)$, we apply the following procedure. First, we compute $N(A_1, \ldots, A_n, t_R, d_R, t_H, d_H, t)$. As before, N indicates the size of the population, t_R the time at which irradiation starts, d_R is the duration of the irradiation (determined by the dose), t_H represents the time at which the heating starts and d_H the respective duration (t_H and d_H are omitted in pure RT models). Durations and time intervals are chosen such that they correspond to experimental data. Differences between the logarithms of computed and measured values are squared and summed up; this sum constitutes the fitness function $f(A_1, \ldots, A_n)$ which is to be minimized. We employ a rather simple evolutionary procedure. Let $(A_1^i, \ldots, A_n^i)$ the parameters of the ith generation. We set $(A_1^{i+1}, \ldots, A_n^{i+1}) = ((1 + \varepsilon(i))r_1^i A_1^i, \ldots, (1 + \varepsilon(i))r_n^i A_n^i)$ with r_k^i a uniformly distributed random variable between −1 and 1. The parameter $\varepsilon(i)$ is a small number which is reduced over the course of the evolution. We used 10^5 steps, $\varepsilon(i)$ was set to 0.02 for the first 66000 steps and then reduced to 0.01. If $f(A_1^{i+1}, \ldots, A_n^{i+1}) \leq f(A_1^i, \ldots, A_n^i)$, $(A_1^{i+1}, \ldots, A_n^{i+1})$ remained unchanged; otherwise it was set back to $(A_1^i, \ldots, A_n^i)$. The method is basically a simple gradient search, which we have chosen because the fitness landscape turned out to be smooth, though flat. This flatness means that parameter variations most often have only little impact upon the outcome and therefore the results of our optimizations have to be interpreted with some caution. Our choices fit well, but different sets of parameters fit almost as well. In order to cope with the possibility of local optima, we performed the optimization several times with different initial values. We observed convergence into the same optimum and therefore concluded a simple gradient search to be appropriate for the models we investigated. However, further improvements, for example, the addition of additional mechanisms, may require more sophisticated optimization methods. A method suitable for chemical systems (i.e., systems with an in general smooth fitness landscape) with a number of continuous parameters comparable to the models presented in this work is presented in Forlin et al. [30]. Not all chemical systems have a smooth fitness landscape and this holds even more for biological systems such as eukaryotic cells with versatile functionality. A method applicable for categorical as well as continuous systems and nonsmooth fitness landscapes is discussed in Ferrari et al. [31]. A general framework, ParamILS, for parameter tuning (or as Hutter et al. [32] prefer to call it, algorithm configuration) is described in [32]. ParamILS is suitable for numerical, ordinal, and categorical parameters. The ability to deal with categorical parameters is of specific value when different states of cells are not anymore connected in a sequential manner, but, for example, cell differentiation is part of the model.

3.1. Apoptotic Cell Death versus Nonapoptotic Cell Death. Apoptotic cell death can be characterised by a linear function with a steep slope in the logarithmic cell survival curve. In the framework of the MHR model in (8) and Figure 3, this behaviour can be interpreted as an efficient elimination process (described by the elimination constant c_e), which prevents a repair of severe or critical cellular lesions. In this case, the equation describing the vital cell population N simplifies to $dN/dt = -\alpha RN$ and therefore $\ln S = -\alpha \mathrm{D}$. In principle, the case with apoptotic cell death can be considered as a baseline cell killing according to Figure 1(b). Data from apoptotic cell killing can be used to determine the baseline radiobiological constant α. In Figure 4, a fit of data from Hardenbergh et al. [8] is shown. The p53 wild type (nondeficient, radiation sensitive) murine fibroblast exhibits the typical linear relationship with a steep slope. The radiosensitivity coefficient α was determined by Harrigan et al. ($\alpha = 1.1\ \mathrm{Gy}^{-1}$ for the natural logarithm of S : $\ln S = -\alpha D$). For the fit of the data by the model in Table 1, the same value is used. The p53-deficient, radioresistent fibroblasts are characterized by a linear-quadratic behaviour in the logarithmic survival plot. The radiosensitivity coefficients were determined by Harrigan et al. to $\alpha = 0.13\ \mathrm{Gy}^{-1}$ and

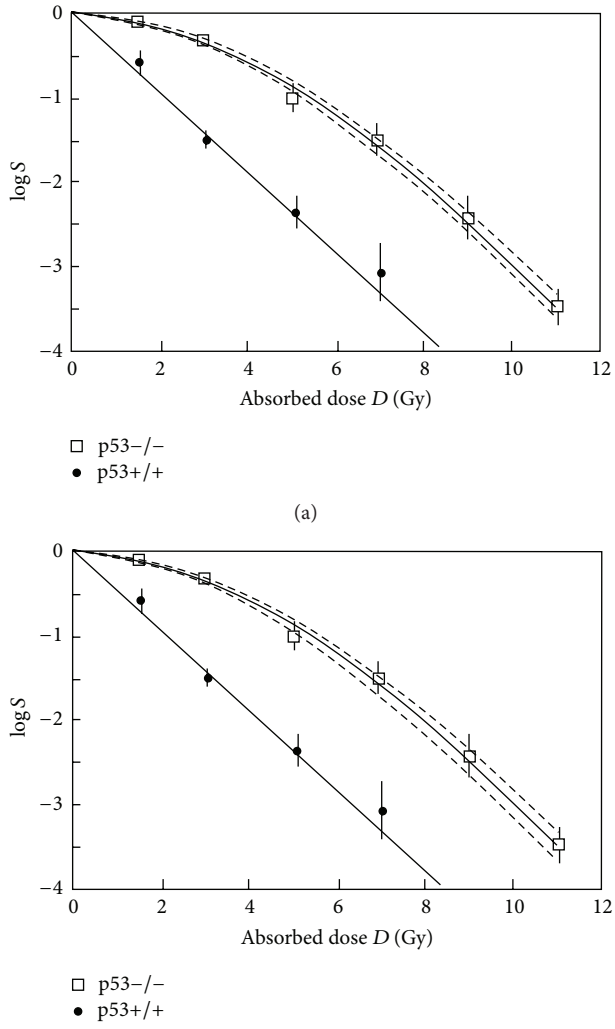

Figure 4: Fit of cell survival in the case of apoptotic (p53+/+) and nonapoptotic (p53−/−) cell death. The solid straight line is given by $\log S = -(1.1 \cdot \log e) \cdot D$. The dashed lines indicate the standard deviation calculated for varying repair parameters, (a) variation of c_r between 84 and 120 h^{-1}; (b) variation of μ_Γ in the range of 0.45–0.55 Gy^{-1}.

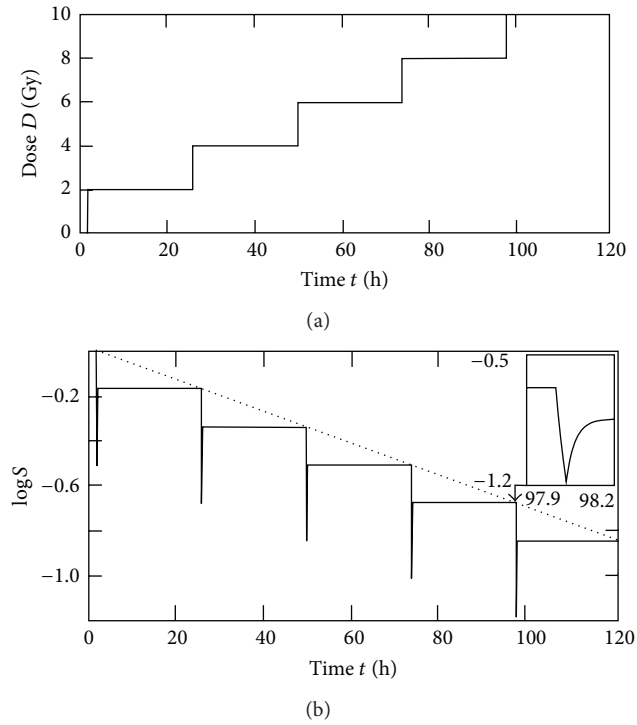

Figure 5: Fractionated radiotherapy course used for cutoff evaluation: (a) For every dose step (fraction of 2 Gy), a constant reduction of $\log S$ results. Therefore, the (upper) envelope in (b) is characterized by a straight line (dotted line in the lower figure). This corresponds with the concept of Oliver [7] and the radiobiological models of Curtis [15] and Scheidegger [18] and represents the case of complete repair.

$\beta = 0.054\,Gy^{-2}$ (for $\ln S = -(\alpha D + \beta D^2)$). For the data fit using the MHR model, the baseline value for $\alpha (= 1.1\,Gy^{-1})$ is used. A good fit can be achieved with $c_r = 100\,h^{-1}$, $c_e = 10\,h^{-1}$, $\mu_\Gamma = 0.5\,Gy^{-1}$, and $\gamma = 1.45\,h^{-1}$ at a dose rate of 60 Gy/h. To test the sensitivity of the MHR model to variations of the repair constants, c_r and μ_Γ are varied and the resulting standard deviations are given (dashed lines). To keep the standard deviation within the error limits of the experimental data, c_r can be varied by ±16% and μ_Γ can be varied in the range of ±10%, respectively.

3.2. Cutoff of Subpopulation with Damages. For simulations, the chain of populations in the MHR model has to be cutoff at certain k_{max} (cf. Section 2.3, (9)). The related effect can be investigated for typical examples by comparing the resulting survival. For the evaluation, the parameters from Section 3.1 were used (nonapoptotic cell killing). For testing the influence of the dose rate R, the values of R were varied in the range of 14–240 Gy/h (typical range for conventional linear accelerators used in radiotherapy). A common radiotherapy course consists of several fractions of 1.5–2.5 Gy with spacing between the fractions of at least one day. Therefore, the cutoff effect was evaluated for 5 fractions of 2 Gy (at a dose rate of 60 Gy/h). The resulting logarithmic survival as function of time is shown in Figure 5. In agreement with the model of Curtis [15] and the Γ-LQ model [18], the envelope of the $\log S$-graph is given by a straight line (upper envelope as dotted line in Figure 5).

To evaluate the cutoff effect also for different doses per fraction, fraction sizes of 8 Gy at a dose rate of 240 Gy/h were investigated.

In Figure 6, the cutoff effect is illustrated by the coefficient $\log S(k_{max})/\log S(k_{max} = 6)$ and the difference $\Delta \log S = \log S(k_{max} = 6) - \log S(k_{max}) = \log(S(k = 6)/S(k_{max}))$. In the case of the coefficient (Figure 6(a)), the influence of different doses per fractions or different cumulative doses is small. The maximum variation was found for $k_{max} = 1$ and varying doses between 8 and 40 Gy at a dose rate of 240 Gy/h: average ± standard deviation of the factor is $\log S(k_{max} = 1)/\log S(k_{max} = 6) = 1.2516 \pm 0.0045$. This quantity seems

Table 2: Parameters used for fitting dose rate dependent data from Wells and Bedford [5].

Parameter	Figure 7(a)	Figure 7(b) thick (thin) lines
α	0.79 Gy^{-1}	0.42 (0.7) Gy^{-1}
c_r	0.51 h^{-1}	100 (4) h^{-1}
c_e	0.14 h^{-1}	55 (1) h^{-1}
μ_Γ	0.036 h^{-1}	0.5 (0.5) Gy^{-1}
γ	9.23 h^{-1}	1.45 (1.45) h^{-1}

to be more or less independent of the dose in the tested range (2–40 Gy). The effect of the dose can be shown by the difference $\Delta \log S$ (Figure 6(b)). The relationship between ΔlogS and the (discrete) values of $k_{\max}$ can be approximated by an exponential function (in the case of $D = 10\,\text{Gy}$ $\Delta \log S = 1.001 \cdot e^{-3.72 \cdot k_{\max}}$ for all data points and $\Delta \log S = 1.001 \cdot e^{-3.37 \cdot k_{\max}}$ for $k_{\max} \in \{1, 2\}$).

For all investigated cases, the cutoff effect becomes small for $k_{\max} > 4$. The reason for this behaviour lies in the structure of the MHR model. The probability for recovery of cells (transformation back to the population N) with more than 4 impacts (radiation induced DNA lesions) can be neglected compared to the elimination rate $c_e L_k$.

3.3. Dose Rate Dependence. It can be expected that a model using five free parameters is able to fit linear-quadratic curves since a two-parameter law is doing so as well. Fitting of linear-quadratic-linear data obtained for high doses per fraction is more difficult [4]. An important test of a radiobiological model is given by its dynamic behaviour at different dose rates. We carried out this test by fitting experimental data from Wells and Bedford [5]. The results are shown in Figure 7.

A good fit can be obtained with parameter values given in Table 2 (values for Figure 7(a)). Compared to the p53-deficient murine fibroblasts in Section 3.1, the C3H10T1/2 cells have a smaller value for the LQ parameter β (0.02 Gy^{-2} instead of 0.054 Gy^{-2}) and a slightly higher value for α. This in principle leads to a less pronounced shoulder compared to larger β values. In comparison with the parameter values for the MHR model, the values of c_r and c_e in Figure 7(a) differ significantly from those used for the murine fibroblasts (c_r: 0.51 h^{-1} instead of 100 h^{-1} and c_e: 0.14 h^{-1} instead of 10 h^{-1}). For testing parameter values for c_r and c_e which are closer to those in Sections 3.1 and 3.2 and not optimized fits with higher values are carried out as well. The results for two selected cases are shown in Figure 7(b). The corresponding parameter values are given in Table 2. In this set of parameters, the values for c_r, μ_Γ, and γ are identical to the parameter values used in Section 3.1. Depending on the weighing of the data points and allowed parameter range, different sets of parameter values can be found to achieve a (more or less good) fit of the dose rate dependence.

A good radiobiological model should fit the dose rate dependencies over a certain range. But for simplistic models, a limitation due to the different processes involved in the cellular response onto radiation can be expected. In particular for very high dose rates or high doses per pulse, changes in the radiobiochemical cascade cannot be excluded. Today, new linear accelerators for clinical use with flattening filter free (FFF) beams are available. To investigate possible biological effects, Lohse et al. [33] treated glioblastoma cell lines with doses of 5 and 10 Gy. The highest dose rate values are clearly above the range given in Table 1 (up to 1440 Gy/h). It has to be pointed out that a pulsed beam with high doses per pulse was used. In this paper, the data obtained from these experiments are used to explore the high dose rate limit of the MHR model. In Figure 8, a fit of the logarithmic survival of T98G glioblastoma cells irradiated at different dose rates is shown.

At very high doses, the $\log S$ curves in Figure 8 are exhibiting a linear-quadratic-linear shape. For dose rates above 240 Gy/h, the values for $\log S$ are changing only in a small range (−1.113 at 240 Gy/h; −1.129 at 360 Gy/h; −1.158 at 1440 Gy/h; −1.168 at 3000 Gy/h). The point at 10 Gy and 1440 Gy/h clearly cannot be fitted by this parameter set. With changed parameters, a fit of the 1440 Gy/h-data is possible for the price of a poor fit of the points at 12 Gy/h. No parameter set enabling a fit of all data points was found by the applied optimisation algorithm.

3.4. Inclusion of Hyperthermia. The synergistic effect of heat and radiation depends upon the time gap between application of hyperthermia and radiation [13]. A model for the synergistic effect should cover this dynamic aspect. To test the dynamic behaviour of the extended MHR model, the experimental data from Sapareto et al. [13] are used. With respect to Table 1, the inclusion of the effect of heat in the MHR model requires additional parameters, which are summarized in Table 3. Selected results of different calculations (with and without using evolutionary optimization) are shown in Figure 9.

The parameter optimisation using only the data points given by Sapareto et al. leads to a shifted baseline (dashed line, Figure 9). It can be assumed that with a sufficient large time gap, the cell survival would be the same as without applying heat (baseline at $\log S = -1.21$). This assumption is included in the fit represented by the solid line in Figure 9. Two additional, hypothetical baseline points (with double weight) at a positive and negative time gap of 7 h are used for fitting. The resulting graph covers more or less the experimental data points. Comparing the corresponding parameter values found by the optimisation algorithm with those ones in Sections 3.1–3.3, clearly different values for γ (very small), c_r, and c_e are resulting. A solution (not optimized fit) which is closer to the parameter values of Sections 3.1–3.3 is shown as dotted line in Figure 9. This graph starts at the baseline and recovers the baseline when radiation is applied after heat with a time gap larger than 2 h. Parameter sets similar to those used in the previous sections generally lead to a smaller effect (shifted baseline and covering the data points at $\log S = -2.55$ or baseline at $\log S = -1.21$ and maximal cell killing at $\log S = -2.0$).

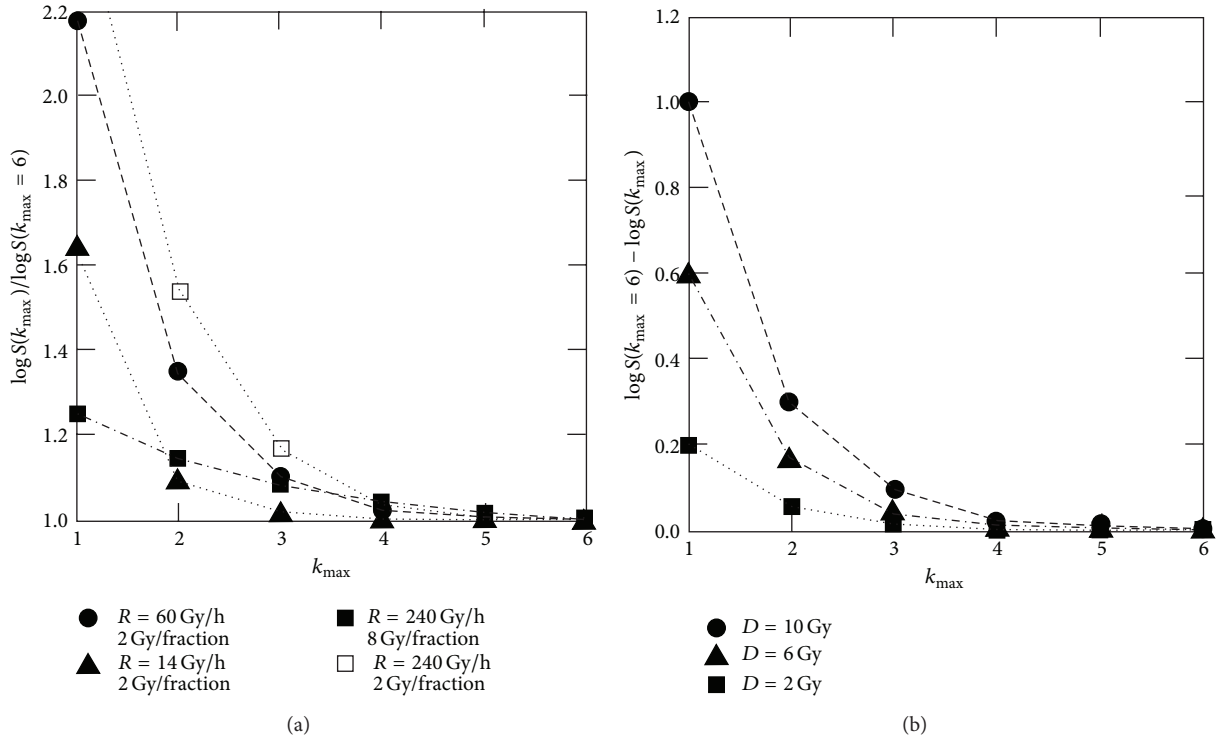

FIGURE 6: Effect of cutoff of the population chain at different dose rates R. In the left diagram, factors between log S-values for a specific k_{max} and log$S$-values $k_{max} = 6$ are shown. These values exhibit a nonlinear dose rate dependence but are nearly independent of the cumulative dose for a specific fractionation scheme (2 Gy fractions according to Figure 5). The situation becomes different for larger doses per fraction (example in the Figure 8 Gy fractions). Due to the high dose rate and the low γ-value (1.45 h^{-1}), the dose equivalent Γ does not reach a steady state and rises up to approximately 8 Gy (7.83 Gy). This leads to a higher repair rate and therefore to a slightly higher influence of the populations with $k < 1$. In the right diagram, the differences of the log S-values are given. This quantity is dependent of the cumulative dose (in this figure applied in fractions of 2 Gy) and can be approximated by an exponential function (for the discrete values of k_{max}).

TABLE 3: Additional parameters to model synergistic effect of heat and radiation.

Parameter	Related equation, remarks	Value used for Figure 9 solid (dotted; dashed) lines
κ	$k_1 = \kappa \cdot e^{-E_a/RT}$ κ is specific for $T < 43^\circ$C, $T > 43^\circ$C is not used in Figure 9	$\frac{a \cdot 10^{-3}\ h^{-1}}{e^{-(E_a/(R\cdot(38+273.16)K))}}$ with $a = 0.56$ (1; 0.89)
E_a	Same as for κ (3)	1528 kJ for $T < 43^\circ$C [23]
k_2	$\frac{d\Upsilon}{dt} = -k_1\Upsilon + k_2\Lambda$; $\frac{d\Lambda}{dt} = k_1\Upsilon - k_2\Lambda$	2.76 (2; 11.17) h^{-1}
μ_Λ	(8)	29.19 (20; 31.26)

4. Discussion and Conclusions

Our hypothesis—that a model reflecting dynamic interaction of DNA and repair proteins (such as the MHR model) is able to describe aspects of the impact of radiation such linear-quadratic (-linear) behaviour and dose rate dependence of survival—can be confirmed wivth some restrictions. The MHR model is exhibiting linear-quadratic and linear-quadratic-linear behaviour as observed in radiobiological experiments. It catches in an intuitive way the behaviour of apoptotic and nonapoptotic (radiation induced) cell death. Also, fractionation of radiation as is usual for standard radiation therapy is covered correctly.

Regarding the chain of populations which is used in the model, at least populations up to 4-5 hits (radiation induced, potentially lethal DNA damaged) should be included. No specifications about radiation induced damages ("hits") are made. Regarding the fact that a dose of 1 Gy (X-rays) is producing ~25 double strand breaks, a "hit" cannot be equivalent to a double strand break in general. Since the probability of a second double strand break in the proximity of a previously induced double strand break is proportional to D^2, a hit also cannot be interpreted as the formation of a damage consisting of two double strand breaks with a certain special correlation. Possible interpretations of the term "hit" may take into account that possibly not all locations on

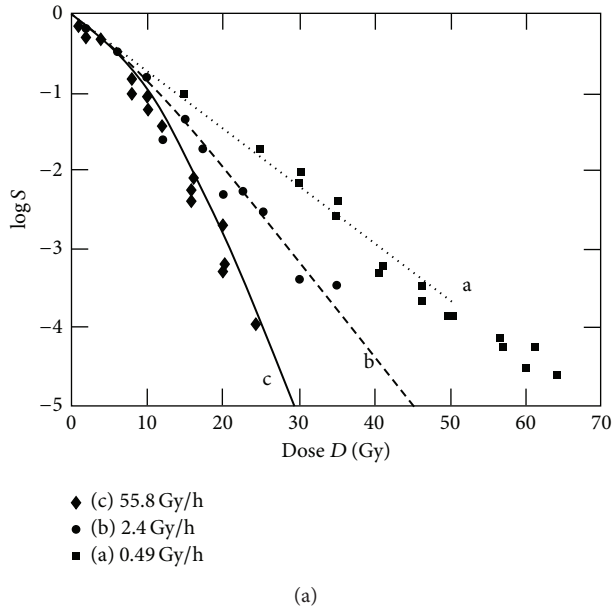

(a)

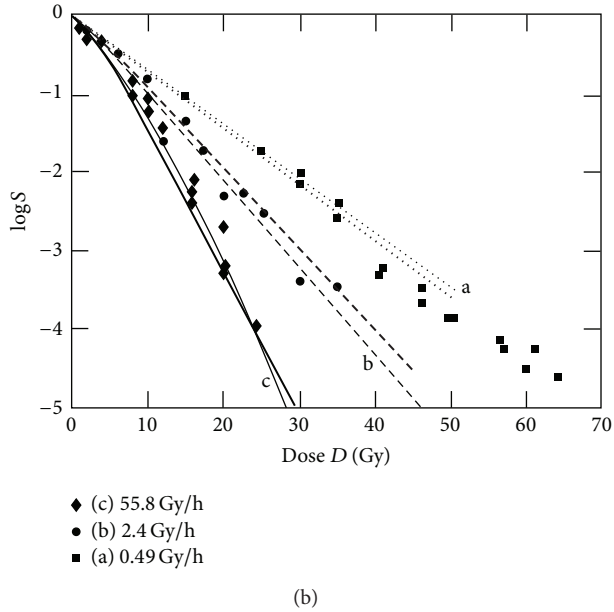

(b)

Figure 7: Fit of experimental data form Wells and Bedford [5]. C3H10T1/2 cells with the LQ parameters $\alpha = 0.1366\,\mathrm{Gy}^{-1}$ and $\beta = 0.02\,\mathrm{Gy}^{-2}$, irradiated at different dose rates. The parameters used for fitting are given in Table 2. (a) shows a fit which corresponds to the fit of Curtis [15] using the LPL model, (b) shows two, not optimized fits with higher values for c_r and c_e.

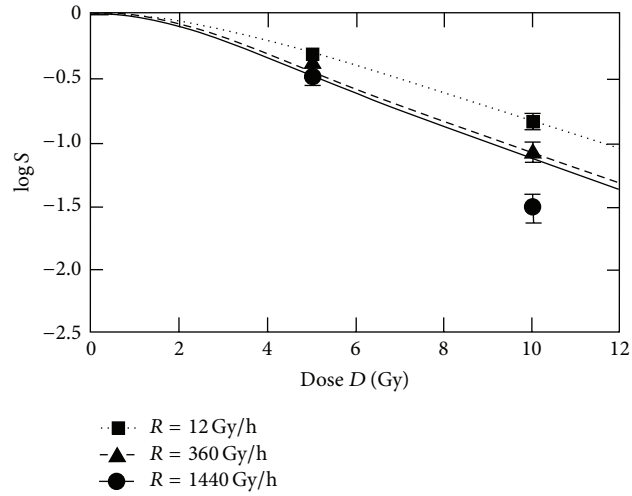

Figure 8: Clonogenic survival of T98G glioblastoma cells at different dose rates. The parameter values for fitting are $\alpha = 0.27\,\mathrm{Gy}^{-1}$, $\gamma = 1.45\,\mathrm{h}^{-1}$, $c_r = 90\,\mathrm{h}^{-1}$, $c_e = 19\,\mathrm{h}^{-1}$, and $\mu_\Gamma = 0.8\,\mathrm{Gy}^{-1}$.

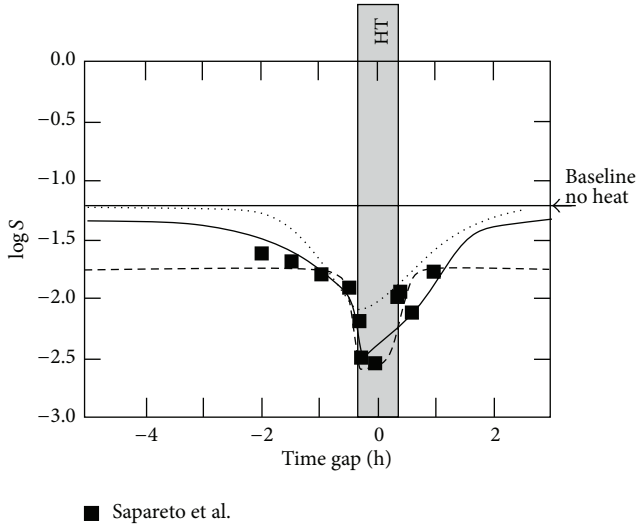

Figure 9: Fit of experimental data (redrawn) from Sapareto et al. [13]. Chinese hamster cells were irradiated with 5 Gy prior (negative time gap) or after heat (positive time gap). Heat (HT) is applied during 40 min (±20 min of point 0 on the time gap axis). Temperature T during heating was 42.5°C. Heat specific parameter values are given in Table 3. Radiation specific parameter values: solid line (optimized) $\alpha = 1.89\,\mathrm{Gy}^{-1}$, $c_r = 191.7\,\mathrm{h}^{-1}$, $c_e = 0.97\,\mathrm{h}^{-1}$, $\mu_\Gamma = 0.96\,\mathrm{Gy}^{-1}$, $\gamma = 6.77 \cdot 10^{-3}\,\mathrm{Gy}^{-1}$; dotted line (not optimized) $\alpha = 1.1\,\mathrm{Gy}^{-1}$, $c_r = 6.1\,\mathrm{h}^{-1}$, $c_e = 2\,\mathrm{h}^{-1}$, $\mu_\Gamma = 0.5\,\mathrm{Gy}^{-1}$, $\gamma = 1.45\,\mathrm{Gy}^{-1}$; dashed line (optimized without baseline points) $\alpha = 1.18\,\mathrm{Gy}^{-1}$, $c_r = 6.42\,\mathrm{h}^{-1}$, $c_e = 8.92\,\mathrm{h}^{-1}$, $\mu_\Gamma = 0.096\,\mathrm{Gy}^{-1}$, $\gamma = 0.699\,\mathrm{Gy}^{-1}$.

a chromosome have the same sensitivity for formation of severe chromosomal damages due to double strand breaks. In addition, the different (protein- and DNA-related) parts of the MHR model could refer to the different pathways of repair. We cannot exclude the possibility that a certain (very fast) repair process (with a small sensitivity to protein damages) is included as well in the α coefficient. Otherwise, one would expect a similar α value for all cell lines which should reflect a cell killing according to the approximately 25 double strand breaks per Gy. Assuming Poisson statistics, the surviving fraction is given by the number of unrepaired lesions n: $S = e^{-n} = e^{-\alpha D}$. Without any repair process, the baseline cell killing would be described by $\alpha = 25\,\mathrm{Gy}^{-1}$. This is clearly higher than the values used for fitting in Section 3.1, where the baseline was determined from the apoptotic cell line.

The probability of induction of DNA-related lesions is assumed to be constant (represented by the parameter α). This represents in principle the case of independent events. We cannot exclude the possibility that previous damage events affect subsequent hits and α varies with the population order k. If the induction of different types of potentially lethal DNA-related lesions and their probability to be repaired is different, the model structure (population chain) will transform to a tree-structure consisting of branches of damaged populations with a specific α.

The (observed) dose rate dependence of cellular survival can be fitted at least in a limited range. The comparison of the experimental data of Wells and Bedford [5] exhibits a problematic aspect of fitting biological data by using the MHR model. Different weighting of data points leads to different sets of parameter values. Especially the values for c_e and c_r show a wide spread. The uncertainty of biological data seems to have a strong impact on the sharpness of the parameter values.

The dose and dose rate limitations may be cell line dependent. Especially the observation of an increased cell killing effect of glioblastoma cells at very high dose rates and high dose values per fraction (10 Gy) seems not to be covered correctly by the model. Reasons for this could be related to the triggering of different chemical reactions in the radio-biochemical cascade at very high doses per pulse, radiation induced, severe damage of mitochondria with subsequent energy depletion or destruction of other cellular structures. Regarding the radio-biochemical cascade, changes of instantaneous levels of radicals may not be affected since radical formation occurs within 10^{-14} s and recombination of H and OH radicals (and production of H_2 and H_2O_2) is starting at 10^{-12} s [21]. Therefore, potential dose rate dependent modifications of the radio-biochemical chain are expected in subsequent steps. It has to be pointed out here that the additional cell killing effect at very high doses per pulse was observed for a few cell lines (T98G and U87MG glioblastoma cell lines which are very radio resistant) and FFF beams [33]. Some experimental absence of dose rate dependence at ultrahigh dose rates is found by different authors [34, 35]. In a review article, Ling et al. [20] concluded that the dose rate effect in external radiotherapy is governed by the beam-on time, not by the average linear accelerator (linac) dose rate, nor by the instantaneous dose rate within individual linac pulses (even for FFF machines). This is an important point especially for intensity modulated radiotherapy (IMRT) where during beam-on time not the whole target volume is irradiated due to time dependent beam collimation. In principle, the target dose in IMRT or in high precision radiotherapy [36] is applied in a prolonged way compared to non-IMRT treatments. In this view, the results of the MHR model are in agreement with these findings. Variations in the dose rate above 240 Gy/h have only a small impact. Time gaps during irradiation due to changing beam collimations have a similar impact like lowering the dose rate to values where the model shows stronger dose rate dependence.

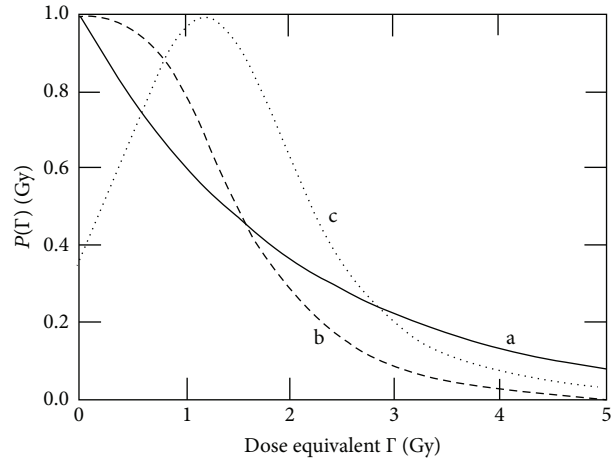

Figure 10: Different approaches for describing the dose equivalent dependence of the repair probability. (a) Exponential function with $\mu_\Gamma = 0.5\,\mathrm{Gy}^{-1}$ as used in Sections 3.2–3.4, (b) sigmoidal function, and (c) possible function in the case of low dose hypersensitivity.

The assumption of a monotonically decreasing repair probability (4) and (5) is questionable. To model low dose hypersensitivity, a radiation induced repair process should be considered. Such a process can be covered by a Gaussian function using a characteristic dose Γ_c [23]: $e^{-\xi(\Gamma-\Gamma_c)^2}$. This leads to a modified model and a different (8): $dL_k/dt = \alpha R L_{k-1} - (\alpha R + c_r \cdot e^{-\xi(\Gamma-\Gamma_c)^2} + c_e) \cdot L_k + c_r \cdot e^{-\xi(\Gamma-\Gamma_c)^2} \cdot L_{k+1}$. Moreover, sigmoidal courses of $P(\Gamma)$ should be considered (Figure 10). A rationale for such an approach may be the assumption of a certain stability of repair protein at low doses. Also a combination of the different patterns of dose-equivalent dependencies could be taken into consideration, since radiation affects all proteins. The initial induction of protein-related damage may be unspecific when regarding direct ionisation and possibly more specific when damages occur via radical formation (indirect pathway). The impact upon the repair capacity (covered by the repair probability) is dependent upon the sensitivity of the different repair pathways regarding radiation induced damage. As a consequence, a more or less unspecific initial damage process would transform into a protein (and pathway) specific response.

The MHR model is a cell population based approach and can therefore be extended to a tumour model with subpopulations characterized by different radiosensitivity. To model effects of cell cycle synchronisation, the inclusion of mitotic cells is important as well. Such extensions may possibly be very important to understand the tumour dynamics *in vivo*. Varying radiosensitivity of different groups of cells may override small differences, for example, due to dose rate dependence above 240 Gy/h. When evaluating tumour volumes of irradiated tumours *in vivo*, the mixture of tumour cells with different radiosensitivity could be essential. In contrast, the overall survival may be governed by the subpopulation with the lowest radiosensitivity.

The verification of the model including the synergistic effect of heat and radiation is difficult. By fitting the experimental data from Sapareto et al. [13], unexpected parameter

values were found (compared to those ones used for radiation only). Fits with parameter values close to the Sections 3.1–3.3 are able to cover the experimentally observed time gap dependence, but only with a shift of the maximum cell killing or the baseline in the order of $\Delta\log S = 0.5$. One reason could be an additional, less time gap dependent (slower) process which is not covered by the model. Another explanation of the shift of the baseline is that this shift is an artefact of the optimisation procedure, which only considers the measured data points, meaning mostly points off the baseline. In principle, this weakness of the evolutionary procedure is easily resolved by introducing "artificial" data points on the baseline for very large time gaps. However, such a procedure should be properly justified and corroborated by some experiments. A better estimation of the parameter values and validation of the model is only possible by using better experimental data. Such data should be generated with a clearly characterized cell line and should not only include time gap dependence but also dose rate dependence (with and without radiation). In addition, time resolved data about DNA- and protein-related repair would help to validate the proposed approach.

From a clinical perspective, future research should refer the problem of thermal dose concept based on variables of state. Recently in the clinical routine applied thermal dose concepts such as the thermal isoeffect dose method (cumulative equivalent minutes (CEM) concept [37]) are completely misreading aspects of dynamic interplay between radiation and heat or varying time gaps between application of heat and radiation.

A remaining question is how to cover complex interaction of damage induction and repair by variables of state. Specific experiments dedicated to this question and delivering dynamic (time resolved) data about protein damages and repair activity would be helpful to refine the concept of state variables. The hypothetic impact of possible differences between the radiation induced response of different cell lines found by such experiments could be evaluated by the (modified) MHR model. In this context, the MHR model offers a work bench for testing concepts and ideas about the control of cellular repair.

Conflict of Interests

The authors declare that there is no conflict of interests regarding the publication of this paper.

References

[1] D. E. Lea and D. G. Catcheside, "The mechanism of the induction by radiation of chromosome aberrations in Tradescantia," *Journal of Genetics*, vol. 44, no. 2-3, pp. 216–245, 1942.

[2] B. Jones, R. G. Dale, C. Deehan, K. I. Hopkins, and D. A. Morgan, "The role of biologically effective dose (BED) in clinical oncology," *Clinical Oncology*, vol. 13, no. 2, pp. 71–81, 2001.

[3] K. H. Chadwick and H. P. Leenhouts, "A molecular theory of cell survival," *Physics in Medicine and Biology*, vol. 18, no. 1, article 7, pp. 78–87, 1973.

[4] M. Guerrero and X. A. Li, "Extending the linear-quadratic model for large fraction doses pertinent to stereotactic radiotherapy," *Physics in Medicine and Biology*, vol. 49, no. 20, pp. 4825–4835, 2004.

[5] R. L. Wells and J. S. Bedford, "Dose-rate effects in mammalian cells. IV. Repairable and nonrepairable damage in noncycling C3H10T1/2 cells," *Radiation Research*, vol. 94, no. 1, pp. 105–134, 1983.

[6] R. G. Dale, "The application of the linear-quadratic dose-effect equation to fractionated and protracted radiotherapy," *The British Journal of Radiology*, vol. 58, no. 690, pp. 515–528, 1985.

[7] R. Oliver, "A comparison of the effects of acute and protracted gamma-radiation on the growth of seedlings of *Vicia faba*," *International Journal of Radiation Biology and Related Studies in Physics, Chemistry, and Medicine*, vol. 8, pp. 475–488, 1964.

[8] P. H. Hardenbergh, P. Hahnfeldt, L. Hlatky et al., "Distinct mathematical behavior of apoptotic versus non-apoptotic tumor cell death," *International Journal of Radiation Oncology Biology Physics*, vol. 43, no. 3, pp. 601–605, 1999.

[9] A. M. Kellerer and H. H. Rossi, "A generalized formulation of dual radiation action," *Radiation Research*, vol. 75, no. 3, pp. 471–488, 1978.

[10] P. Lambin, E. P. Malaise, and M. C. Joiner, "Might intrinsic radioresistance of human tumour cells be induced by radiation?" *International Journal of Radiation Biology*, vol. 69, no. 3, pp. 279–290, 1996.

[11] C. Mothersill, C. B. Seymour, and M. C. Joiner, "Relationship between radiation-induced low-dose hypersensitivity and the bystander effect," *Radiation Research*, vol. 157, no. 5, pp. 526–532, 2002.

[12] C. Streffer, "Molecular and cellular mechanisms of hyperthermia," in *Thermoradiotherapy and Thermochemotherapy*, M. H. Seegenschmiedt, P. Fessenden, and C. C. Vernon, Eds., pp. 47–74, Springer, New York, NY, USA, 1995.

[13] S. A. Sapareto, L. Hopwood, and W. Dewey, "Combined effects of x-irradiation and hyperthermia on CHO cells for various temperatures and orders of application," *Radiation Research*, vol. 44, pp. 221–233, 1978.

[14] N. A. Franken, A. L. Oei, H. P. Kok et al., "Cell survival and radiosensitisation: modulation of the linear and quadratic parameters of the LQ model (Review)," *International Journal of Oncology*, vol. 42, no. 5, pp. 1501–1515, 2013.

[15] S. B. Curtis, "Lethal and potentially lethal lesions induced by radiation—a unified repair model," *Radiation Research*, vol. 106, no. 2, pp. 252–270, 1986.

[16] O. N. Vassiliev, "Formulation of the multi-hit model with a non-Poisson distribution of hits," *International Journal of Radiation Oncology, Biology, Physics*, vol. 83, no. 4, pp. 1311–1316, 2011.

[17] R. G. Bristow and R. P. Hill, "Hypoxia, DNA repair and genetic instability," *Nature Reviews Cancer*, vol. 8, no. 3, pp. 180–192, 2008.

[18] S. Scheidegger, G. Lutters, and S. Bodis, "A LQ-based kinetic model formulation for exploring dynamics of treatment response of tumours in patients," *Zeitschrift fur Medizinische Physik*, vol. 21, no. 3, pp. 164–173, 2011.

[19] S. Scheidegger, R. M. Füchslin, G. Lutters, and S. Bodis, "Dynamic modelling of the synergistic effect of hyperthermia and radiotherapy," *Radiotherapy and Oncology*, vol. 103, Supplement 1, pp. S360–S361, 2012.

[20] C. C. Ling, L. E. Gerweck, M. Zaider, and E. Yorke, "Dose-rate effects in external beam radiotherapy redux," *Radiotherapy and Oncology*, vol. 95, no. 3, pp. 261–268, 2010.

[21] G. E. Adams and D. G. Jameson, "Time effects in molecular radiation biology," *Radiation and Environmental Biophysics*, vol. 17, no. 2, pp. 95–113, 1980.

[22] J. R. Lepock, "Protein denaturation: its role in thermal killing," in *Radiation Research: A Twentieth-Century Perspective*, W. C. Dewey, M. Edington, R. J. M. Fry, E. J. Hall, and G. F. Withmore, Eds., pp. 992–998, Academic Press, New York, NY, USA, 1991.

[23] S. Scheidegger and R. M. Füchslin, "Kinetic model for dose equivalent—an efficient way to predict systems response of irradiated cells," in *Proceedings of the ASIM Workshop (ASIM '11)*, 2011.

[24] A. Szasz and G. Y. Vincze, "Dose concept of oncological hyperthermia: heat-equation considering the cell destruction," *Journal of Cancer Research and Therapeutics*, vol. 2, no. 4, pp. 171–181, 2006.

[25] P. A. Corning and S. J. Kline, "Thermodynamics, information and life revisited—part I: "To Be or Entropy," *Systems Research and Behavioral Science*, vol. 15, no. 4, pp. 273–295, 1998.

[26] P. A. Corning and S. J. Kline, "Thermodynamics, information and life revisited—part II: "Thermoeconomics" and 'Control information'," *Systems Research and Behavioral Science*, vol. 15, no. 6, pp. 453–482, 1998.

[27] H. Wolters and A. W. T. Konings, "Membrane radiosensitivity of fatty acid supplemented fibroblasts as assayed by the loss of intracellular potassium," *International Journal of Radiation Biology*, vol. 48, no. 6, pp. 963–973, 1985.

[28] E. H. Johnson and M. J. Polisar, *The Kinetic of Molecular Biology*, John Wiley & Sons, New York, NY, USA, 1954.

[29] E. K. Rofstad and T. Brustad, "Arrhenius analysis of the heat response *in vivo* and *in vitro* of human melanoma xenografts," *International Journal of Hyperthermia*, vol. 2, no. 4, pp. 359–368, 1986.

[30] M. Forlin, I. Poli, D. de March, N. Packard, G. Gazzola, and R. Serra, "Evolutionary experiments for self-assembling amphiphilic systems," *Chemometrics and Intelligent Laboratory Systems*, vol. 90, no. 2, pp. 153–160, 2009.

[31] D. Ferrari, M. Borrotti, and D. de March, "Response improvement in complex experiments by co-information compostite likelihood optimization," *Statistics and Computing*, 2013.

[32] F. Hutter, H. H. Hoos, K. Leyton-Brown, and T. Stützle, "ParamILS: an automatic algorithm configuration framework," *Journal of Artificial Intelligence Research*, vol. 36, pp. 267–306, 2009.

[33] I. Lohse, S. Lang, J. Hrbacek et al., "Effect of high dose per pulse flattening filter-free beams on cancer cell survival," *Radiotherapy and Oncology*, vol. 101, no. 1, pp. 226–232, 2011.

[34] C. C. Ling, I. J. Spiro, J. Mitchell, and R. Stickler, "The variation of OER with dose rate," *International Journal of Radiation Oncology, Biology, Physics*, vol. 11, pp. 1367–1373, 1985.

[35] H. B. Michaels, E. R. Epp, C. C. Ling, and E. C. Peterson, "Oxygen sensitization of CHO cells at ultrahigh dose rates: prelude to oxygen diffusion studies," *Radiation Research*, vol. 76, no. 3, pp. 510–521, 1978.

[36] Y. Shibamoto, S. Otsuka, H. Iwata, C. Sugie, H. Ogino, and N. Tomita, "Radiobiological evaluation of the radiation dose as used in high-precision radiotherapy: effect of prolonged deliverytime and applicability of the linear-quadratic model," *Journal of Radiation Research*, vol. 53, no. 1, pp. 1–9, 2012.

[37] S. A. Sapareto and W. C. Dewey, "Thermal dose determination in cancer therapy," *International Journal of Radiation Oncology Biology Physics*, vol. 10, no. 6, pp. 787–800, 1984.

Hindawi Publishing Corporation
Computational and Mathematical Methods in Medicine
Volume 2013, Article ID 782049, 7 pages
http://dx.doi.org/10.1155/2013/782049

Research Article

A Study of Rough Set Approach in Gastroenterology

Ahmet Sahiner and Tuba Yigit

Department of Mathematics, Suleyman Demirel University, 32260 Isparta, Turkey

Correspondence should be addressed to Ahmet Sahiner; ahmetnur32@gmail.com

Received 27 August 2013; Accepted 11 October 2013

Academic Editor: Rudolf Füchslin

We try to determine the type of abdominal pain of the patients who have several symptoms. Via the rough set theory, we obtain information table and discernibility matrix and put forward the status decision information. Thus, we obtain certain results and test these operations by the Rosetta program.

1. Introduction

Rough set theory was introduced by Pawlak in the early 1980s [1, 2]. The basic idea of this theory depends on classifying the objects that cannot be discernible according to some qualities. Rough sets can be defined using doubt, vagueness, and indeterminacy [3]. The theory can be used as a tool to discover data dependencies and to reduce the number of attributes contained in a data set requiring no additional information [4].

The most important feature of rough sets is that the theory is supported by mutual model development by practical exercise tools. In rough set, a large number of software systems are present. Rosetta and RSES can be given as an example. If we think of the problem of making groups of members which have a large number of qualifications in the set, the increasing number of members and qualities of members makes us insufficient to solve the problem.

Abdominal pain is one of the most common complaints that everybody may have at least once or a few times and one of the most important complaints that causes patient to go to doctor. Acute abdominal pain or acute abdominal as is called in surgery includes pathologies occurring with pain in abdominal region depending on the reasons except trauma which may require medicine or medical surgery. The reasons constituting clinical table include a lot of pathologies from mild to serious. Delays in diagnosis and cure may affect the success remarkably. Although there are many new and comprehensive methods by means of technological innovations, detailed story, careful inspection and doctor's predecisions are still too important.

Gastrointestinal infection (infectious intestinal disease) can be caused by a variety of communicable diseases and infections, which gain entry by and/or affect the gastrointestinal tract.

Infectious intestinal disease affects as many as 1 in 5 members of the population each year.

In this study data of the patients (who have abdominal pain) had been collected by the doctors who are employed in a private hospital at internal diseases clinic. The data of 58 patients suffering from these diseases have been examined. As the result of that examination the number of symptoms has been limited by 10. It is provided that the symptoms are diagnosed quickly by using minimum symptoms in the analysis part. Thus a leading data analysis has been done for decision periods of doctors.

2. The Concept of Rough Set

A data set is represented as a table, where each row represents a case, an event, a patient, or simply an object. Every column represents an attribute (a variable, an observation, a property, etc.) that can be measured for each object; the attribute may be also supplied by a human expert or user. This table is called an information system. More formally, that is a pair $A = (U, A)$, where U is a nonempty finite set of objects called the universe and A is a nonempty finite set of attributes

such that $a : U \to V_a$. The set is called the value set of $a \cdot a(x)$ denotes the value of attribute a for object x. Any subset $B \subseteq A$ determines a binary relation IND(B) on U, called indiscernibility relation, if $a(x) = a(y)$, for every $a \in B$.

The family of all equivalence classes of IND(B), namely, the partition determined by B, will be denoted by U/B. An equivalence class of IND(B) containing x will be denoted by $B(x)$. If $(x, y) \in \text{IND}(B)$ we will say that x and y are B-indiscernible.

Given an object subset $X \subset U$, we call $\underline{B(x)}$ and $\overline{B(X)}$ the B-lower and B-upper approximation of X, respectively; $\underline{B(x)}$ and $\overline{B(X)}$ are defined as follows:

$$\underline{B(x)} = \{x \in U : B(x) \subseteq X\},$$
$$\overline{B(X)} = \{x \in U : B(x) \cap X \neq \emptyset\}. \quad (1)$$

$\text{BN}_B(X) = \overline{B(X)} - \underline{B(x)}$ is referred to as the B-boundary region of X. If $\text{BN}_B(\overline{X}) = \emptyset$, then the set X is exact with respect to B, or X is referred to as rough set with respect to B.

R is a family of equivalence relations, $r \in R$; if $\text{IND}(R) = \text{IND}(R - r)$, we say that r is indispensable in R.

Given $Q \subseteq R$, $\text{IND}(Q) = \text{IND}(R)$, and for any $q \in Q$, q is indispensable. We say that Q is a reduct of R. Obviously, there is not only a single reduct mostly. Core is defined as the common part of all reducts:

$$\text{Core} = \cap \text{red}(R), \quad (2)$$

where red(R) denotes all of the reducts of R. Reduct and core are two fundamental concepts of rough set theory. The reduct is the essential part of the information system, which can discern all objects discernible by the original one [5–13].

3. Data Set

3.1. List of Attributes of Symptoms. According to the information provided above, in order to be able to diagnose the related diseases distinctively we investigate answers to questions consisting of the following ten items. The letter a stands for attribute:

(a_1) severity of abdominal pain ((1) mild, (2) medium, or (3) severe);

(a_2) features of abdominal pain ((1) heavyset, (2) agonizing, or (3) reflecting pain);

(a_3) characteristics of abdominal pain ((1) steady or (2) changeable);

(a_4) duration of abdominal pain ((1) sudden start, (2) for days, (3) for months, or (4) for years);

(a_5) location of abdominal pain ((1) right upper dial, (2) epigastric, (3) left upper dial, (4) umbilical, (5) right hypochondrium, or (6) left hypochondrium (7) pervasive);

(a_6) relation to eating, ((1) increasing, (2) decreasing, or (3) steady);

(a_7) the existence of alarm symptoms (anemia, losing weight, and rectal bleeding) ((1) alarm symptom exists, (2) alarm symptom does not exist);

(a_8) the existence of systemic symptoms (fever, strong heartbeat, and low tension) ((1) systemic symptom exists (2) systemic symptom does not exist);

(a_9) stomach intestine discomfiture ((1) bloated feeling-constipation, (2) bloated feeling-diarrhea, (3) bloated feeling-constipation-diarrhea or (4) no discomfiture);

(a_{10}) the existence of dyspeptic complaints ((1) nausea-vomit, (2) burning-souring, (3) bitter liquid taste in mouth, or (4) pyrosis).

4. Clinical Table

The most significant symptom in the acute abdomen chart is the abdominal pain. Since the patient arrives at the clinic with a complaint of abdominal pain, the beginning of the history should also be with abdominal pain. The localization of pain and its beginning and development characteristics should be considered.

Different characters of abdominal pain in a patient with acute abdomen carry significant signs/traces/footprints in the diagnosis of the illness. It is possible to list those characters under the headings as follows:

(1) reflection feature,

(2) severity/intensity,

(3) beginning and development feature,

(4) form and period (frequency),

(5) relation with food.

To give a brief summary of the illnesses examined in this context, we state the following.

Cholecystitis (Inflammation of Gallbladder). It is an illness caused by the inflammation of the gallbladder. It usually develops depending on the stone in the gallbladder. It comes, suddenly or within hours, as agonizing pain localized in the upper right quadrant along with systemic symptoms such as fever, nausea, and vomiting.

Peptic Ulcer. It is an illness characterized by the increase of acid-pepsin secretion in the stomach. It is an inflammatory illness of the stomach. It is an illness whose most significant symptoms are heavyset burning-scraping pains whose reflections can sometimes be felt on shoulders and back. Stress and oily-spicy foods may trigger this illness.

Irritable Intestinal Syndrome (Delicate Intestinal Illness). It is an illness especially of the large intestine. There has been an increase in the frequency of the illness recently. There is an increase in the sensitivity of the nerve cells in the large intestine mucosa. It does not have a sudden start. It is

characterized by a pain in the abdominal region, swollenness, constipation, and/or diarrhea attacks.

Pancreatic Inflammation. It is an inflammatory illness of pancreas. It occurs suddenly; generally it may cause pervasive abdominal pain. One of the most common causes is long-term excessive alcohol consumption. Other causes include

(i) high levels of calcium in the blood;

(ii) abnormalities in anatomy which are usually present at birth;

(iii) cystic fibrosis;

(iv) high blood fats (hypertriglyceridemia);

(v) in rare cases, some drugs can cause pancreatitis;

(vi) in a number of cases no specific cause can be identified, a condition known as idiopathic pancreatitis.

Reflux. When you have something to eat or drink, it passes down the oesophagus (gullet) into the stomach. The flow of traffic should definitely be one way. However, reflux occurs when whatever happens to be in your stomach travels in the wrong direction back up into the oesophagus. Unlike vomiting, which is quite a violent activity, reflux mostly occurs without us being aware that it is happening.

Poor diet is believed to be the most prevalent acid reflux cause. Acid reflux occurs during digestion, when the stomach churns up acid or refluxes into the esophagus, causing a burning sensation in the chest or throat. Too much acid can push back through a valve between the stomach and the esophagus called the lower esophageal sphincter (LES). Along the same lines as diet, overeating also causes reflux. When you overeat, the stomach cannot keep up with the demand to process all the acids. So food gets backed up, and digestive acids infiltrate the esophageal valve to cause that unpleasant burning feeling centered in the chest.

Other factors that create a predisposition for acid reflux include smoking, use of alcohol, food allergies, certain medications, and lying down after meals.

The most frequent symptom is heartburn which is a burning sensation in the chest. Run heartburn is often most noticed at the lowest end of the bone, and the discomfort rises upwards to an extent that varies from individual to individual. Sometimes the burning feeling can reach all the way up to the throat. Heartburn occasionally can be felt deeply within the chest—almost within the back. Some patients notice reflux when some of the contents of their stomach "repeat" by coming back up the esophagus as far as the throat or even the mouth.

Enteric. It is an inflammation of intestine mucus and generally caused by bacteria and infections. It comes into existence sometimes abruptly and sometimes within hours as agonizing pains. Enteric symptoms included nausea, vomiting, abdominal pain, flatulence, tenesmus, fecal urgency, and incontinence.

It is an inflammation of intestine mucus and generally caused by bacteria and infections. It comes into existence sometimes abruptly, sometimes within hours as agonizing pains. Enteric symptoms included nausea, vomiting, abdominal pain, flatulence, tenesmus, fecal urgency, and incontinence.

5. Reduction and Status Decision

5.1. Collection of Data Bases. In this section, data of patients with abdominal pain provided through a questionnaire and converted into symptoms table attribute list"; hence we are ready to reduct the collected data by the technique of Rough Set theory. The list of attribute of symptoms consists of 10 basic attributes. In fact we have an information table including 58 different patients' symptoms. But for the sake of simplicity Table 1 is constructed according to only 29 different patients' symptoms.

The patients are shown as "Y", and they are numerated as $Y_1, Y_2, \ldots, Y_{58}$ in order. The attributes are shown as letter "a" and are numerated as $a_1, a_2, \ldots, a_{10}$ in order. This 58×10 matrix is constructed according to attribute list obtained by complaint questionnaire. The numbers in the cells denote the value according to (3) as follows. Example of discernibility matrix for (Y_1, Y_2, Y_{58}) is

$$\begin{pmatrix} & Y_1 & Y_7 & Y_{58} \\ Y_1 & & & \\ Y_7 & a_5, a_6 & & \\ Y_{58} & \begin{matrix} a_1, a_2, a_4, \\ a_5, a_8, a_9, \\ a_{10} \end{matrix} & \begin{matrix} a_1, a_2, a_4, \\ a_6, a_8, a_9, \\ a_{10} \end{matrix} & \end{pmatrix}, \tag{3}$$

the table which was found as the result of making the data numerical. A column H showing the diagnosis of the patients will be added after that. The data set

$$H_i = \begin{Bmatrix} \text{IBS}, i = 1 \\ \text{PU}, i = 2 \\ \text{Enteritis}, i = 3 \\ \text{Reflux}, \ i = 4 \\ \text{Cholecystitiss}, i = 5 \\ \text{Pancreatitis}, i = 6 \end{Bmatrix} \tag{4}$$

is arranged by column H in Table 1. The illnesses are numerated from 1 to 6 and are arranged in Table 1.

5.2. Discernibility Matrix and the Reductions. By the data taken from Table 1 our system becomes 58×58 symmetric discernibility matrix. The component c_{ij} for $i \neq j$ of this matrix corresponds to symptoms attribute set. In this way, we have the opportunity to compare symptoms attributes of a given group of patients to those others, and then we can record these differences into the corresponding cell to obtain the discernibility matrix. The examples of rows and columns of this matrix for the cell Y_1, Y_7, and Y_{58} are as in (3).

Our real discernibility matrix will be filled by caring the symptoms differences among the patients in the disease groups in this way. This matrix is a diagonal symmetric. Using the discernibility matrix, the discernibility function can be found. The function f_A is constructed as follows. Those are

Table 1: The symptoms for 29 of 58 different patients.

	a_1	a_2	a_3	a_4	a_5	a_6	a_7	a_8	a_9	a_{10}	H
Y_1	1	1	1	4	6	1	2	2	1	2	**1**
Y_2	1	1	1	4	7	3	2	2	1	4	**1**
Y_3	2	1	2	3	4	1	1	2	1	4	**1**
Y_4	1	1	1	4	6	3	2	2	3	2	**1**
Y_5	1	1	2	4	6	1	2	2	1	4	**1**
Y_6	1	1	2	4	4	1	2	2	3	4	**1**
Y_7	1	1	1	4	3	3	2	2	1	2	**1**
Y_8	1	1	1	3	3	1	2	2	3	4	**1**
Y_9	2	2	1	4	4	1	2	2	1	4	**1**
Y_{10}	1	1	2	3	6	3	2	2	3	4	**1**
Y_{11}	1	1	2	4	7	1	2	2	1	4	**1**
Y_{12}	1	1	1	4	4	1	2	2	3	2	**1**
Y_{13}	1	2	1	3	6	1	2	2	1	1	**1**
Y_{14}	1	1	1	4	7	1	2	2	1	4	**1**
Y_{15}	1	2	1	4	5	3	2	2	1	2	**1**
Y_{16}	1	1	1	3	2	1	2	2	3	4	**1**
Y_{17}	2	2	1	4	7	1	2	2	1	4	**1**
Y_{18}	2	1	1	4	6	3	2	2	3	4	**1**
Y_{19}	2	1	1	3	2	2	2	2	4	2	**2**
Y_{20}	2	2	1	2	2	2	2	2	4	3	**2**
Y_{21}	2	3	1	2	2	3	2	2	4	2	**2**
Y_{22}	2	3	1	3	2	2	1	2	4	2	**2**
Y_{23}	2	3	1	3	2	2	2	2	4	2	**2**
Y_{24}	1	3	1	3	2	2	2	2	4	2	**2**
Y_{25}	2	3	1	2	4	3	2	2	4	2	**2**
Y_{26}	2	1	1	3	2	2	2	2	1	2	**2**
Y_{27}	2	3	1	3	3	2	1	2	4	2	**2**
Y_{28}	1	3	1	3	7	2	2	2	4	2	**2**
Y_{29}	2	1	1	3	2	2	2	2	4	2	**2**

attributes within the same cell related by $(\vee)$ and those which are recorded in different cell are related by $(\wedge)$ operation. Thus, our discernibility function is

$$f_A(a_1, a_2, a_3, \ldots, a_{58}) = (a_5 \vee a_6, \vee a_{10}) \wedge (a_1 \vee a_3 \vee a_4 \vee a_5 \vee a_7 \vee a_{10}) \wedge (a_1 \vee a_5). \quad (5)$$

f_A discernibility function is simplified using the following features of the Boolean algebra:

$$a \vee (a \wedge b) = a$$
$$a \wedge (b \wedge c) = a$$
$$a \vee (b \wedge c) = (a \vee b) \wedge (a \vee c)$$
$$a \wedge (b \vee c) = (a \wedge b) \vee (a \wedge c). \quad (6)$$

When we have large data set, ROSETTA program can be used for analyzing the data tables. This program is used for data mining and knowledge processing. From given data bases, reduction process using several different algorithms reduces the mathematical overprocess. Language simplification process can be done in a short period by using "C++." In this part reductions with different methods and status-decision knowledge were found and shown with the examples of output data.

Table 2: Reduction result by using Johnson Algorithm.

	Reduct	Support	Length
1	$\{a_1, a_4, a_5, a_6\}$	100	5

Table 3: Reduction result by using Genetic Algorithm.

	Reduct	Support	Length
1	$\{a_1, a_2, a_3, a_7, a_{10}\}$	100	5
2	$\{a_2, a_3, a_4, a_5, a_6\}$	100	5
3	$\{a_2, a_3, a_5, a_9, a_{10}\}$	100	5
4	$\{a_1, a_3, a_6, a_9, a_{10}\}$	100	5
5	$\{a_1, a_3, a_4, a_9, a_{10}\}$	100	5
6	$\{a_1, a_3, a_5, a_6, a_{10}\}$	100	5
7	$\{a_1, a_2, a_3, a_5, a_6\}$	100	5
8	$\{a_2, a_3, a_5, a_6, a_{10}\}$	100	5
9	$\{a_1, a_3, a_6, a_7, a_{10}\}$	100	5
10	$\{a_1, a_3, a_4, a_5, a_6\}$	100	5
11	$\{a_2, a_3, a_6, a_7, a_8, a_{10}\}$	100	6
12	$\{a_2, a_3, a_4, a_6, a_9, a_{10}\}$	100	6
13	$\{a_2, a_3, a_4, a_7, a_8, a_{10}\}$	100	6
14	$\{a_2, a_3, a_4, a_7, a_9, a_{10}\}$	100	6
15	$\{a_2, a_3, a_6, a_7, a_9, a_{10}\}$	100	6
16	$\{a_2, a_3, a_4, a_5, a_7, a_{10}\}$	100	6

5.3. Constitution of Reductions with Different Algorithms. In the following we give the resulting reductions obtained by using different algorithms. The data provided below are obtained using access data base linked by Rosetta program. By using this method only one attribution pair with 5 tuples. The other attributes are listed in 3 and 4 tuples has been found. See Tables 2, 3, 4, and 5. More precisely, for the sake of summarizing we can say the following.

Using Johnson method gives us the minimal reduction. It has been supported 100% by $\{a_1, a_3, a_4, a_5, a_6\}$ as can be seen in Table 7.

If we use RSES which is a directory library having been consisted of its own library of ROSETTA program and known to be consisted in using the experimental methods, we find the results in Table 4.

Table 4 looks like the table which is found by the method of genetic algorithm. The difference between genetic algorithm and RSES exhaustive is that latter one is limiting with 6 tuples term. In RSES genetic algorithm a_3 attribute appears as discernibility attribute of 6 different abdominal pain diseases. At this point, if we remove a_3 and a_6 dominant

Table 4: Reduction result by using RSES Exhaustive Algorithm.

	Reduct	Support	Length
1	$\{a_1, a_2, a_3, a_5, a_6\}$	1	5
2	$\{a_1, a_3, a_4, a_5, a_6\}$	1	5
3	$\{a_1, a_3, a_5, a_6, a_{10}\}$	1	5
4	$\{a_1, a_2, a_3, a_7, a_{10}\}$	1	5
5	$\{a_1, a_3, a_4, a_9, a_{10}\}$	1	5
6	$\{a_1, a_3, a_6, a_7, a_{10}\}$	1	5
7	$\{a_1, a_3, a_6, a_9, a_{10}\}$	1	5
8	$\{a_2, a_3, a_4, a_5, a_6\}$	1	5
9	$\{a_2, a_3, a_4, a_7, a_{10}\}$	1	5
10	$\{a_2, a_3, a_4, a_6, a_9, a_{10}\}$	1	6
11	$\{a_2, a_3, a_5, a_6, a_{10}\}$	1	5
12	$\{a_2, a_3, a_5, a_7, a_{10}\}$	1	5
13	$\{a_2, a_3, a_5, a_9, a_{10}\}$	1	5
14	$\{a_2, a_3, a_6, a_7, a_8, a_{10}\}$	1	6
15	$\{a_2, a_3, a_6, a_7, a_9, a_{10}\}$	1	6

Table 5: Reduction result by using RSES genetic algorithm.

	Reduct	Support	Length
1	$\{a_2, a_3, a_4, a_7, a_{10}\}$	1	5
2	$\{a_1, a_3, a_6, a_7, a_{10}\}$	1	5
3	$\{a_2, a_3, a_4, a_5, a_6\}$	1	5
4	$\{a_1, a_3, a_4, a_5, a_6\}$	1	5
5	$\{a_1, a_2, a_3, a_7, a_{10}\}$	1	5
6	$\{a_1, a_2, a_3, a_5, a_6\}$	1	5
7	$\{a_1, a_3, a_6, a_9, a_{10}\}$	1	5
8	$\{a_2, a_3, a_5, a_6, a_{10}\}$	1	5
9	$\{a_2, a_3, a_5, a_7, a_{10}\}$	1	5
10	$\{a_1, a_3, a_4, a_9, a_{10}\}$	1	5
11	$\{a_1, a_3, a_5, a_6, a_{10}\}$	1	5
12	$\{a_2, a_3, a_5, a_9, a_{10}\}$	1	5
13	$\{a_2, a_3, a_6, a_7, a_8, a_{10}\}$	1	6
14	$\{a_2, a_3, a_4, a_6, a_9, a_{10}\}$	1	6
15	$\{a_2, a_3, a_6, a_7, a_9, a_{10}\}$	1	6

Table 6: Reduction result by using genetic algorithm.

	Reduct	Support	Length
1	$\{a_2, a_4, a_7, a_8\}$	100	4
2	$\{a_2, a_4, a_5, a_8\}$	100	4
3	$\{a_1, a_3, a_4, a_7, a_8\}$	100	5

Table 7: Reduction result by using Johnson algorithm.

	Reduct	Support	Length
1	$\{a_2, a_4, a_5, a_8\}$	100	4

attributes and rearrange the remaining eight attributes we obtain the following order:

$$\begin{aligned} &a_4 \longrightarrow a_3, \quad a_5 \longrightarrow a_4, \quad a_7 \longrightarrow a_5, \\ &a_8 \longrightarrow a_6, \quad a_9 \longrightarrow a_7, \quad a_{10} \longrightarrow a_8. \end{aligned} \tag{7}$$

Table 8: Reduction result by using RSES exhaustive.

	a_2	a_4	a_7	a_8	H
Y_1	∗	6	1	2	**1**
Y_2	∗	7	1	∗	**1**
Y_3	1	4	1	∗	**1**
Y_4	∗	6	3	2	**1**
Y_5	∗	6	1	4	**1**
Y_6	∗	4	3	4	**1**
Y_7	1	3	1	2	**1**
Y_8	∗	3	3	4	**1**
Y_9	2	4	1	4	**1**
Y_{10}	1	∗	3	4	**1**
Y_{11}	1	7	1	∗	**1**
Y_{12}	1	4	3	2	**1**
Y_{13}	2	6	1	1	**1**
Y_{14}	∗	7	1	∗	**1**
Y_{15}	2	5	1	2	**1**
Y_{16}	∗	7	3	∗	**1**
Y_{17}	2	7	1	4	**1**
Y_{18}	∗	6	3	4	**1**
Y_{19}	1	∗	4	2	**2**
Y_{20}	2	2	∗	3	**2**
Y_{21}	3	2	∗	∗	**2**
Y_{22}	3	2	∗	∗	**2**
Y_{23}	3	2	∗	∗	**2**
Y_{24}	3	2	∗	∗	**2**
Y_{25}	3	2	4	2	**2**
Y_{26}	∗	2	1	2	**2**
Y_{27}	3	2	4	2	**2**
Y_{28}	3	2	4	2	**2**
Y_{29}	1	∗	4	2	**2**
Y_{30}	3	4	4	2	**2**
Y_{31}	3	1	∗	2	**2**
Y_{32}	2	∗	2	∗	**3**
Y_{33}	1	7	2	1	**3**
Y_{34}	3	∗	2	1	**3**
Y_{35}	1	5	2	1	**3**
Y_{36}	3	∗	2	1	**3**
Y_{37}	2	∗	2	∗	**3**
Y_{38}	2	4	4	1	**3**
Y_{39}	1	∗	4	3	**4**
Y_{40}	1	∗	4	3	**4**
Y_{41}	1	∗	4	3	**4**
Y_{42}	∗	∗	1	3	**4**
Y_{43}	∗	∗	1	3	**4**
Y_{44}	∗	∗	1	3	**4**
Y_{45}	1	∗	4	3	**4**
Y_{46}	1	∗	4	3	**4**
Y_{47}	∗	∗	1	3	**4**
Y_{48}	∗	∗	1	3	**4**

Table 8: Continued.

	a_2	a_4	a_7	a_8	H
Y_{49}	*	1	4	4	**5**
Y_{50}	*	1	*	1	**5**
Y_{51}	*	1	*	1	**5**
Y_{52}	*	1	*	1	**5**
Y_{53}	*	1	*	1	**5**
Y_{54}	*	1	*	1	**5**
Y_{55}	2	1	4	1	**5**
Y_{56}	2	3	*	1	**6**
Y_{57}	2	7	4	1	**6**
Y_{58}	1	7	*	1	**6**

Then if we further apply reductions using the Rosetta program we obtain the results in Tables 6 and 7.

Having used this method, 4 tuples only two quality pair were found.

Table 7 gives us the information about the reduction result with respect to Johnson algorithm.

The output result $\{a_2, a_4, a_5, a_8\}$ supports 100%. "Length" shows how many terms the reduction has.

Equation (8) is decision related discernibility matrix

$$\begin{pmatrix} & Y_1 & Y_7 & Y_{58} \\ Y_1 & & a_4 & a_2, a_4, a_8 \\ Y_7 & a_4 & & a_2, a_4, a_8 \\ Y_{58} & a_2, a_4, a_8 & a_2, a_4, a_8 & \end{pmatrix}. \tag{8}$$

6. Decision Relative Discernibility Matrices and Decision Relative Discernibility Functions

Essentially by using attributes $(a_2 \wedge a_4 \wedge a_5 \wedge a_8) \vee (a_2 \wedge a_4 \wedge a_7 \wedge a_8)$ with four terms, decision relative discernibility matrices and decision relative discernibility functions are found. Then two different matrices will occur for attributes with 4 tuples.

Functions will be constituted from these matrices and will be simplified. Decision relative discernibility matrix is diagonal symmetric such as in discernibility matrix. Each column of this matrix is written as multiplication of addition of attributes. By this way, decision relative discernibility functions are found by writing it as multiplication of addition of attributes for each patient. This function for $(a_2 \wedge a_4 \wedge a_7 \wedge a_8)$ is obtained from $(a_2 \wedge a_4 \wedge a_5 \wedge a_8)$ decision relative discernibility matrix shown in Table 8.

We used a Matlab program to get functions from this matrix. Then the following result has been found by doing individual simplifications:

$$\begin{aligned} f_1(A) &= (a_4 \vee a_8) \wedge (a_4 \vee a_8) \wedge \cdots \wedge (a_2 \vee a_4 \vee a_7 \vee a_8) \\ &= a_4 \wedge a_7 \wedge a_8 \\ f_2(A) &= a_4 \wedge a_7 \\ &\vdots \\ f_{58}(A) &= a_4 \wedge (a_2 \vee a_8). \end{aligned} \tag{9}$$

Decision relative discernibility function for $(a_2 \wedge a_4 \wedge a_5 \wedge a_8)$ is shown with $g_i(A)$, $i = 1, \ldots, 58$ as the following:

$$\begin{aligned} g_1(A) &= a_4 \wedge a_8 \\ &\vdots \\ g_{58}(A) &= a_2 \wedge a_5 \wedge a_8. \end{aligned} \tag{10}$$

6.1. The Decision Rules. A decision table is made through decision relative discernibility functions which are related to the decision described above. In the decision table, rows represent patients, columns represent groups of attributes with 4 terms.

The decision table can be accepted as a decision set. Now, we explain how this table is constructed in our study. For example, the condition and the decision for (a_2, a_4, a_7, a_8) can be found through the followings

$$\begin{aligned} a_{4_6} a_{7_1} a_{8_2} &\Longrightarrow H^1 \\ a_{4_7} a_{7_1} a_{8_2} &\Longrightarrow H^1 \\ a_{4_7} a_{7_1} &\Longrightarrow H^1 \\ a_{2_1} a_{4_4} a_{7_1} &\Longrightarrow H^1, \\ a_{2_1} a_{7_4} a_{8_2} &\Longrightarrow H^2 \\ a_{2_2} a_{4_2} a_{8_3} &\Longrightarrow H^2 \\ a_{2_3} a_{4_2} &\Longrightarrow H^2 \\ a_{2_3} a_{4_2} a_{7_4} a_{8_2} &\Longrightarrow H^2. \end{aligned} \tag{11}$$

Also the condition and the decision for (a_2, a_4, a_5, a_8) can be found through the followings

$$\begin{aligned} a_{4_6} a_{8_2} &\Longrightarrow H^1 \\ a_{2_1} a_{5_2} a_{8_4} &\Longrightarrow H^1 \\ a_{2_1} a_{4_4} a_{5_1} a_{8_4} &\Longrightarrow H^1 \\ a_{4_6} a_{8_2} &\Longrightarrow H^1, \\ a_{2_1} a_{4_2} a_{8_2} &\Longrightarrow H^2 \\ a_{2_2} a_{4_2} a_{8_3} &\Longrightarrow H^2 \\ a_{2_3} a_{4_2} a_{5_2} &\Longrightarrow H^2 \\ a_{4_2} a_{5_1} a_{8_2} &\Longrightarrow H^2. \end{aligned} \tag{12}$$

Finally, the above can be explained; for instance, if abdominal pain located left hypochondrium and meteorism and constipation, dyspepsia, the disease of the patient may be IBS; that is,

$$a_{4_6} a_{7_1} a_{8_2} \Longrightarrow H^1, \tag{13}$$

and if abdominal pain is colic and located epigastrium, dyspepsia, the disease of the patient may be peptic ulcer; that is,

$$a_{2_2} a_{4_2} a_{8_3} \Longrightarrow H^2. \quad (14)$$

7. Conclusion

We realized that rough set theory is very useful in classifying and analyzing a data set which consists of many attributes. This method could be used in many areas of science such as medicine, biology, and pharmacology. For instance, in pharmacology, reduction of adverse effects of a drug is very important.

Abdominal pain taken into consideration in this study is a symptom which we come across a lot in society. Although there are many, the most striking attributes of this pain related to this case has been determined by this method and this helps doctors diagnose with a great accuracy in a short time.

On the other hand, of course it is possible to support our theoretical in principle study with some clinical tests. In this case it would be possible to form multivariate matrix and we could analyze it by using cluster analysis, principal components analysis, and neuron net classification.

Planned future works are as follows.

(1) Certain modern global optimization techniques such as fuzzy logic and intuitionistic fuzzy relations can be applied to this kind of problems.

(2) The least and the most effective symptoms will be determined by using some classic and modern optimization tecniques together to prevent wastage on health care costs.

Conflict of Interests

The authors declare that there is no conflict of interests regarding the publication of this paper.

References

[1] W. Marek and Z. Pawlak, *Rough Sets and Information Systems*, ICS PAS Reports, 1981.

[2] Z. Pawlak, "Rough sets," *International Journal of Computer & Information Sciences*, vol. 11, no. 5, pp. 341–356, 1982.

[3] Z. Pawlak, *Rough Sets: Theoretical Aspects of Reasoning About Data*, Kluwer Academic Publishing, Dordrecht, The Netherlands, 1991.

[4] R. Jensen, Q. Shen, and A. Tuson, "Finding rough set reducts with SAT," *Lecture Notes in Computer Science*, vol. 3641, pp. 194–203, 2005.

[5] D. Yu, Q. Hu, and W. Bao, "Combining multiple neural networks for classification based on rough set reduction," in *IEEE International Conference on Neural Networks & Signal Processing*, pp. 543–548, Nonjing, China, December 2003.

[6] E. Kondrad, E. Orlawska, and Z. Pawlak, *An Approximate Concept Learning*, Bericht, Berlin, Berlin, 1981.

[7] R. S. Michalski, "Recognition as role-guided inductive interference," *IEEE Transactions on Pattern Analysis and Machine Intelligence*, vol. 2, no. 4, pp. 349–361, 1980.

[8] J. E. Orlwaska, *Logic of Vague Concepts, Application of Rough Sets*, ICS PAS, Reports, 1982.

[9] A. Starzyk, D. E. Nelson, and K. Strutz, "Reduct generation in information systems, in information systems," *Bulletin of the International Rough Set Society*, vol. 3, no. 1-2, pp. 19–22, 1999.

[10] K. Svozil, "Quantum field theory on fractal spacetime: a new regularisation method," *Journal of Physics A*, vol. 20, no. 12, article 033, pp. 3861–3875, 1987.

[11] S. Telçeken, *Kaba Kümeler Teorisi Yardımı ile Büyük Veri Topluluklarının Analizi, Yüksek Lisans Tezi*, Fen Bilimleri Enstitüsü Anadolu Üniversitesi, 2003.

[12] L. Zhang and S. Malik, "The quest for efficient boolean satisfability solvers," in *Proceedings of the 18th International Conference on Antomated Deduction*, pp. 295–318, 2002.

[13] Y. Zhao, Y. Yao, and F. Luo, "Data analysis based on discernibility and indiscernibility," *Information Sciences*, vol. 177, no. 22, pp. 4959–4976, 2007.